RICE UNIVERSITY

Time-Lapse Imaging of Fault Properties at Seismogenic Depth Using Repeating Earthquakes, Active Sources and Seismic Ambient Noise

by

Xin Cheng

A THESIS SUBMITTED
IN PARTIAL FULLFILLMENT OF THE
REQUIREMENTS FOR THE DEGREE

Doctor of Philosophy

APPROVED, THESIS COMMITTEE:

Fenglin Niu, Associate Professor
Earth Science

Colin A. Zelt, Professor
Earth Science

Cin-Ty A. Lee, Associate Professor
Earth Science

Thomas W. Hill, Professor
Physics and Astronomy

HOUSTON, TEXAS

NOVEMBER 2008

ABSTRACT

Time-Lapse Imaging of Fault Properties at Seismogenic Depth Using Repeating Earthquakes, Active Sources and Seismic Ambient Noise

by

Xin Cheng

The time-varying stress field of fault systems at seismogenic depths plays the most important role in controlling the sequencing and nucleation of seismic events. Using seismic observations from repeating earthquakes, controlled active sources and seismic ambient noise, five studies at four different fault systems across North America, Central Japan, North and mid-West China are presented to describe our efforts to measure such time dependent structural properties.

Repeating and similar earthquakes are hunted and analyzed to study the post-seismic fault relaxation at the aftershock zone of the 1984 M 6.8 western Nagano and the 1976 M 7.8 Tangshan earthquakes. The lack of observed repeating earthquakes at western Nagano is attributed to the absence of a well developed weak fault zone, suggesting that the fault damage zone has been almost completely healed. In contrast, the high percentage of similar and repeating events found at Tangshan suggest the existence of mature fault zones characterized by stable creep under steady tectonic loading.

At the Parkfield region of the San Andreas Fault, repeating earthquake clusters and chemical explosions are used to construct a scatterer migration image based on the observation of systematic temporal variations in the seismic waveforms across the occurrence time of the 2004 M 6 Parkfield earthquake. Coseismic fluid charge or discharge in fractures caused by the Parkfield earthquake is used to explain the observed seismic scattering properties change at depth. In the same region, a controlled source

cross-well experiment conducted at SAFOD pilot and main holes documents two large excursions in the travel time required for a shear wave to travel through the rock along a fixed pathway shortly before two rupture events, suggesting that they may be related to pre-rupture stress induced changes in crack properties.

At central China, a tomographic inversion based on the theory of seismic ambient noise and coda wave interferometry clearly reveals a coseismic velocity decrease region with the strike and length strikingly matching the fault zone of the 2008 M 7.9 Wenchuan earthquake at depth. We speculate the imaged decrease velocity region resulted from decreased crustal stress around the fault zone at upper crust.

ACKNOWLEDGEMENTS

I would like to thank my advisor, Fenglin Niu, for his close guidance and great support during the past 5 years. I have learned a lot from Fenglin, about his enthusiasm in science and optimism in life.

I would like to thank my academic committee member, Colin Zelt and Cin-Ty Lee, for their constructive comments and suggestions, and for being so helpful during many circumstances.

I would like to thank my friends and colleagues, Yang He, Fuchun Gao, Li Zhang, Zhengxue Li, for their friendship and encouragement. Special thanks go to my officemate, Elizabeth Vanacore, for helping me with my English and editing most of my papers.

I would like to thank my parents and sister, for their love and unconditional support since the very beginning.

My finally thanks go to my beloved wife, Hui Wang. She joined me for this adventure, thousands of miles away from home and old friends. Hui, thank you for being with me during this long journey.

TABLE OF CONTENTS

Chapter 1

Introduction

The time-varying stress state of fault systems at seismogenic depths is perhaps the single most important property controlling the sequencing and nucleation of seismic events. The importance of stress has been illustrated recently by the success of predicted stress changes, based on Coulomb stress calculations, in accounting for the spatial distribution of aftershocks [*Stein*, 1999], as well as providing an explanation for the clustering of large seismic events, such as the nearby 1992 Landers and 1999 Hector Mine earthquakes [e.g., *Freed and Lin*, 2001]. Measuring and monitoring this stress field has thus been a long-sought goal for the solid-earth science community over the last few decades.

The measurement of stress, however, is notoriously difficult, particularly at seismogenic depths. Geodesy provides important constraints on the surface deformation field, which can be related to seismogenic stress through an assumed structural model of the rheology. Yet, the constraints on the depth distribution of stress and strain from geodesy are limited. These surface constraints need to be combined with other techniques that, while not as directly related to stress and strain, have superior depth resolution. The most promising techniques at present appear to be seismic. Numerous laboratory studies over several decades have shown that the elastic properties (seismic velocity, attenuation, anisotropy) of crustal rocks clearly exhibit stress dependence [e.g., *Birch*, 1960; 1961; *Scholz*, 1968; *Nur and Simmons*, 1969; *Crampin and Zatsepin*, 1997]. Such dependence is attributed to the opening/closing of microcracks due to changes in the stress normal to the crack surface [e.g., *Walsh*, 1965; *Nur*, 1971]. Thus stress changes can, in principle, be

detected by exploiting the stress sensitivity of the elastic properties of the seismogenic crust.

To measure such stress-induced variations at seismogenic depth, highly repeatable seismic sources, either natural such as repeating earthquake clusters or artificial such as repeated active explosions or shakers, are often used. There have been two major approaches to the problem. One approach is to observe temporal changes in the travel times of first arrivals. In this regime the scatterers are assumed to be small compared to a wavelength [e.g., *Crampin and Zatsepin*, 1997; *Yamamura et al.*, 2003]. As a result, these data constrain the background transmission velocity of the medium. The other approach is to examine temporal variations in the *P*- and *S*-wave coda (e.g., coda wave interferometry). This is effectively samples the cracks as seismic scatterers, in the regime where the wavelengths used are comparable to crack size. The coda is then the primary focus of the seismogram in that it represents a way to detect both changes in the properties of scatterers, as well as to obtain information on transmission velocity along paths taken by scattered energy through the medium. With this approach, convincing changes in coda properties attributed to both the coseismic damage of large earthquakes [e.g., *Baisch and Bokelmann*, 2001] and the aseismic stress transient [*Niu et al.*, 2003] are observed.

The main research goal of this thesis is to develop a reliable imaging method to monitor stress/strain transient at seismogenic depth and also to probe the rupture nature of earthquakes by utilizing seismic observation. In the following, I will give a brief overview of my entire thesis work, which can be divided in three parts.

The first part includes Chapter 2 and Appendix A. The focuses are aim at searching for repeating earthquakes at different tectonic environments and understanding their physical mechanism.

Since any variations presented in the observed seismic waveform inherit the changes in the source characteristics and medium properties, earlier studies of temporal variations in the seismic coda wave [e.g., *Chouet*, 1979; *Aki*, 1985, 1995], while suggestive, is criticized by possible errors due to a slightly changes in source parameters between earthquakes used. The recent observation of repeating earthquakes, however, can be used to greatly minimize the source uncertainties. Repeating earthquakes are a series of earthquakes regularly occurring on the same patch of a fault plane. These earthquakes usually occur with the same magnitude, source mechanism, and roughly the same repeating interval. When recorded at the same station, they produce nearly identical seismograms. They are commonly interpreted as repeated ruptures of a single asperity surrounded by a stably sliding area. It has been reported in the creeping zones of major faults along plate boundaries, such as several sections of the San Andreas Fault [*Ellsworth*, 1994; *Nadeau et al.*, 1995] and subduction zones in northeast Japan [*Igarashi et al.*, 2003].

In Chapter 2, we analyzed the waveform data of more than 21,000 microearthqaukes with a magnitude between 0 and 4.5 occurring between 1995 and 2001 in the aftershock zone of the 1984 western Nagano earthquake in central Japan. We found no evidence for repeating earthquakes at this intraplate fault. Together with other seismic investigation, such as no evidence for fault zone trapped wave associated with the main fault, we attribute the lack of repeating earthquakes to the absence of low-velocity damage zone

along the fault. Instead of repeating earthquakes, we observed a total of 807 similar aftershocks in the study period, which accounts for less than 4% of the total seismicity. The difference between repeating earthquakes and similar aftershocks is defined by their spatial distribution. In principle, the rupture areas of the repeating earthquakes overlap with each other, while similar aftershocks are displaced from one to another. These similar aftershocks occurred very closely in time, ranging from a few seconds to days. Taking the advantage of high quality array data, precise relocation showed that these events are separated by a few meters to about 100 m. There is a clear lower bound in distance between those consecutive events and the minimum appears to be proportional to the size of the first events. By assuming the minimum distance as the rupture radii, we observed a maximum stress drop of 10 MPa for these events.

In Appendix A, collaborating with our colleges, we analyzed the catalog, local and regional waveform data of more than 1000 earthquakes occurring between 2001 and 2006 in the aftershock zone of the 1976 Tangshan earthquake in North China. We identified a total of 46 similar or repeating event sequences composed by 328 earthquakes in this intraplate fault. The high percentage of similar and repeating events suggests a well developed weak zone featured by stable creep under steady tectonic loading. Analysis of the periods and magnitudes of the observed repeating events indicates an annual slip rate no larger than 2.6 ± 0.4 mm/yr at 15 km depth. The seismicity also clearly exhibits a dextral bend in the middle of the fault and more than 85% of the events occurred in the northern segment where relatively small coseismic slips were observed during the 1976 M 7.8 Tangshan earthquake. The two segments appear to have significant different *b* values, 1.03 ± 0.02 and 0.85 ± 0.03 for the northern and southern sections, respectively.

The relative lower seismicity and lower b value observed from the southern section reflects the collective effect of the fault geometry and the regional stress field resulting from the India-Eurasia collision.

The conclusion drawn from the above two studies combined with reports from other studies is that the existence of repeating earthquakes requires a well developed weak fault zone as well as a constant loading creep rate. The weak areas of the fault under stable creep due to tectonic loading, while the stress is build up on strong asperities, which are surrounded by a creeping area, until they reach to the critical point and release the stress through an earthquake, and then the processes restarts again. Thus, the usage of repeating earthquakes to study fault evolution is limited by the region of their existence and also their temporal coverage, which is usually determined by tectonic loading rate and rock properties. For example, for repeating earthquakes with $M \sim 1$ at San Andreas Fault, a constant surface creeping rate of 3 cm/yr creates a repeating rate about 1 year.

An effective way to expand studies based on repeating earthquakes is to use controlled sources such as repeated explosions or shakers. With the advantage of exactly known source timing and location, repeating shots are also capable of monitoring temporal changes of velocity field associated with large earthquakes. The extension of repeating earthquakes study to the usage of controlled artificial sources is presented as the second part of this thesis work.

The second part includes Chapter 3 and Appendix B. The focus is trying to develop a reliable time-lapse monitoring method by using active source data or loosely defined co-located event clusters. Thus, we can break the holdback of repeating earthquakes.

In Chapter 4, as an extension of study of *Niu et al.* [2003], on the basis of coda wave interferometry, we developed a new scatterer migration imaging method to distinguish waveform variations induced by source location, background velocity or localized velocity change. In this study, we use borehole records of four repeating earthquake clusters and two repeating explosions to investigate temporal and special varying seismic scattering properties at the Parkfield region of the San Andreas Fault associated with the 2004 M 6 Parkfield earthquake. A systematic temporal variation is observed in both seismograms of the repeating earthquakes and the explosions that occurred before and immediate after the 2004 Parkfield earthquake. Application of our migration technique to loosely co-locate (~10 m apart) controlled source data reveals a consistent 4-D scattering image with the one derived from repeating earthquake clusters. The migration images a well defined localized changing of seismic scattering properties, e.g., a "moving" scatterer, on the fault rupture zone and at 3 km depth beneath Middle Mountain area. The location of the moving scatterer is near the same region reported by *Niu et al.* [2003], which was coincident with a well documented 1993 aseismic transient. The scattering waveform variations are most clearly observed with P to S or S to S converted phases, which indicates a most likely cause of S velocity change. We speculate the observed scattering properties change is the result of fluid charge or discharge in fractures caused by the 2004 Parkfield earthquake. Our new technique of scatterer migration imaging developed through this study can be applied to broad regions where relatively loosely defined clusters are available.

In Appendix B, taking the advantage of a specially designed repeatable piezoelectric source, modern data acquisition systems and advanced computational capability, we have

conducted a controlled source cross-well experiment at SAFOD pilot and main holes at Parkfield, California, to directly explore stress sensitivity at seismogenic depth. Over a two-month period, we observed an excellent anticorrelation between changes in the time required for a shear wave to travel through the rock along a fixed pathway and variations in the barometric pressure. We also observed two large excursions in the travel time data that are coincident with two earthquakes that are among those predicted to produce the largest coseismic stress change at SAFOD. The two excursions start approximately 10 and 2 hours before the events, respectively, suggesting that they may be related to pre-rupture stress induced changes in crack properties, such as dilatancy observed in early laboratory studies [*Brace et al.*, 1966; *Scholz*, 1968]. The encouraging observation in this study might provide an effective tool for understanding the stress changes that accompany and perhaps precede seismic activity by continuous seismic monitoring.

The extension from repeating earthquakes to loosely co-located similar events, from natural sources to controlled artificial sources greatly expands our ability to do time-lapse measuring and monitoring in active tectonic region especially close to fault zones of large earthquakes or nearby active volcanoes. However, the largest disadvantages of active source experiments are the expensive cost and the poor depth sampling. Explosive energy usually cannot reach deep into the crust where we are most interested. This is where the third part of this thesis kicks in.

The third part of this thesis, which is Chapter 4, describes our efforts to incorporate recently developed seismic ambient noise and surface wave tomography technique with coda wave interferometry method to study the time-lapse properties of the velocity structure around the fault zone of the devastating 2008 M 7.9 Wenchuan earthquake.

It has been recently shown that the cross-correlation of the diffuse wave field (e.g., scattered coda wave of ambient noise) will yield the Green's function between two receivers, as if one of the receivers behaves like an impulsive source [*Weaver and Lobkis*, 2001]. The discovery of these buried waves in seismic ambient noise wave field provides a unique temporal coverage in structure properties monitoring as long as the availability of continuous wave field, since years long continuous seismic records can be used to recover repeated sampling waveform between station pairs as if one of the stations is a repeating source.

We analyzed 100 days (50 days before the earthquake and 50 days after) continuous records at 16 broadband stations close to the 2008 Wenchuan earthquake fault zone. Rayleigh wave signals between each station pair are extracted by cross-correlation of the daily records of seismic ambient noise wave field. A tomographic map at period of 10 to 25 s is inverted from the measured group velocities and agrees well with known regional crustal geology. A clear boundary is delineated between the high velocity Tibet plateau and the low velocity Sichuan basin. By measuring the differential travel time for the target period of the Rayleigh waves recovered from all the station pairs across the occurrence time of the Wenchuan earthquake, consistent travel time variations are observed in the study area. The tomographic inversion clearly shows an area with a ~0.4% velocity decrease coincident with the occurrence of the earthquake. The strike and length of this velocity decrease area strikingly matches the fault zone of the Wenchuan earthquake at depth. We speculate that the observed decrease of seismic velocity could be the result of decreased stress in the upper crust around the fault zone. Our results demonstrate the capability of using continuous seismic noise record to monitor the

temporal variations of stress field at seismogenic depth. The application of the method to other active tectonic region such as subduction zone of active volcano area will provide additional valuable information to study the physical mechanism in depth or even help disaster forecasting.

This thesis study seeks to make significant progress toward the goal of observing time dependent structural properties at seismogenic depths. We expect the methods developed and the observations made through our study would constitute a new and valuable observational capability for application to furthering our understanding of the triggering and sequencing of earthquakes. Another beneficial impact will also come from the possibility to forecast volcanic eruption by monitoring the deep process of magma supply.

Chapter 2 through Chapter 4, including Appendix A and B, is the collection of five papers written for submission and publication during the course of my thesis work.

- Chapter 2: Cheng, X., F. Niu, P. G. Silver, S. Horiuchi, K. Takai, Y. Iio, and H. Ito (2007), Similar microearthquakes observed in western Nagano, Japan, and implications for rupture mechanics, *J. Geophys. Res.*, *112*, B04306, doi:10.1029/2006JB004416.
- Chapter 3: Cheng, X., F. Niu , P. G. Silver, and R. Nadeau (2008), Seismic imaging of scatterer migration associated with the 2004 Parkfield earthquake using waveform data of repeating earthquakes and active sources, *Bull. Seismol. Soc. Am.*, to be submitted.
- Chapter 4: Cheng, X., F. Niu, and B. Wang (2008), Coseismic velocity change during the 2008 Wenchuan earthquake observed from seismic ambient noise, *Geophys. Res. Lett.*, to be submitted.

- Appendix A: Li, L., Q.-F. Chen, X. Cheng, and F. Niu (2007), Spatial clustering and repeating of seismic events observed along the 1976 Tangshan fault, north China, *Geophys. Res. Lett.*, *34*, L23309, doi:10.1029/2007GL031594.
- Appendix B: Niu, F., P. G. Silver, T. M. Daley, X. Cheng, and E. L. Majer (2008), Preseismic velocity changes observed from active source monitoring at the Parkfield SAFOD drill site, *Nature*, *454*, 204-208, doi:10.1038/nature07111.

Chapter 2

Similar microearthquakes observed in western Nagano, Japan and implications for rupture mechanics

2.1 Abstract

We have applied a waveform cross correlation technique to study the similarity and the repeatability of more than 21,000 microearthquakes (0<M<4.5) in the aftershock zone of the 1984 Western Nagano earthquake in central Japan. We find that the seismicity in this particular intraplate fault essentially consists of no repeating earthquakes that occurred on the same patch of the fault in a quasi-periodic manner in the study period between 1995 and 2001. On the other hand, we identify a total of 278 doublets and 62 multiplets (807 events) that occurred consecutively within seconds to days. Based on the relative arrival times of the *P* and *S* waves, we have obtained precise relative locations of these consecutive events with an error between several meters to a few tens of meters. There is a clear lower bound on the distances measured between these consecutive events and the lower bound appears to be proportional to the size of the first events. This feature is consistent with what *Rubin and Gillard* [2000] have observed near the San Juan Bautista section of the San Andreas Fault. Shear stress increases at the edge of an earthquake rupture and the rupture edge becomes the most likely place where the second events are initiated. The observed minimum distance thus reflects the rupture size of the first events. The minimum distance corresponds to the rupture size calculated from a circular fault model with a stress drop of 10 MPa. We found that using different time windows results in a slight difference in the delay time estimates and the subsequent projection locations, which may reflect the finite-size nature of earthquake ruptures.

2.2 Introduction

Repeating earthquakes are a series of earthquakes regularly occurring on a patch of a fault plane. These earthquakes usually have approximately the same magnitude with roughly the same repeating interval. They are commonly interpreted as repeated ruptures of a single asperity surrounded by a stably sliding area [e.g., *Nadeau et al.*, 1995]. Repeating earthquakes have been found in several sections of the San Andreas Fault [*Ellsworth*, 1994; *Nadeau et al.*, 1995] and in subduction zones, such as in northeast Japan [*Igarashi et al.*, 2003]. These regions are featured by either a large surface creep rate or a low seismic coupling coefficient. Also for the sections where repeating earthquake sequences are found in the San Andreas Fault, fault zone trapped wave studies [*Li et al.*, 1998; 2003] indicate the presence of a well developed low-velocity zone along the fault.

Because of the close location and similar source mechanism, repeating earthquakes usually produce nearly identical seismograms when recorded at the same station. Besides the repeating events, some adjacent immediate aftershocks are also observed to have very similar waveforms [*Rubin and Gillard,* 2000]. Here we discriminate the two types of similar events in terms of their spatial distribution. We define repeating events as earthquakes with approximately the same magnitude and their relative centroids distance being much smaller than the rupture radii, whereas the centroids of adjacent immediate aftershocks (following *Rubin and Gillard* [2000], hereafter referred as to consecutive events) are located outside of their rupture areas. Because of the high waveform similarity between repeating and consecutive earthquakes, they have been widely used to study rupture size and interaction of immediate adjacent aftershocks [*Rubin and Gillard,*

2000], as well as to detect temporal variations in seismic velocity near fault zones, either coseismic or aseismic [*Dodge and Beroza*, 1997; *Schaff and Beroza*, 2004; *Niu et al.*, 2003].

In this study we analyzed the waveform data of more than 21,000 microearthquakes with a magnitude between 0 and 4.5 occurring between 1995-2001 in the aftershock zone of the 1984 western Nagano earthquake in central Japan (Figure 2.1) to study the similarity and repeatability of these events. We chose the study area largely based on the availability of high quality array data and high seismicity in this region. With the data we first search for similar events. We further investigate the existence of repeating and consecutive events in this particular intraplate environment and examine whether rupture can reoccur immediately.

2.3 Data and Waveform Similarity Measurements

A magnitude 6.8 shallow earthquake (roughly right lateral strike slip) occurred in western Nagano in central Japan on September 14, 1984. The earthquake was followed by aftershocks that subsided after several years. However, several M=5+ earthquakes occurred during 1993-1995 in the same region, and since then, a high level of seismicity has been observed. A very dense seismic network with 56 stations including two borehole seismometers was set up to monitor the high level seismic activity in 1995. Each station is equipped with a three-component velocity transducer and a 16-bit analog-to-digital converter. The sensor has a natural frequency of 2 Hz and the system has a flat frequency response up to 4 KHz [*Iio et al.*, 1999]. Triggered data have been recorded at a very high sampling rate of 10 KHz. A total of 21,000 microearthquakes with magnitudes between 0

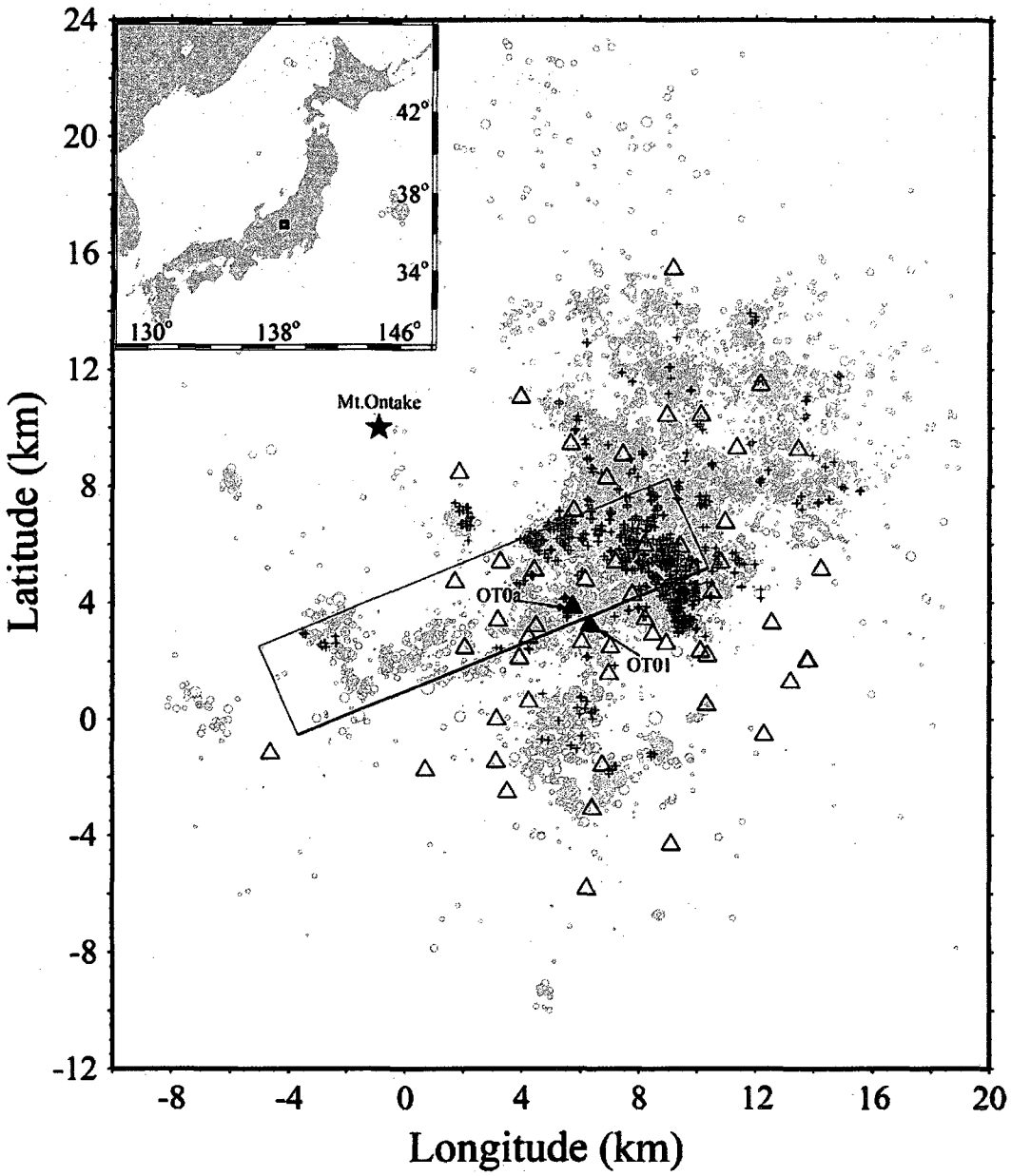

Figure 2.1 Geographic location of the aftershock area of 09/14/84 Nagano earthquake in central Japan. Earthquakes and stations are shown in dots and triangles, respectively. The rectangle is the fault plane of the main shock determined by *Yoshida and Koketsu* [1990]. The fault dips roughly to the north at an angle of 70° with the upper boundary (thick solid line) being 0.3 km below the surface. Crosses indicate the locations of the identified 807 similar events. The epicenter of the 1984 earthquake (35.79°N, 137.49°E) is taken as the origin of the coordinate. The fault plane is defined by four points: (35.7851°N, 137.4493°E, 0.3 km), (35.8365°N, 137.6050°E, 0.3 km), (35.8641°N, 137.5900°E, 9.9 km), (35.8127°N, 137.4343°E, 9.9 km). Two solid triangles indicate the two borehole stations OT0a and OT01.

and 4.5 were recorded between 1995 and 2001. Locations of those events were routinely determined from the *P*- and *S*-wave arrival times automatically picked using the method proposed by *Horiuchi et al.* [1992]. We manually checked the arrival times and then used them to relocate the earthquakes with the double-difference relocation algorithm hypoDD [*Waldhauser,* 2001]. The refined hypocenters are within a few hundred meters to the original locations and build the data set used in this study.

We calculated the cross-correlation of all the possible pairs of events recorded at one borehole station (OT01, Figure 2.1) using a time window that covers both *P* and *S* waves to find potential similar events. OT01 was chosen for its long coverage and high quality data. It has been operating since the network was installed in 1995 whereas the other borehole station, OT0a was installed in 1998. Two waveforms with a cross-correlation coefficient (cc) ≥ 0.8 were selected as preliminary candidates of similar events and were used for further analysis. We then expanded our cc measurements to all records for those potential similar events. We first converted the velocity seismograms to displacement records (see below for details) and then hand picked the *P*- and *S*-wave time windows. An example of the two picked time windows is shown in Figure 2.2. We then calculated the cc for both the *P* and *S* waves and counted numbers of stations with cc ≥ 0.8 for both *P* and *S* waves. If the number of stations with high cc values (≥ 0.8) is greater than 6 and accounts for more than 80% of the total records, we defined them as similar events (time delays measured from pairs with cc ≥ 0.9 are used for relocation). We found in general the cc is closely related to the signal-to-noise ratio (*SNR*) of the measured records; those with greater cc values usually have a larger *SNR*.

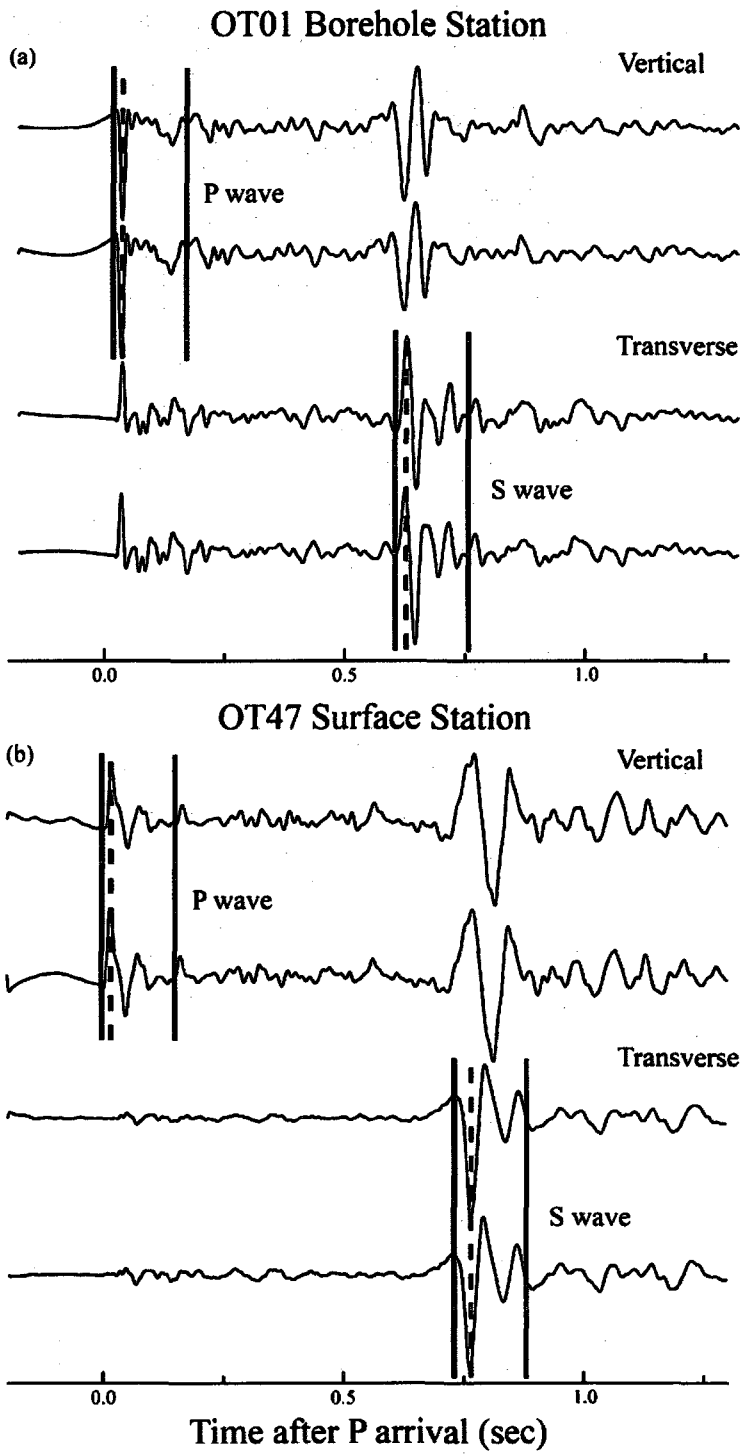

Figure 2.2 Examples of seismograms of two similar events recorded at the 150-m-deep borehole station OT01 (a) and a surface station, OT47 (b). The *P*- and *S*-wave time delays are measured from the vertical and transverse components, respectively. Vertical lines denote the two time windows used in this study.

2.4 Differential Time Measurements and Error Estimations

It is well known that it is possible to obtain sub-sample time precision through coherence measurements. In our study, we employed a cosine fitting method to estimate sub-sample delay time in time domain [*de Jong et al.*, 1990; *Cespedes et al.*, 1995]. Given the largest sample of the correlation function, *cc(0)*, and its two neighbors *cc(-1)* and *cc(1)*, the estimated sub-sample shift is given by following expression:

$$\tau = \alpha / \arctan\left(\frac{cc(-1)-cc(1)}{2cc(0)\sin\alpha}\right), \text{ where } \alpha = \arccos\left(\frac{cc(-1)+cc(1)}{2cc(0)}\right) \quad (1)$$

The measured differential times were further confirmed with direct interpolation of either the two time series or the cross correlation functions.

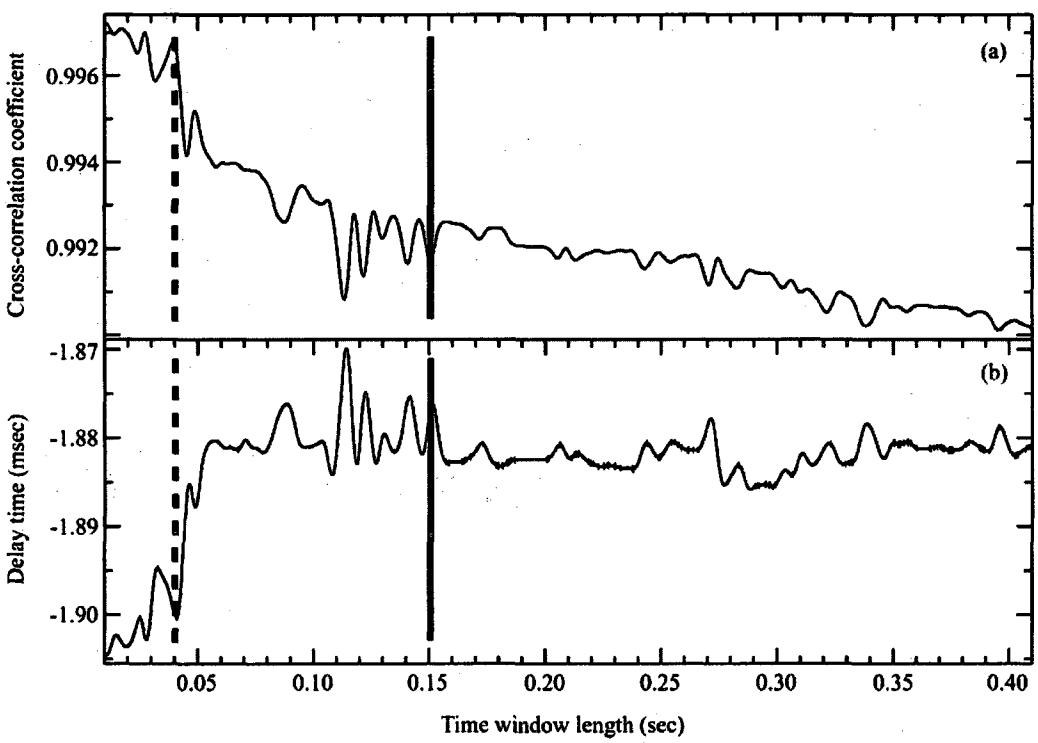

Figure 2.3 Cross-correlation coefficient (a) and delay time (b) measurements are shown as a function of time window length for *P* wave recorded at OT01 shown in Figure 2.2a. The two vertical lines defined the two time windows used in delay time measurements.

In general the measured differential time shows little dependence on the time window length except for the first half cycle which we will discuss in detail later (Figure 2.3). We chose to use a fixed time window, 0.15 s for both *P* and *S* waves, which covers at least two cycles of the *P* and *S* waves that have a dominant frequency higher than 15 Hz (Figure 2.2a).

When the cross correlation method is used to measure the differential time between two highly similar wavelets, there exists a theoretical lower bound which places a limit on the performance of all unbiased time delay estimators. This limit is known as the Cramer-Rao Lower Bound (CRLB) [e.g., *Carter*, 1987; *Walker and Trahey*, 1995]. It predicts that the low bound in time delay measurements is directly related to *SNR*:

$$\Delta t_{RMS} = \frac{1}{\sqrt{2} \cdot \omega_0 \cdot SNR}. \qquad (2)$$

Here ω_0 is the dominant angular frequency in the *P*- and *S*-wave time windows. Derivation of equation (2) is outlined in the Appendix. Equation (2) indicates that the *SNR* is the only parameter that controls the precision in our time delay estimation when the digitizing error is much less than the background noise. The precision is not controlled by the sampling rate of the digitizer and it is possible to obtain sub-sampling interval measurements of the time delay. The dominant frequency for our data is 30 Hz for the *P* wave and 15 Hz for the *S* wave, respectively. *SNR* is taken as lower value computed from the two seismograms for calculating cc. Most of the data have an *SNR* greater 10, which means that the estimated error is below 1 ms. Since the rupture sizes of the analyzed events are in the range of a few meters to a few hundreds of meters, we rounded up our delay time measurements to one tenth millisecond. Therefore errors in the delay time estimations are between 0.1 ms and 1 ms.

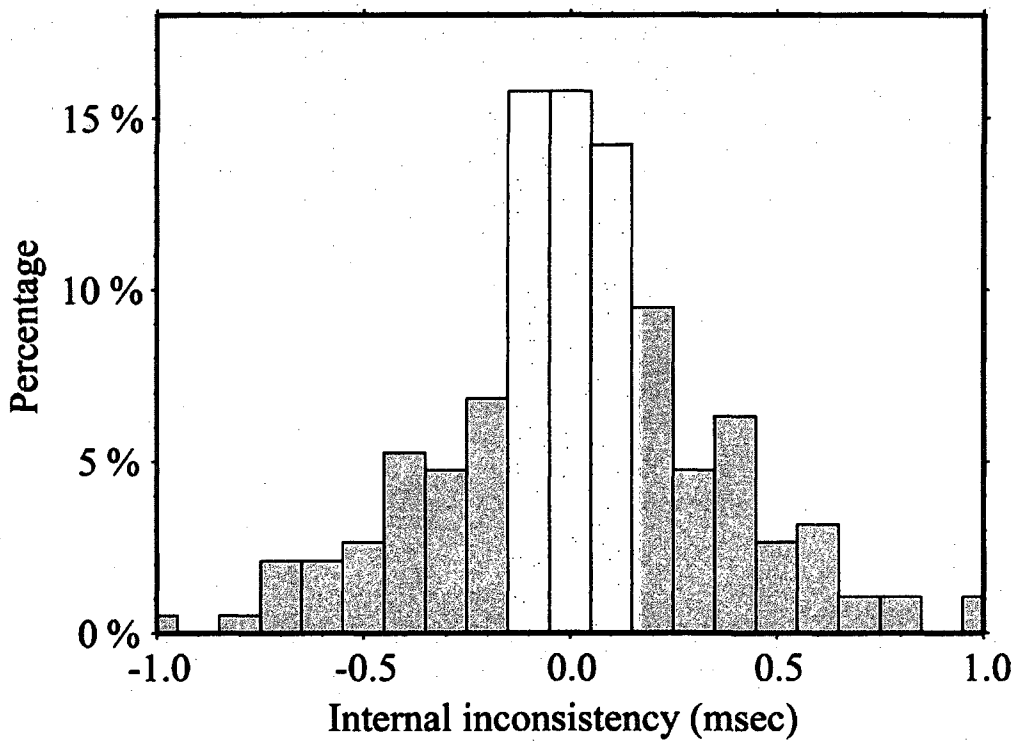

Figure 2.4 Histograms showing the distributions of internal inconsistency in the multiplet delay-time measurements. See the text for details on the internal inconsistency.

An alternative way to estimate error is to use internal inconsistency existing in the delay times between the pairs in a multiplet. For a multiplet with three events, for example, we can obtain three *S-P* differential times for three pairs, ΔT_{12}^{o}, ΔT_{13}^{o}, and ΔT_{23}^{o}. Among the three differential times, only two are independent. In other words, we can calculate ΔT_{23}^{c} from ΔT_{12}^{o} and ΔT_{13}^{o}. The inconsistency between the measured ΔT_{23}^{o} and derived ΔT_{23}^{c} can be considered as an index of the measurement error. We obtained a total of 201 inconsistency estimates varying in the range between approximately -1 ms to 1 ms with a average of 0.02 ms and standard deviation of 0.2 ms (Figure 2.4), which is roughly consistent with the CRLB estimations.

2.5 Earthquake Relocation and Distance between Similar Events

2.5.1 Doublet relocation

Following *Got et al.* [1994] and *Rubin and Gillard* [2000] we assumed that similar events are sufficiently close that all the differences in travel times may be ascribed solely to the different ray paths in the source region. To avoid the tradeoff between origin time and event depth, instead of using *P*- or *S*-wave travel times, we used relative *S-P* travel times to determine their relative locations. The relative *S-P* differential time, ΔT_{ij}^{k}, between events *i* and *j* at station *k* is expressed as:

$$\Delta T_{ij}^{k} = \left(\Delta \mathbf{r}_{ij} \cdot \mathbf{n}_{\beta}^{k}\right)/\beta - \left(\Delta \mathbf{r}_{ij} \cdot \mathbf{n}_{\alpha}^{k}\right)/\alpha , \qquad (3)$$

where $\Delta \mathbf{r}_{ij}$ is the relative position vector, $\mathbf{n}_{\alpha}^{k}$ and $\mathbf{n}_{\beta}^{k}$ are the unit vectors along the *P* and *S* rays to station *k*, respectively, α and β are the *P*- and *S*-wave velocity in the source region. A 3D velocity model derived from a *P*- and *S*-wave tomographic study [*Cheng et al.*, in preparation] was used in calculating the take off angles.

For each similar event pair we have a system of linear equations in the form

$$\mathbf{Gm} = \mathbf{d} , \qquad (4)$$

where **G** is a $N \times 3$ (N is the total number of ΔT_{ij}^{k} observations) matrix, **m** is a vector of length 3, $[\Delta x, \Delta y, \Delta z]^{T}$, containing the relative locations to be determined, **d** is the data vector of the observed *S-P* differential times. We further introduced a weight to each of the equations in (3) and used the normal inversion scheme:

$$\mathbf{m} = \left(\mathbf{G}^{T}\mathbf{W}_{N}\mathbf{G}\right)^{-1}\mathbf{G}^{T}\mathbf{W}_{N}\mathbf{d} . \qquad (5)$$

Here $\mathbf{W}_{N}$ is a diagonal matrix made by the weights introduced to equation (4). $\mathbf{W}_{N}$ is calculated from a bi-weight function to downweight large anomalous data and also data

with large errors. We used the same bi-weight function proposed by *Mosteller and Tukey* [1979]

$$W_k = \max^2\left(0, 1-\left(\frac{R_k}{\alpha R_{med}}\right)^2\right), \tag{6}$$

where $R_k=\Delta T_k-\Delta\tau_k$ is the time residual. $\Delta\tau_k$ is time delay computed for the kth station based on known relative relocations, and R_{med} is the median of the set of absolute values of R_k. This weight function rejects observations that give residuals whose absolute value is α times greater than the median. α is usually chosen between 4 and 6 and we have used 4 in this study.

Based on the CRLB error measurements we constructed the diagonal data covariance matrix, $\mathbf{C_d}$. With the bi-weight function and data covariance matrix, we can construct $\mathbf{W_N}$,

$$\mathbf{W_N} = \mathbf{W_k}\mathbf{C_d^{-1}}. \tag{7}$$

The initial solution was obtained by assigning unit weights for $\mathbf{W_k}$. The inversion process was then iterated and the weighting factor $\mathbf{W_k}$ and $\mathbf{W_N}$, were updated at each step. The process was terminated when either the root-mean-square (RMS) residual reached a constant value or the maximum number of iterations was reached. Usually it took only a few iterations to reach the final solution.

2.5.2 Multiplet relocation

In the case of a multiplet, we are basically solving the similar linear system with an increased number of observations and unknowns. **G** becomes a $N\times3(M-1)$ matrix where N is the total number of observations (ΔT_{ij}^k), M is the total number of events in the multiplet; **m** becomes a vector of length $3(M-1)$, $[\Delta x_2, \Delta y_2, \Delta z_2, \ldots, \Delta x_M, \Delta y_M, \Delta z_M]^{\mathrm{T}}$,

which are the relative locations to the first event. **d** is still the data vector of the observed *S-P* differential times.

2.5.3 Relocation error

To estimate relocation errors, we first calculated model covariance matrix based on the following equation:

$$\mathbf{C_m} = \left(\mathbf{G^T W_N G}\right)^{-1}. \tag{8}$$

We then took the square root of the diagonal elements of $\mathbf{C_m}$ as the errors in the relative locations. Relocation errors estimated from this method range from a few tenths of meters to about ten meters. Generally errors estimated from the covariance matrix are believed to be underestimated [*Got et al.*, 1994].

To obtain a better estimation on the location errors, we used a rather straight forward grid searching method. We defined a 3D region surrounding the event locations determined by the above inversions with a set of grid points. For each grid point we calculated the RMS residual time using the same weighting parameter described in equation (6). The relocation uncertainty thus can be directly estimated from the uncertainties in the *S-P* time measurements (Figure 2.5). The location error corresponding to a 0.1 ms uncertainty (estimated from CRLB) in delay time measurements is a few meters, several times larger than those estimated from the covariance matrix method.

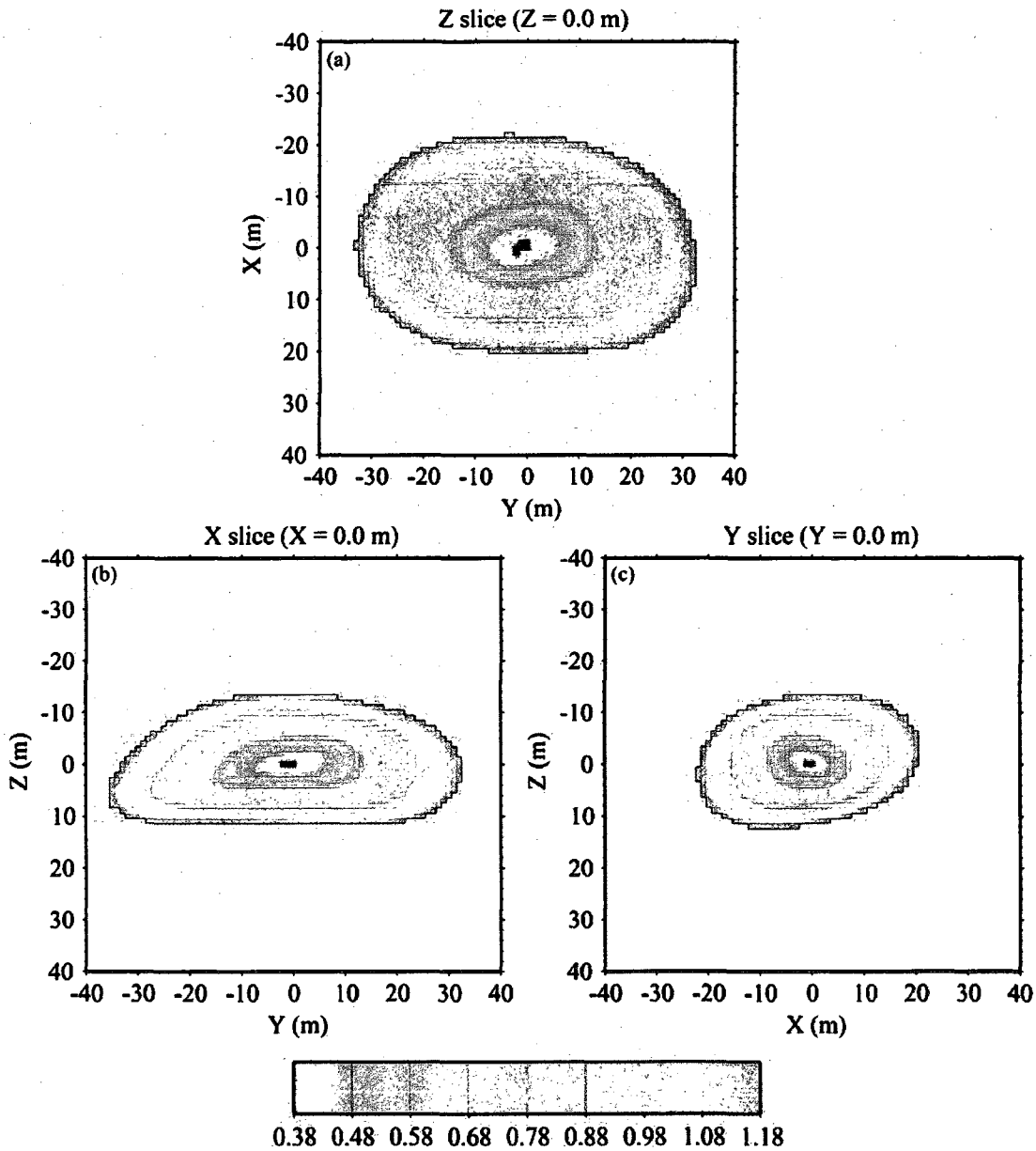

Figure 2.5 Three normal direction slices show 3D shape of the uncertainties with a grid-search method. Amplitude is the *S-P* residual in millisecond.

2.6 Estimation of Scalar Moment and Rupture Size

To compare the distances between the similar events with rupture sizes, it is necessary to have an objective measure of earthquake size. In this study we used the Brune Model [*Brune*, 1970] to estimate the scalar seismic moment M_o:

$$M_o = \frac{4\pi\rho c^3 R\Omega_o}{U_{\varphi\theta}}. \tag{9}$$

Here Ω_o is the displacement spectrum at zero frequency or the permanent displacement [*Abercrombie*, 1995]. ρ, c, R, and $U_{\varphi\theta}$ are density (2700 kg/m^3), seismic wave velocity (5.50 km/sec for P waves and 3.18 km/sec for S waves), hypocentral distance (in meters) and a correction term for radiation pattern, respectively. The spherical average of radiation patterns are 0.52 and 0.63 for P and S waves, respectively [*Aki and Richards*, 1980; *Abercrombie*, 1995].

The long period amplitude Ω_o was estimated by fitting displacement spectra. The ω^2 model of *Brune* [1970] and the revised model by *Boatwright* [1978] shown in equations (10) and (11), respectively, were used to fit the P- and S-wave amplitude spectra:

$$\Omega(\omega) = \frac{\Omega_o e^{-\frac{\omega t}{2Q}}}{1+\left(\frac{\omega}{\omega_c}\right)^2}, \tag{10}$$

$$\Omega(\omega) = \frac{\Omega_o e^{-\frac{\omega t}{2Q}}}{\left[1+\left(\frac{\omega}{\omega_c}\right)^4\right]^{0.5}}, \tag{11}$$

Here ω and ω_c are the angular frequency and corner frequency, respectively. Q and t are the quality factor and the arrival time of the P or S wave. The Boatwright model has a sharper corner than the Brune model. In equations (10) and (11), we have three free parameters, Ω_o, ω_c and Q, to fit. We found that Q is less well constrained compared to the

other two parameters. We thus used a constant Q model (Q_p= 300, Q_s= 560, *Stork and Ito* [2004]; *Imanishi et al.*, [2004]) and searched for the Ω_o and ω_c that best fit the observed *P*- and *S*-wave spectra.

To estimate the displacement spectra, we first converted velocity records to displacement by a deconvolution of the instrument response. The typical frequency response for a velocity transducer to ground velocity can be simplified as [*Aki and Richards*, 1980]:

$$I(\omega) = \frac{G\omega^2}{-\omega^2 + 2ih\omega_0\omega + \omega_0^2}, \tag{12}$$

where ω_0 is the natural frequency of the sensor ($2\pi \times 2$ Hz), h is the damping constant and G is the gain factor.

We used data recorded at the 800-m-deep borehole station (OT0a) to determine the scalar moment M_o. Figure 2.6 shows an example of the spectrum of the *P* wave from the vertical component. We used Levenberg-Marquardt algorithm [*Bates and Watts*, 1988] in finding the best fitting value of M_o. On average the Boatwright model fit better than the Brune model did, although the difference was trivial. We computed M_o from *P* and *S* waves, and the average value of the two was taken as the M_o estimate. Our estimates are consistent with those estimated by *Imanishi et al.* [2004], but are systematically higher than the values of *Stork and Ito* [2004]. The magnitude estimated by *Stork and Ito* [2004] was calculated from the dominant components (vertical for *P*, radial for *SV* and transverse for *SH*) only, we found significant energies in the minor components, for example, *P* in the radial and *SV* in the vertical components, which may explain the lower values of *Stork and Ito* [2004].

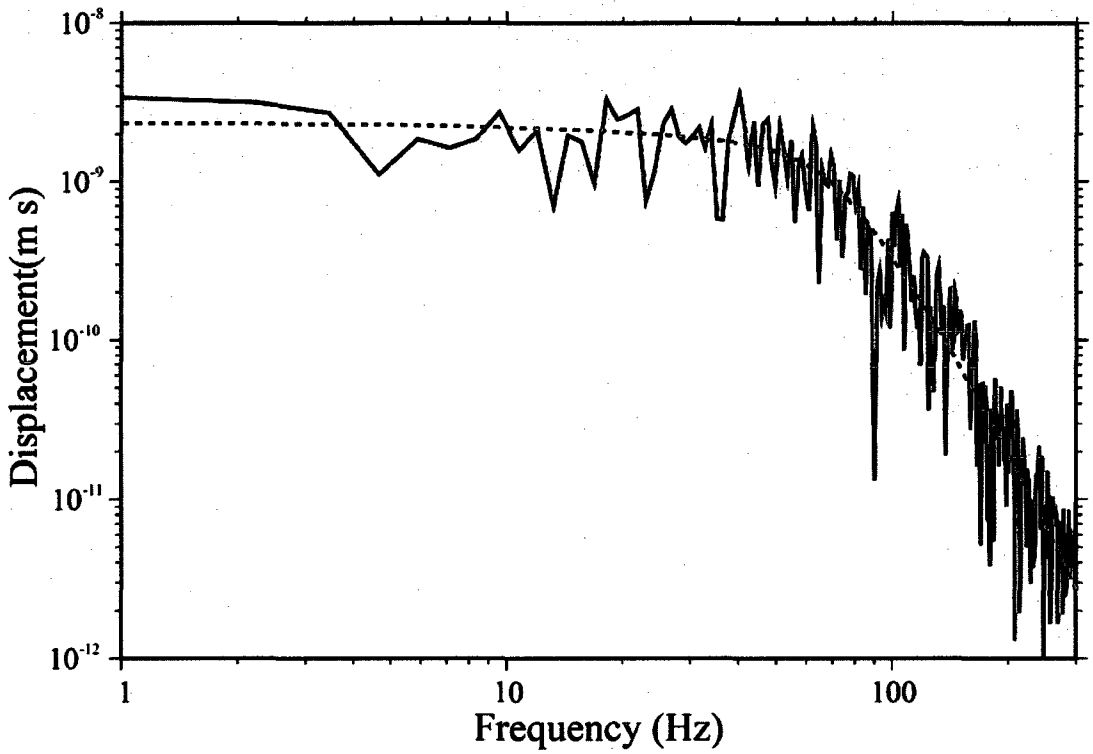

Figure 2.6 An example of the observed amplitude spectrum (solid line) at the 800-m-deep borehole station OT0a is shown with the best-fitting *Boatwright* [1970] ω^2 source model (dashed line).

The magnitude in the catalog was the JMA (Japan Meteorological Agency) magnitude (M_j). Since the 800-m-deep borehole seismometer was installed in 1998, we could not estimate M_o with this station for events that occurred before 1998. We therefore used the moment M_o estimated from the data after 1998 to calibrate the JMA magnitude with a linear regression:

$$\log M_0 = 0.95 M_j + 9.9 . \qquad (13)$$

Equation (13) is very close to what *Abercrombie* [1996] observed in Southern California. The above relationship was then used to estimate M_o from M_j for events that occurred before 1998. Assuming a circular rupture model, we can estimate rupture radius, a, from

M_o under a given stress drop ($\Delta\sigma$) by using the equation from *Kanamori and Anderson* [1975]:

$$a = \left(\frac{7M_0}{16\Delta\sigma} \right)^{\frac{1}{3}}. \quad (14)$$

2.7 Results and Discussions

Within the 21,000 microearthquakes we found only 807 similar events. These similar events comprise 278 doublets and 62 multiplets. The ratio of similar events to the entire seismicity (<4%) is extremely low compared to those found on the San Andreas Fault near San Juan Bautista and in southern California [*Rubin and Gillard*, 2000; *Shearer et al.* 2005] where over 60-70% of the seismicity were identified to be similar events. All the doublets and multiplets in our study area occurred within a few days. The locations of the similar events appear to be random (crosses in Figure 2.1). There is, however, a narrow peak in the distribution of normal distance of these similar events to the fault plane (Figure 2.7a). Such a peak can also be seen from the entire seismicity (Figure 2.7b), although there is a small shift in the location of the peak. We interpret this peak as the true location of main shock fault.

We found that relocation errors are generally in the range of several meters to a few tens of meters depending mainly on the uncertainties in the delay time measurements and station coverage. As mentioned in the previous section, we saw a systematic difference in delay times measured from the first half cycle and the whole wavelet (Figure 2.3).

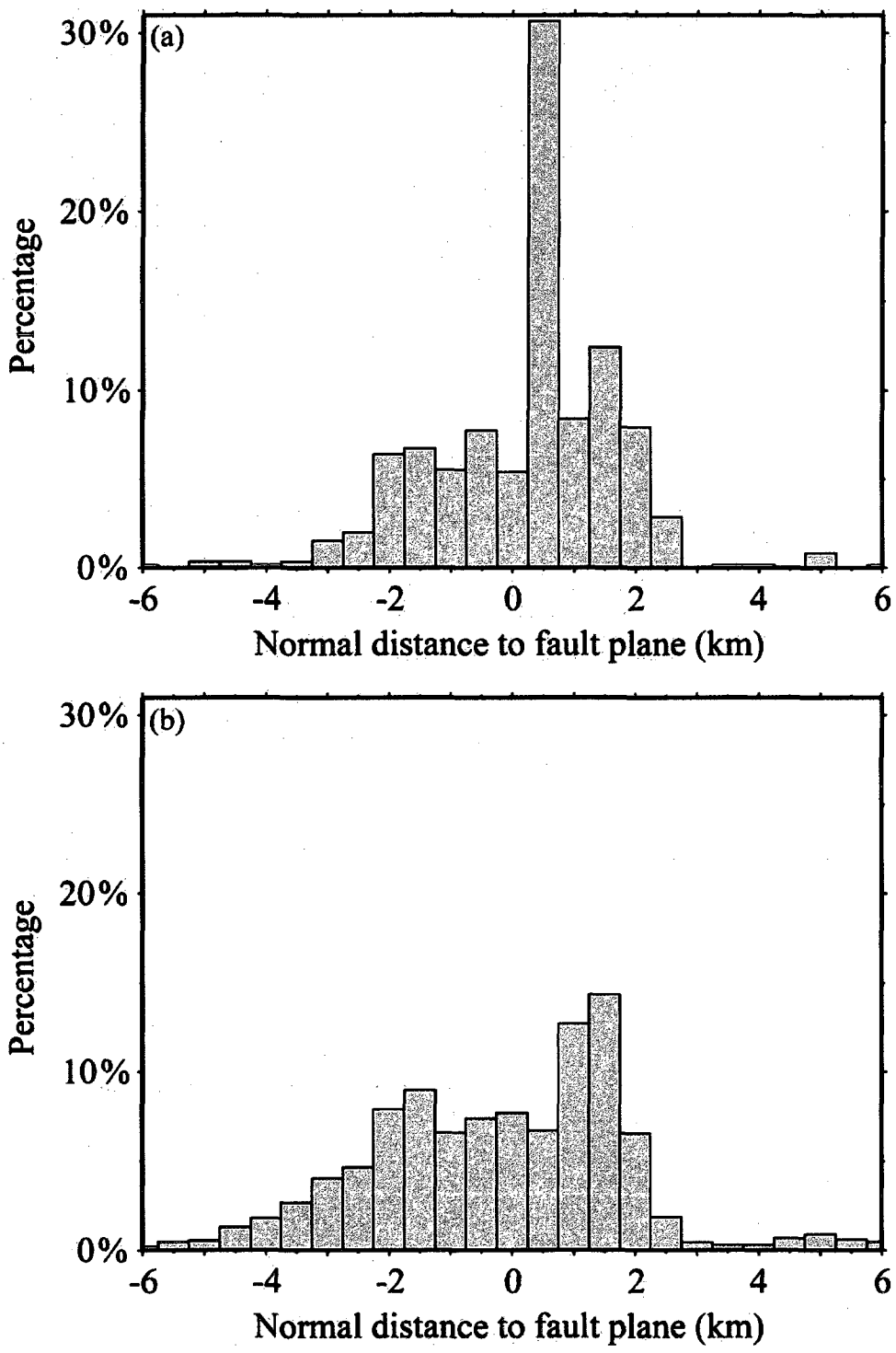

Figure 2.7 Histograms showing the distributions in the normal distance to the fault plane of the 1984 earthquake for the similar events (a), and the entire seismicity (b). Note there is peak around 0.5 km, which we interpret as the real fault zone of the earthquake.

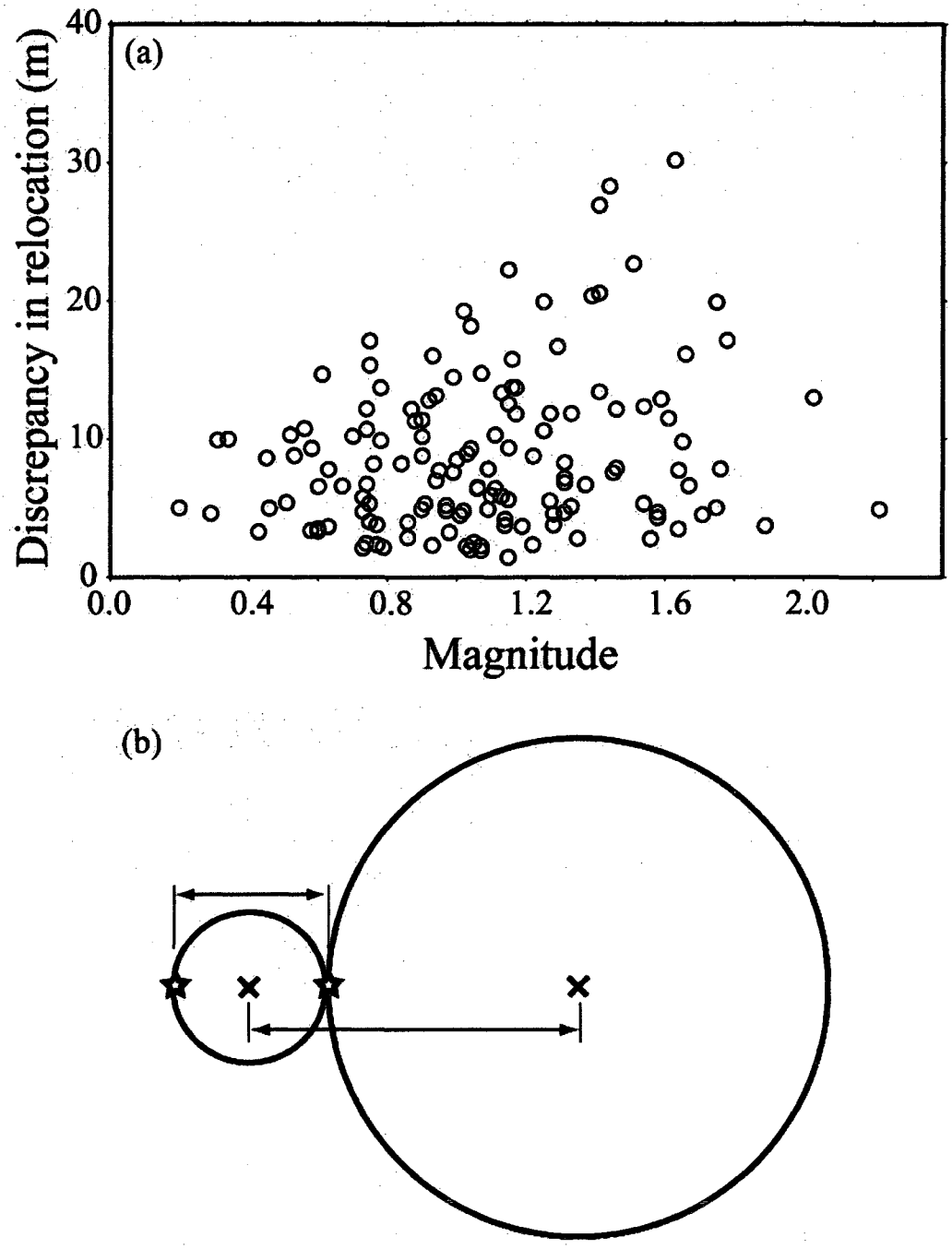

Figure 2.8 (a) Discrepancy in the relative locations arising from choosing different time windows. It appears to increase with the magnitude of the larger event in the pair. The two time windows are indicated in Figure 2.2. (b) Schematic diagram showing discrepancy in relative locations between rupture initials and centroids. This discrepancy is most likely due to the finite-size nature of earthquake ruptures.

We performed a second relocation with the delay times measured from the short time window and found a discrepancy as much as 30 meters from the locations estimated from the *S-P* times measured from the 0.15 s window. We also found that the discrepancy roughly increases with the magnitude of the larger event of the pair (Figure 2.8). In general, the magnitude difference between the two events in a pair also shows an increase with the larger event size. An increase of magnitude difference could result in a decrease of waveform similarity and therefore an increase of measurement error in delay time and event location. The average cc of each pair, however, does not show any dependence on event magnitude. It is thus hard to explain the above observation solely by an increasing of location error with event magnitude. We speculate that the observed discrepancy may reflect the finite-size nature of earthquake ruptures. It is likely that the short time window measures the relative location between the initial points, while the long time window gives the relative locations of the centroids and the two could be different.

To obtain a better comparison between event distances and their rupture sizes, we first projected the relative location vectors onto the 1984 earthquake fault plane and its normal direction (Figure 2.9). It is conceivable that the rupture planes of the events within the fault zone are probably more or less parallel to the 1984 fault plane whereas the others could have more random fault planes. We thus divided the similar events into "on fault" and "off fault" groups and projected them separately. In general there is no significant difference between the two groups in distribution of distance and colatitude. Distance between the consecutive pairs varies from ~5 meters to ~100 meters with a peak around 20 meters (Figures 2.9a and 2.9d).

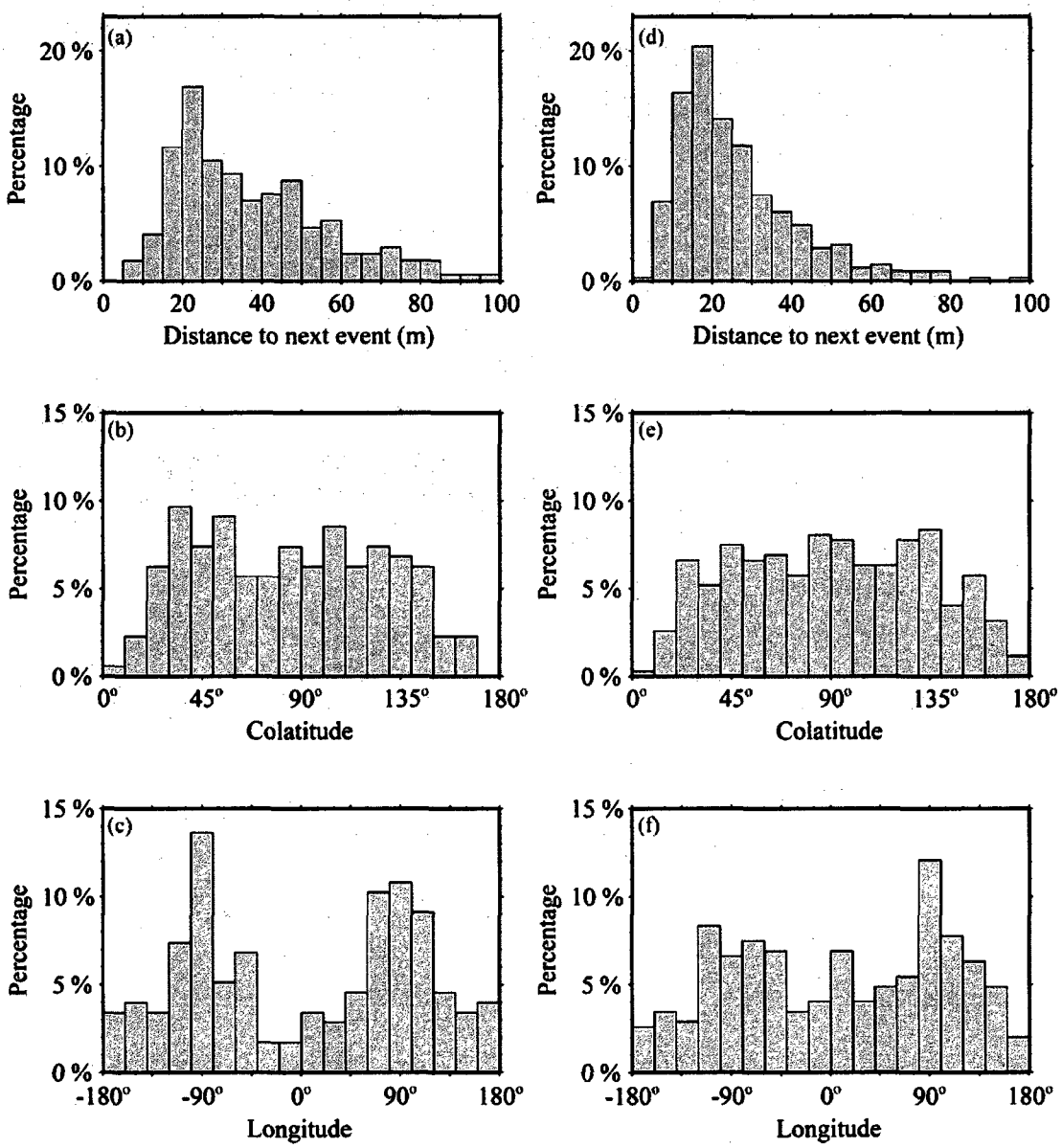

Figure 2.9 Histograms showing the distributions of the relative location vectors in amplitude, colatitude and longitude for the "on fault" (a, b, c) and the "off fault" events (d, e, f). The colatitude and longitude are defined in a spherical coordinate with the fault normal as pole and the fault plane as equator. Colatitude is the angle between the relative location vectors and the fault normal. The longitude is defined as the clockwise angle between the projection of the relative location vector onto the fault plane and the downdip direction. Note the relative location vectors of the "on fault" events show a relatively even distribution in colatitude direction (b) and are concentrated in the strike direction (c).

The relative location vector shows an even distribution in colatitude direction (Figures 2.9b and 2.9e), suggesting the fault planes of these small events are either not on the same plane or not parallel to the main fault. There is, however, a clear pattern in the distribution of longitude for events near the main fault plane. The second rupture tends to occur along the strike direction (Figure 2.9c), which is not seen in the case of the "off fault" events (Figure 2.9e). Recent studies [e.g., *Stein*, 1999] have shown that the spatial distribution of aftershocks agrees well with the rupture-induced change in Coulomb stress. If this is true, then our observations on the spatial distribution of the immediate aftershocks suggest that most of the "on fault" earthquakes are strike-slip events whereas the "off fault" ones are not necessarily strike-slip events.

Following *Rubin and Gillard* [2000], we plotted the distance to the second events as a function of the magnitude (M_j) of the first event (Figure 2.10a). Here the "on-fault" and "off-faults" events are shown separately. It appears that there is a minimum distance for each magnitude and the value of this minimum distance increases with magnitude (Figure 2.9a). There is also a systematic difference between the two groups of events. The "on fault" group (solid squares) has a relatively larger low cut compared to the "off fault" group (open circles). For comparison we have also shown the rupture radii for a circular fault model calculated from a stress drop of 10 MPa (solid line) and 50 MPa (dashed line) in Figure 2.10a. They correspond roughly to the minimum distances of the two groups. The linear trends of the low cut thus suggest that these similar events should be considered as consecutive events rather than repeating earthquakes.

This can be further confirmed by projecting the "normalized" relative location vectors onto the fault plane (Figure 2.10b). A colatitude range of 60°-120° was used here in

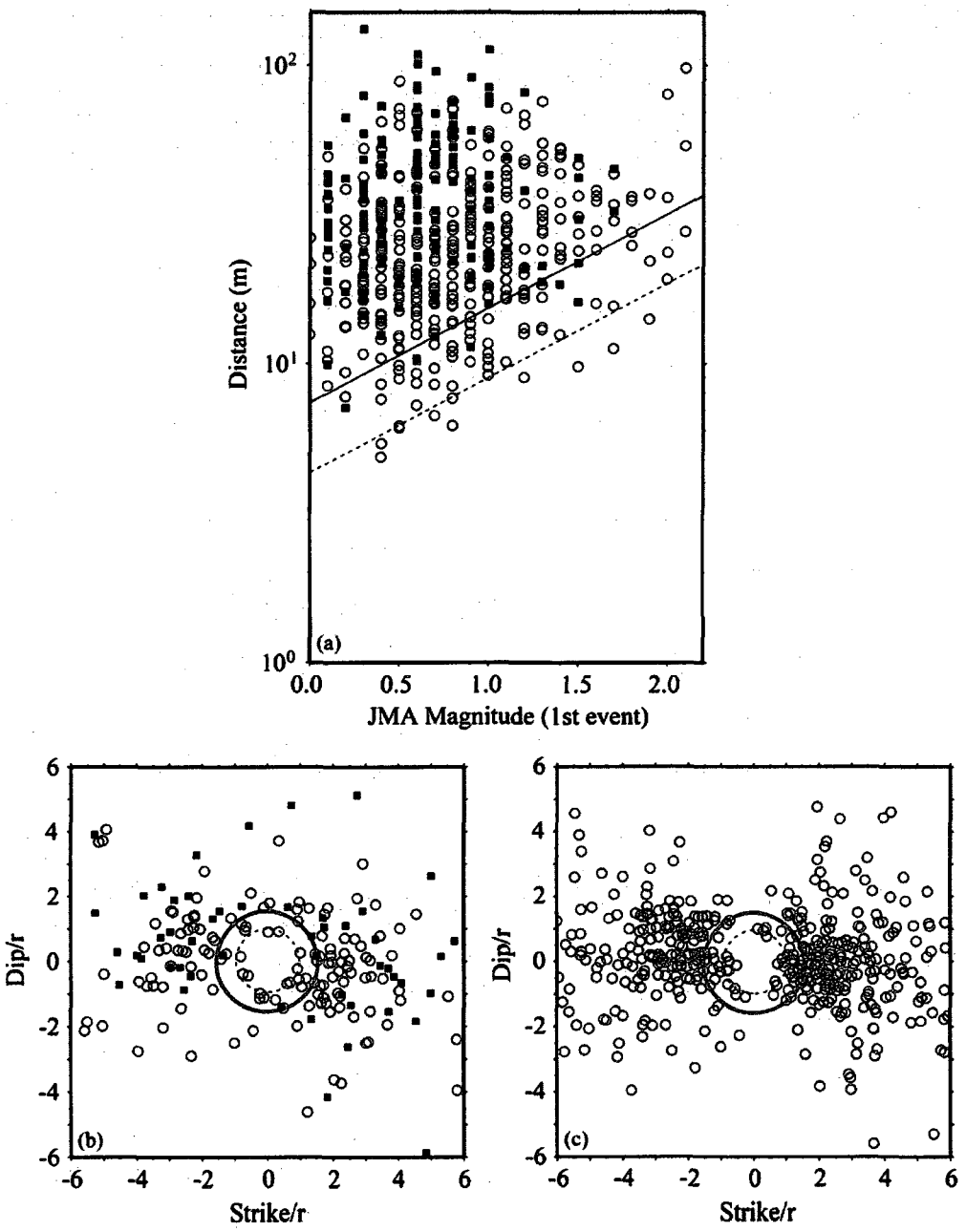

Figure 2.10 (a) Distances between consecutive earthquakes are shown as a function of magnitude of the first events. The solid and dashed lines denote the rupture radii calculated from stress drops of 10 MPa and 50 MPa, respectively. The "on fault" and "off fault" events are shown in solid squares and open circles, respectively. (b) The normalized relative location vectors are projected onto the fault plane. A colatitude range of 60°-120° are used in selecting the pairs. The rupture radii corresponding to a stress drop of 10 MPa and 50 MPa are shown in solid and dashed line circles, respectively. The latter is used in the normalization. Note the small "hole" in the center of the plot. (c) Same projection as (b) to vertical fault planes containing the relative location vectors.

selecting the events. The rupture radii corresponding to a stress drop of 50 MPa were used in the normalization. Again the two groups are shown in separately. The solid circle denotes the rupture area for a stress drop of 10 MPa. We can see a small "hole" in the center of plot. Most of the events are located outside the unit circle (dashed line) whereas all "on fault" events lie further out of the 10 MPa circle. If we assume that the similar events have vertical fault planes containing the relative location vectors, we can also confirm the presence of the central hole in a similar projection for all the similar events including those outside the 60°-120° colatitude range (Figure 2.10c).

We assumed that the identified doublets and multiplets share the same rupture planes when we used the minimum distance to infer stress drop in Figure 2.10. Here we argue the validity of this coplanar assumption from the following two aspects. First, *Yukutake et al.* [2006] found that most of the "on fault" earthquakes are strike-slip events with fault planes more or less parallel to the main shock fault plane. So if the coplanar assumption is valid, then the relative location vectors should also align with the main fault plane, which is not shown in the locations that best fit the *S-P* times (Figure 2.9). It is, however, possible to find relative location vectors aligning with the main fault within the uncertainties in *S-P* times (Figure 2.5). With a conditional inversion, we can obtain a set of location vectors that exhibit a well defined 90° spike in colatitude direction, suggesting that most of the location vectors are also parallel to the main fault plane (Figure 2.11). Second, if the multiplets are coplanar, then the relative location vectors among the earthquakes must lie within the same plane. We applied a multivariable regression to determine how well these vectors are confined in a plane.

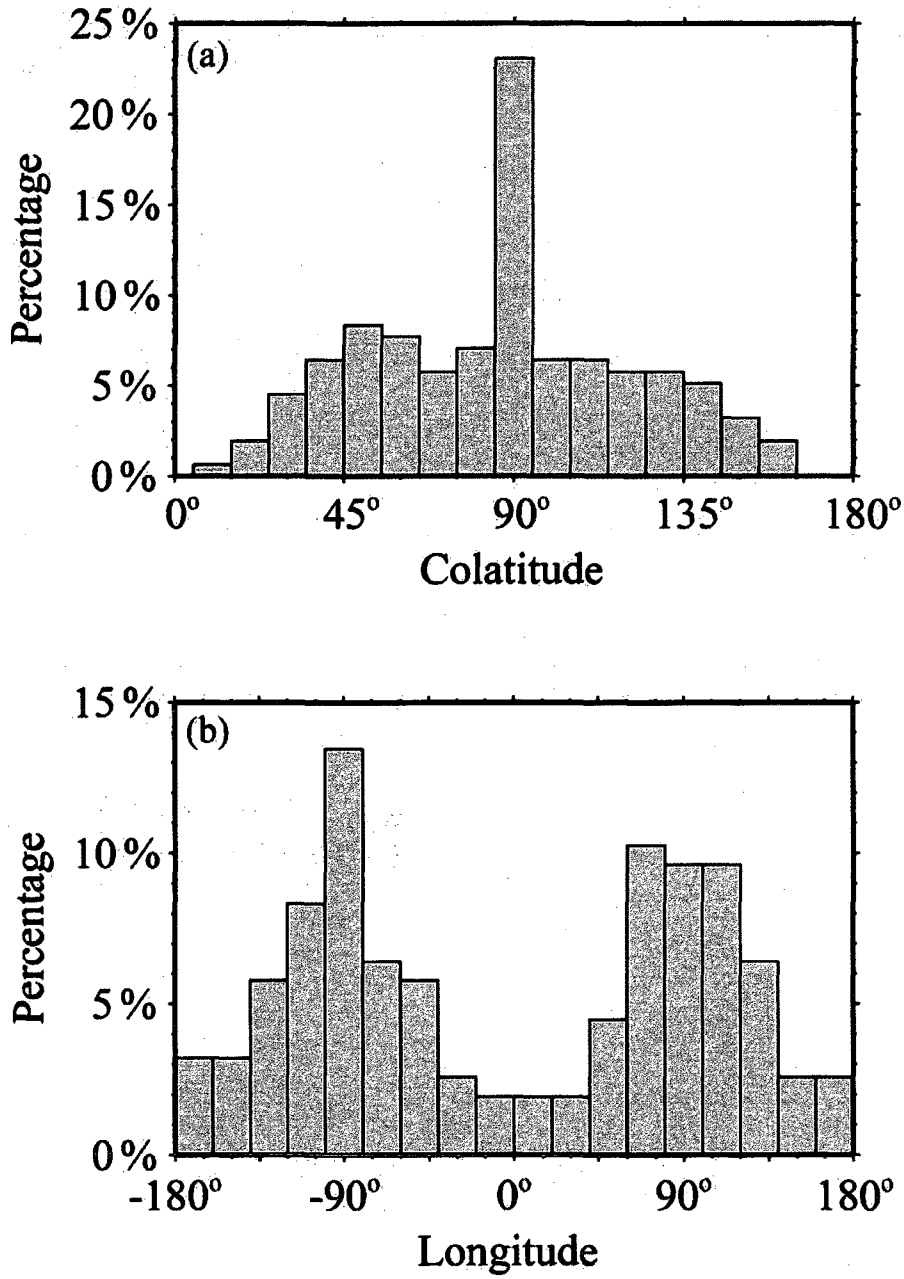

Figure 2.11 Histograms showing the distributions of the relative location vectors in colatitude and longitude with a conditional inversion. Note the large 90° spike in colatitude direction (a) and the relative concentration in the strike direction (b).

The R-square of the largest 6 multiplets (the largest multiplet in our dataset consists of 10 events) varies from 0.71 to 0.97 with an average of 0.84, so we concluded that the vectors in each multiplet are indeed located in the same plane.

The lack of repeating earthquakes could have many reasons. Our catalog covers only 6 years and it might be not long enough to observe earthquake repeating when the tectonic loading rate is low. Recurrence intervals observed at San Andreas Fault vary from days to years depending on event size [*Nadeau and McEvilly*, 1999; *Peng et al.*, 2005]. *Waldhauser and Ellsworth* [2002] found a repeat rate of approximately 6 years at an observed surface creep rate of about 5 mm/year (long term 9 mm/year) when they study the Hayward fault, California. *Kimata et al.* [2004] observed an uplift of 3-6 mm in the study area during 2002-2004. If the same deformation rate is present before 2001 (this is probably true because there is no significant increase of seismicity in 2002-2004), then we would expect microearthquakes to repeat within the 6-year period, even if we assume a loading rate that is 10 times lower than that of the San Andreas Fault. We thus attribute the lack of repeating earthquake to the absence of a weak damaged zone along the main fault, which undergoes stable creep under steady tectonic loading. This weak zone is seismically distinct from the wall rocks by a reduced velocity of a few tens of percent [*Li et al.*, 2003] and produces characteristic propagation signals, such as fault zone trapped waves. Fault zone trapped waves arise from coherent reflections between fault zone and wall rocks and have relatively large amplitude and long durations [*Li et al.*, 2003]. We found no evidence for such trapped waves associated with the main fault, suggesting that the damage zone of the 1984 earthquake has been healed almost completely. There are

also no distinct low velocity anomalies near the fault in our preliminary tomographic images [*Cheng et al.*, in preparation].

Our observations on the distances between consecutive pairs, however, are consistent with what *Rubin and Gillard* [2000] have observed at the San Andreas Fault, suggesting rupture physics between the two different fault systems is probably the same. The lack of "immediate" repeaters is further used by *Rubin and Gillard* [2000] to argue that microearthquakes they have studied are probably not triggered by the model proposed by *Segall and Rice* [1995]. In this model changes in pore pressure associated with coseismic slip and the postseismic fluid diffusion are used to explain the stabilization of one rupture and a subsequent immediate recurrence. We thus conclude that this model does not work in our study area either.

If we assume that the observed minimum distances reflect the rupture size of the first events, by using equation (14) we obtained a stress drop of 10 MPa for the "on fault" group and 50 MPa for the "off fault" group, respectively. Since we have assumed that the consecutive event pairs occurred on the same fault planes and that these planes are parallel to the 1984 earthquake fault, our estimates presented here represent the upper bound of the stress drops. It is very likely that the above assumptions are more valid for the "on fault" events. We thus consider the 10 MPa is more representative to the corresponding stress drop of these microearthquakes. Because of the assumptions and the small amounts of the pairs used here it seems to be difficult to argue whether or not this stress drop depends on event size from the minimum distance versus magnitude relationship.

The estimated stress drop here is consistent with the observation of *Rubin and Gillard* [2000]. They obtained a maximum of 10 MPa stress drop at the San Andreas Fault, while the median stress drop at the San Andreas Fault estimated by *Abercrombie* [1995] is about 3 MPa. Using the same dataset, *Stork and Ito* [2004] and *Imanishi et al.* [2004] have estimated the stress drops for these microearthquakes to be in the range of 0.01-10 MPa and 0.1-2 MPa, respectively. Our estimate is several times larger than their values. Since there are large uncertainties in estimating the corner frequency, ω_c in fitting spectra, the stress drops calculated from it could have very large errors. Also in our method we have assumed that the observed minimum distance equals to the rupture radius of the first event, this could be inappropriate if the second rupture occurred in a different plane from the first one. In addition, if the slip along the fault is very heterogeneous, it will result a large deviation between the slip centroid and the center of the rupture area. Considering the above facts, we conclude that the discrepancy from the two methods is not significant.

2.8 Conclusions

We have investigated the spatial and temporal distribution of similar microearthquakes occurred at the aftershock zone of the 1984 western Nagano earthquake in Central Japan to understand fault evolution and rupture interactions. We found no evidence for repeating earthquakes at this intraplate fault. Together with other seismic investigations, we attribute the lack of repeating earthquakes to the absence of low velocity damage zone along the fault. We observed a total of 807 similar events in the period of 1995-2001, which accounts for less than 4% of the total seismicity. These events occurred very closely in time, ranging from a few seconds to days. Precise

relocation showed that these events are separated by a few meters to about one hundred meters. There is a clear lower bound in distance between events and the minimum appears to be proportional to the size of the first events. By assuming the minimum distances as the rupture radii, we obtained a maximum stress drop of 10 MPa for these events.

Acknowledgments. We thank the National Research Institute for Earth Science and Disaster Prevention of Japan for providing the data. The Associate Editor, Dr. Felix Waldhauser, and two reviewers, Drs. Allan Rubin and Yong-gang Li provided very constructive reviews that improved the manuscript significantly. This work was supported by NSF Grants EAR-0352134 and EAR-0352119.

2.9 Appendix A

Error Estimation of Time Delay

Following *Aki and Richards* [1980] we assume that a seismogram *d(t)* consists of signal *s(t)* and noise *n(t)*:

$$d(t) = s(t) + n(t). \tag{A1}$$

In the frequency domain equation (A1) can be written as

$$|D(\omega)|\exp[i\varphi_d(\omega)] = |S(\omega)|\exp[i\varphi_s(\omega)] + |N_T(\omega)|\exp[i\varphi_n(\omega)]. \tag{A2}$$

Here the noise spectrum is estimated in a time window before the first arrival. For small $|N_T(\omega)|/|S(\omega)|$, the measured phase from the data is

$$\varphi_d(\omega) = \varphi_s(\omega) + \frac{|N_T(\omega)|}{|S(\omega)|}\sin[\varphi_n(\omega) - \varphi_s(\omega)]. \tag{A3}$$

The second term in the above equation is the phase fluctuation due to the noise. For a white noise *n(t)*, $\varphi_n(\omega) - \varphi_s(\omega)$ is randomly and uniformly distributed from 0 to 2π, error in $\varphi_n(\omega) - \varphi_s(\omega)$ thus can be calculated as:

$$\Delta\varphi_{RMS} = \frac{1}{\sqrt{2}}\frac{|N_T(\omega)|}{|S(\omega)|}. \tag{A4}$$

If we assume the dominant angular frequency of the signal is ω_0, then error in the time delay measurement is

$$\Delta t_{RMS} = \frac{\Delta\varphi_{RMS}}{\omega_0} = \frac{1}{\sqrt{2}\omega_0}\frac{|N_T(\omega_0)|}{|S(\omega_0)|} = \frac{1}{\sqrt{2}\cdot\omega_0\cdot SNR}, \tag{A5}$$

where *SNR* is the signal-to-noise ratio.

Chapter 3

Seismic imaging of scatterer migration associated with the 2004 Parkfield earthquake using waveform data of repeating earthquakes and active sources

3.1 Abstract

We use borehole records of four repeating earthquake clusters and two explosive sources to investigate temporal and spatial varying seismic scattering properties at the Parkfield region of the San Andreas Fault associated with the September 28, 2004 *M* 6 Parkfield earthquake. A systematic temporal variation is observed in both seismograms of the repeating earthquakes and the explosions that occurred before and immediately after the 2004 Parkfield earthquake. We use a technique based on de-correlation index from running window cross-correlation measurements to locate the "source" of the temporal variations present in the waveform, i.e., "moving" scatterers. A synthetic test demonstrates the method's capability to distinguish subtle variations in waveform introduced by source location, background velocity and localized velocity change. Application of the method to loosely co-located explosion data reveals a consistent scatterer migration imaging with the result from repeating earthquakes data using traditional differential seismograms. A co-seismic "moving" scatterer is observed within the fault zone of the San Andreas Fault at ~3 km depth beneath Middle Mountain area. The location of the moving scatterer is near the same region reported by *Niu et al.* [2003], which was coincident with a well documented 1993 aseismic transient. The scattering waveform variations are most clearly observed with *P* to *S* or *S* to *S* converted phases for repeating earthquakes data and with *P* to *S* converted phase for active source data. We

speculate that the observed scattering properties change is the result of fluids charge or discharge in fractures caused by the 2004 Parkfield earthquake.

3.2 Introduction

With important implications for earthquake forecasting and hazard evaluation, characterizing fault evolution in terms of stress and strain field change through strikes of large earthquakes has been a long time goal of earthquake seismologist. While the surface strain field is observable by geodetic instrumentation, such as GPS and strainmeters, *in-situ* measurements of stress and strain field at seismogenic depth are still difficult to obtain. One approach is to examine temporal variations in the *P*- and *S*-wave coda since they repeatedly sample the same region in space. Laboratory studies have shown that the elastic properties of crustal rocks clearly exhibit stress dependence attributed to the stress-induced opening or closing of fluid-filled cracks [*Walsh*, 1965; *Scholz*, 1968; *Nur and Simmons*, 1969; *O'Connell and Budiansky*, 1974]. Thus, in principle, seismic coda wave has the capability to detect stress field evolution due to changes in crack properties.

To monitor such stress-induced temporal variations, a highly repeatable powerful source, either natural or artificial, that can propagate through the media to generate similar waveform data is required. One natural source is repeating earthquakes, which are believed to occur on the same patch of a fault plane with the same source mechanism at different time [e.g., *Nadeau et al.*, 1995]. When recorded at the same station, they produce highly similar seismograms. Recent development of earthquake relocation techniques based on waveform cross-correlation and the double-difference algorithm [e.g., *Waldhauser and Ellsworth*, 2000] significantly improves earthquake relocation

precision which leads to the discovery of many repeating earthquake clusters. Observations were reported in several sections of the San Andreas Fault [e.g., *Nadeau et al.*, 1995; *Rubin and Gillard*, 2000] and in subduction zones, such as in northeast Japan [*Igarashi et al.*, 2003]. Although the high similarity of waveform of repeating earthquake clusters, there are still subtle differences in the seismograms that reflect temporal-varying media properties sampled by waves propagating through it. By examining the changes in lapse time for the *S* wave and its associated coda of repeating earthquakes, observations of co-seismic velocity reduction associated with large earthquakes have been reported [*Schaff and Beroza*, 2004; *Rubinstein and Beroza*, 2004a, 2004b, 2005, 2007; *Peng and Ben-Zion*, 2006]. Authors suggest that the observed velocity change caused by strong-motion-induced damage, i.e., crack density, at the very shallow depth, usually only several hundred meters. *Niu et al.* [2003] detected systematic temporal variations in *S*-coda wave of several repeating earthquakes and they interpreted as a "moving" scatterer associated with the 1993 aseismic transient at the Parkfield region of the San Andreas Fault. However, the usage of repeating earthquakes to study fault evolution is limited by the region of their existence and temporal coverage. For example, we usually do not have repeating earthquakes immediately before a large earthquake to produce a perfect event pair cross the occurrence time of the large earthquake to characterize co-seismic change of the fault properties. Also, the repeatability of repeating earthquakes is limited by the amount of loading creeping rate and rock properties. For repeating earthquakes with M ~ 1 at San Andreas Fault, a constant surface creeping rate of 3 cm/year creates a repeating rate about 1 year.

An effective way to expand studies based on repeating earthquakes is using controlled sources such as an explosion or shaker. With the advantage of exactly known source time and position, repeating shots are also capable of monitoring temporal changes of velocity field associated with large earthquakes [*Li et al.*, 1998; *Vidale and Li*, 2003; *Li et al.*, 2006]. Studies of fault zone guide waves and *S*-coda waves by *Li et al.* [1998, 2003 and 2006] reveal a significant co-seismic velocity drop inside a narrow ~200 m fault damage zone and logarithmic time post-seismic velocity healing. They believe the rock damage induced by dynamic rupture of fault zone responsible for the observed velocity change. *Niu et al.* [2008] observed preseismic velocity changes from their cross-well active source monitoring experiment at the Parkfield SAFOD drill site. They reported two large excursions in the travel time of *S* and *S*-coda wave which were associated with two earthquakes. They suggest that pre-rupture stress induced changes in crack properties may responsible for the observed excursions in travel time. They also observed well correlated *S* and *S*-code wave travel time variations with barometric pressure changes at seismogenic depth.

In this study, we use both natural and artificial sources to investigate temporal and spatial varying seismic scattering properties at the Parkfield region induced by the 2004 Parkfield earthquake. A new technique based on coda wave interferometry is developed to image the source of the temporal variations in waveform. We find a systematic pattern in temporal varying scattering properties (i.e., "moving" scatterers) at ~3 km depth in the fault zone of the San Andreas Fault, consistent with data from natural source and artificial source records.

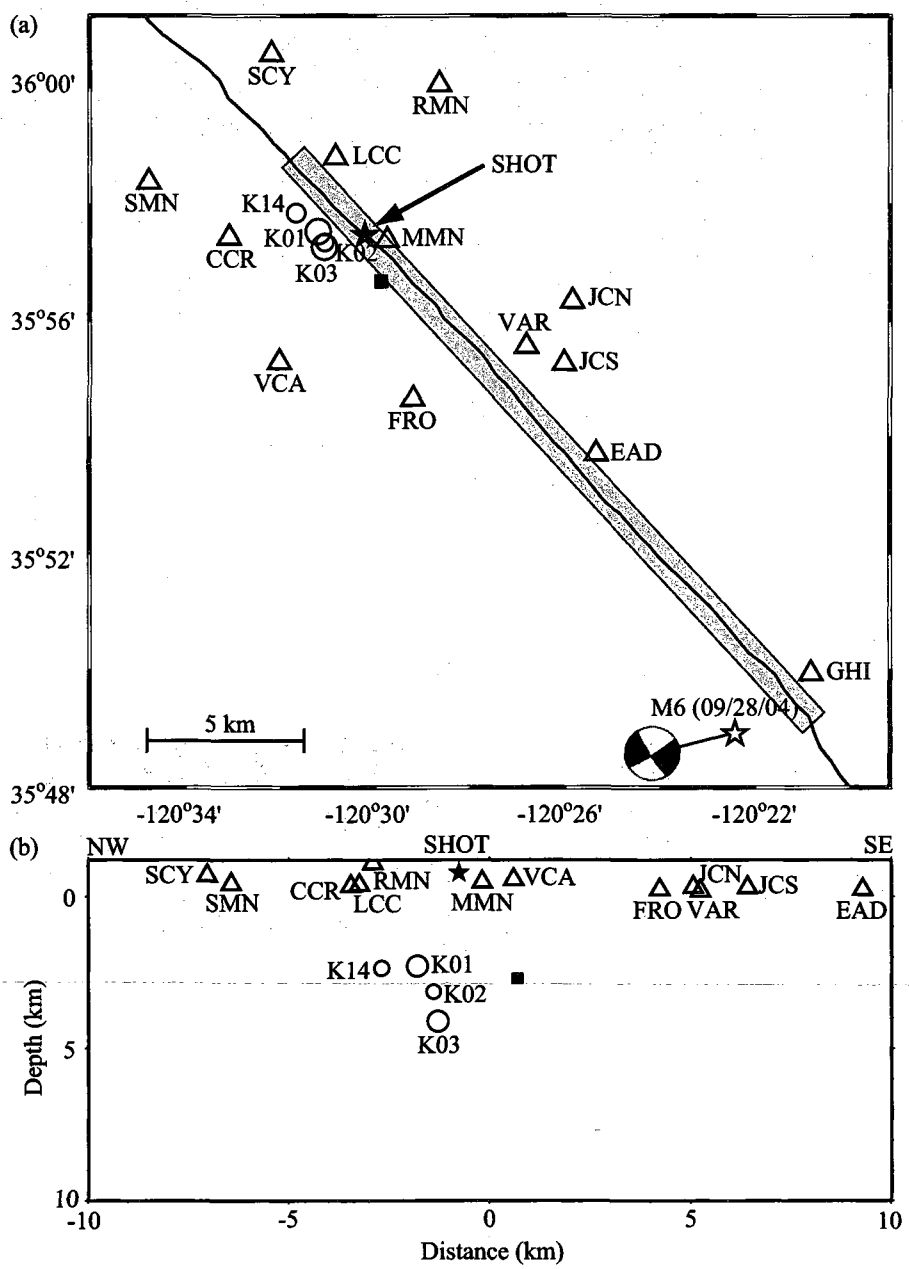

Figure 3.1 Map of the Parkfield study area. (a) map view; (b) fault cross-section view. The three component borehole HRSN stations are shown as open triangles. The open circles show the locations of four repeating earthquake clusters used in this study. The size of the circle indicates the average size of the earthquake in each cluster. The size of the circle indicates the relative size of the earthquake. The black line shows the surface trace of the San Andreas Fault. The black solid star shows the location of explosion shots. The black open star shows the hypocenter of the 2004 Parkfield *M* 6 earthquake. Also shown is the moment tensor solution and the surface rupture zone (gray area) for the 2004 Parkfield earthquake. The black solid square shows the location of "moving" scatterer.

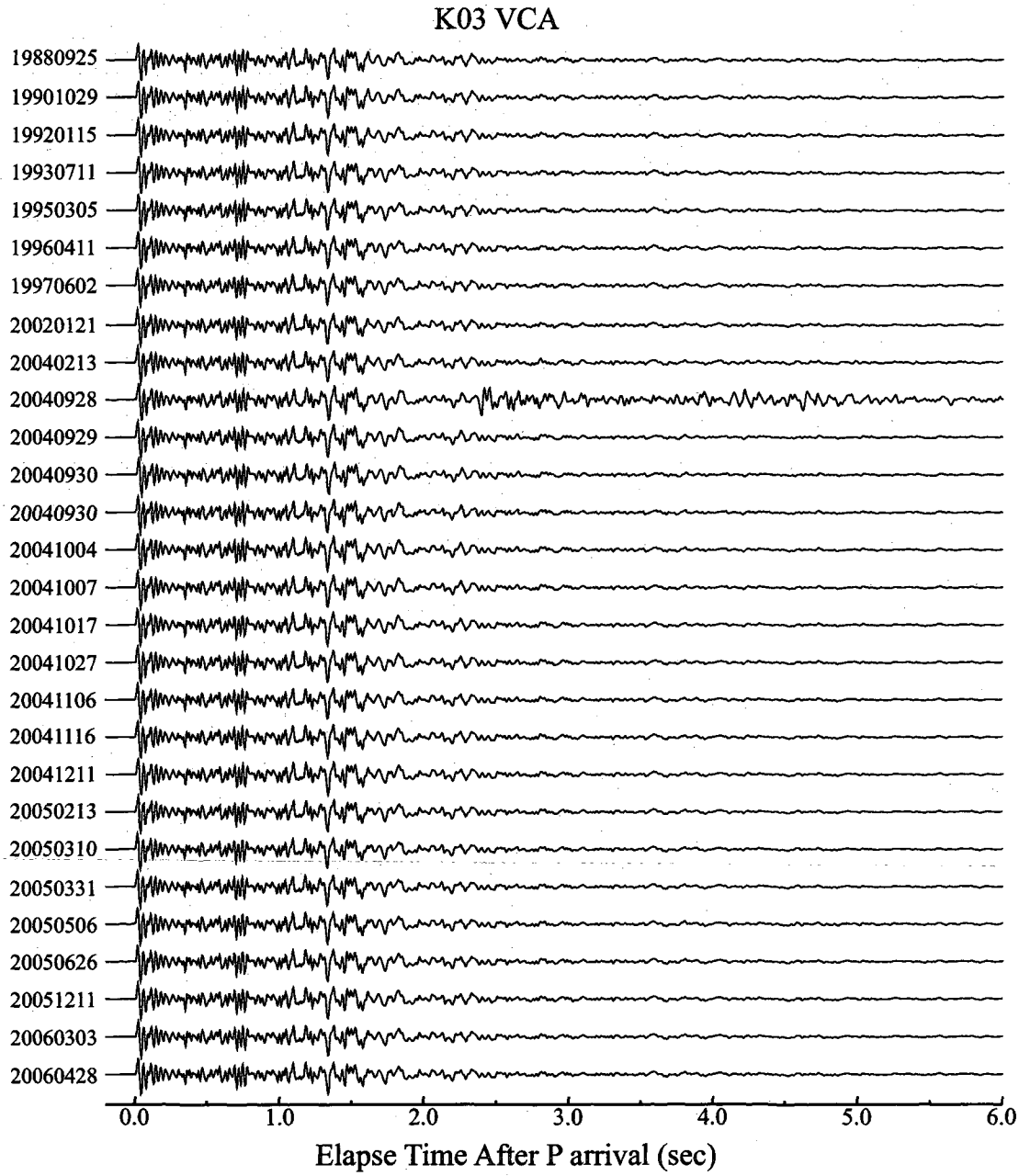

Figure 3.2 Example waveforms of repeating earthquakes. Shown are the vertical-component seismograms for repeating earthquake cluster K03 at station VCA. Waveforms are aligned to the *P* arrival time. Note the extreme waveform similarity throughout the entire 6 s time window. Except events occur on 20040928, 16 minutes after the 2004 Parkfield earthquake, another suspicious aftershock appears about 2.5 sec after *P* arrival.

3.3 Data

For decades, the Parkfield region of the San Andreas Fault has been heavily instrumented, which makes it an ideal natural laboratory for studying temporal variations of fault properties (Figure 3.1). The local High Resolution Seismic Network (HRSN), a borehole station network with 250 Hz sampling rate provide a unique opportunity for the most sensitive temporal wave field variations study. By examining seismograms provided by the HRSN network, clusters of earthquakes with highly similar waveform are reported. Figure 3.2 shows an example of the waveform of repeating earthquake cluster K03 at station VCA, which contain 28 events member covering from 1988 to 2006. Our study employs four repeating earthquake clusters and two explosions recorded by twelve borehole stations (exclude station GHI, which is far away from study area) to monitor the time dependence of seismic scattering properties in this region (Figure 3.3 and Table 3.1). Notice the gray area in Figure 3.3 corresponding an interrupt period of HRSN station operation, no data available during that period caused an apparent gap in repeating earthquakes detection. These four repeating earthquake clusters were used by *Niu et al.* [2003] and we update the catalog to present so that the clusters now include both events before and immediately after the 2004 Parkfield earthquake. The extremely similarity of the waveforms for this four repeating earthquake clusters at all thirteen borehole HRSN stations with difference azimuth guarantied their relative locations are within meters. In addition, on Oct 17, 2002 and Dec. 29, 2004, two chemical explosions were taken in place at our study region and clearly recorded by all the HRSN stations. The location difference of the two explosions was only around ~ 10 meters, they produced very similar seismograms when recorded at the same station.

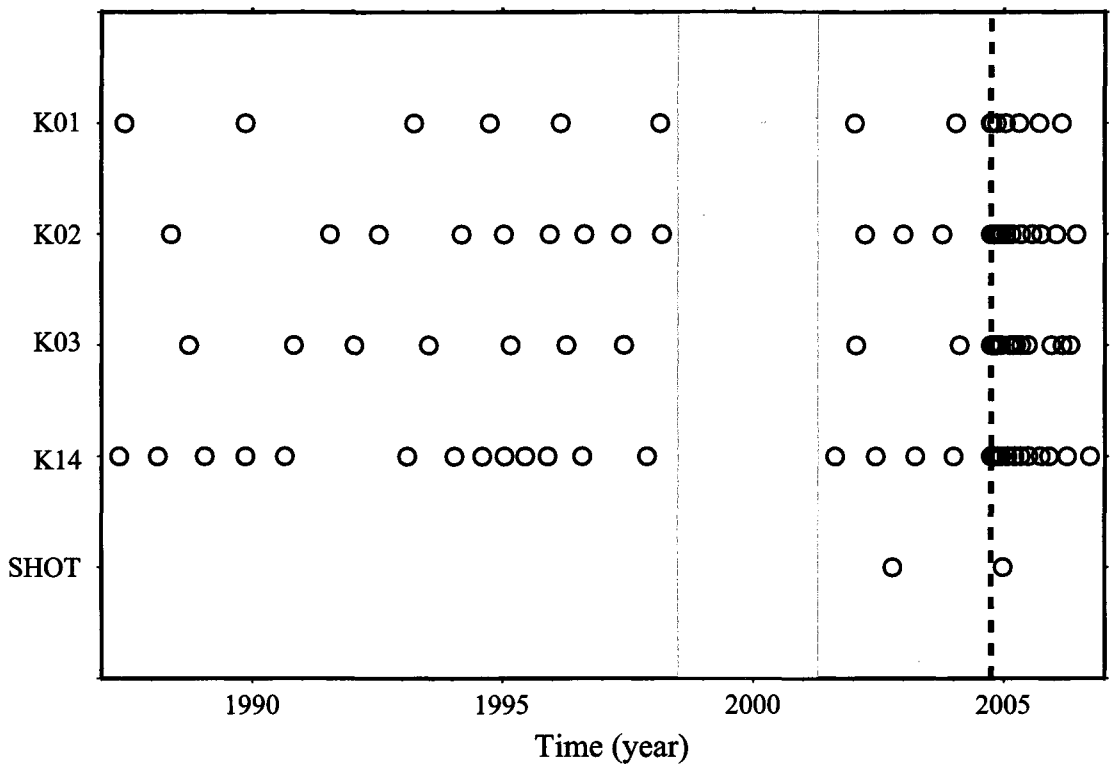

Figure 3.3 Time line of the four repeating earthquake clusters (K1, K2, K3, and K14) and two explosion shots used in this study. The vertical dashed line indicates the time of the Parkfield earthquake. Gray area corresponds to the time period when HRSN stations went offline, which leaves a gap in the catalog of repeating earthquake clusters.

Table 3.1. Average Hypocenters and Magnitudes for Clusters Used[a]

Cluster	Latitude (deg)	Longitude (deg)	Depth (km)	Magnitude
K01	35.958961	-120.520353	2.283	0.982
K02	35.955837	-120.517919	3.134	0.671
K03	35.954549	-120.517996	4.105	0.959
K14	35.964190	-120.527992	2.356	0.702
Shot	35.957916	-120.503967	-0.779	

[a]Average hypocenters and magnitudes are estimated from events member after 2001. Depth is reference to mean sea level.

The unique data set provides us a great opportunity to closely examine earthquake induced change to the fault stress field and perform a calibration between the natural and artificial source record.

3.4 Imaging Scatterer Migration

3.4.1 Repeating Earthquakes

We first chose a reference event for each cluster that all the other members of the cluster are compared with. Since we are mostly interested the temporal and spatial changes included by the Parkfield earthquake, we select events just preceding the Parkfield earthquake as the reference events. Due to the repeatability and availability of the repeating earthquake data, the reference events could be days or months even years before the 2004 Parkfield earthquake. We assume there are no comparable changes in the fault system during the time period between the reference events and the Parkfield earthquake, which is a quite reasonable assumption for a steady slip fault system and also proved by comparing seismograms before the Parkfield earthquake.

In this study we examine only the vertical channel of the HRSN data set for the better signal to noise ratio (SNR). We first filter the data set with a band-pass window of 5 - 35

Hz using a second order Butterworth filter (zero-phase shift). After interpolated all seismogram to 320,000 samples per second with zero padding in frequency domain, we then use cross-correlation technique to align normalized events within each repeating earthquake cluster to subsample precision to a manually picked *P* arrival. We use a cosine fitting method to estimate subsample delay time in time domain [*De Jong et al.*, 1990; *Cespedes et al.*, 1995].

The reason for the alignment is to remove any possible errors in the original time of the earthquake and to reduce the sensitivity of hypocenter location error. Once all the events within each individual cluster are carefully aligned, we constructed a differential seismogram $\delta s(t)$ for each event pair by taking the difference of seismograms before and after the Parkfield earthquake for each station. In principle, only energy from time-dependent physical characteristics, such as changes from scatterer location, strength or localized velocity change near to the scatterer, will be highlighted in differential seismogram. Any energy from the background noise will be removed by this procedure. Figure 3.4 presents the differential seismograms from station RMN and VCA for cluster K01 and K03, respectively. For about two years period from January 2002 to January 2004, events of cluster K01 produce no obvious energy in differential seismogram measurements at station RMN and VCA. The same is also shown in the differential seismograms constructed for events of cluster K03 with a two years interval before the 2004 Parkfield earthquake. However, strong energy appears between the event at January 2004 and the event 16 minutes after the 2004 Parkfield earthquake. Systematic observations across four repeating earthquake clusters and all HRSN stations show as a strong evidence of large co-seismic scattering properties change.

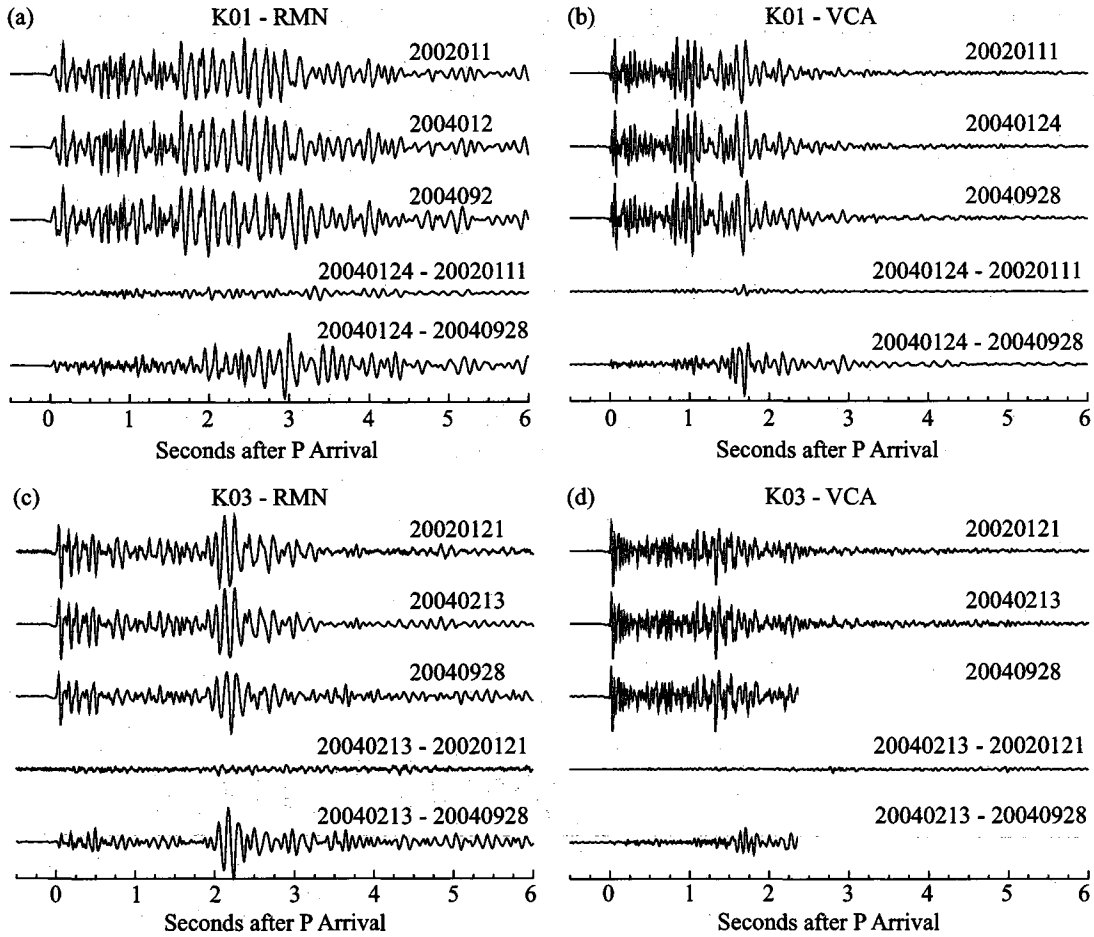

Figure 3.4 Example vertical-component waveforms of repeating earthquake clusters and their corresponding differential seismograms. (a), (b), (c) and (d) show the records of station RMN and VCA for K01 and K03 clusters, respectively. In each subplot, the top three traces show the waveforms before and immediately after the 2004 Parkfield earthquake. The bottom two traces show the differential seismograms constructed from waveforms before and cross the occurrence time of the 2004 Parkfield earthquake. Clear energy emerges in the difference seismogram created across the occurrence time of the 2004 Parkfield earthquake as the indication for co-seismic scattering properties change, which is very stable for the two years period before the 2004 Parkfield earthquake.

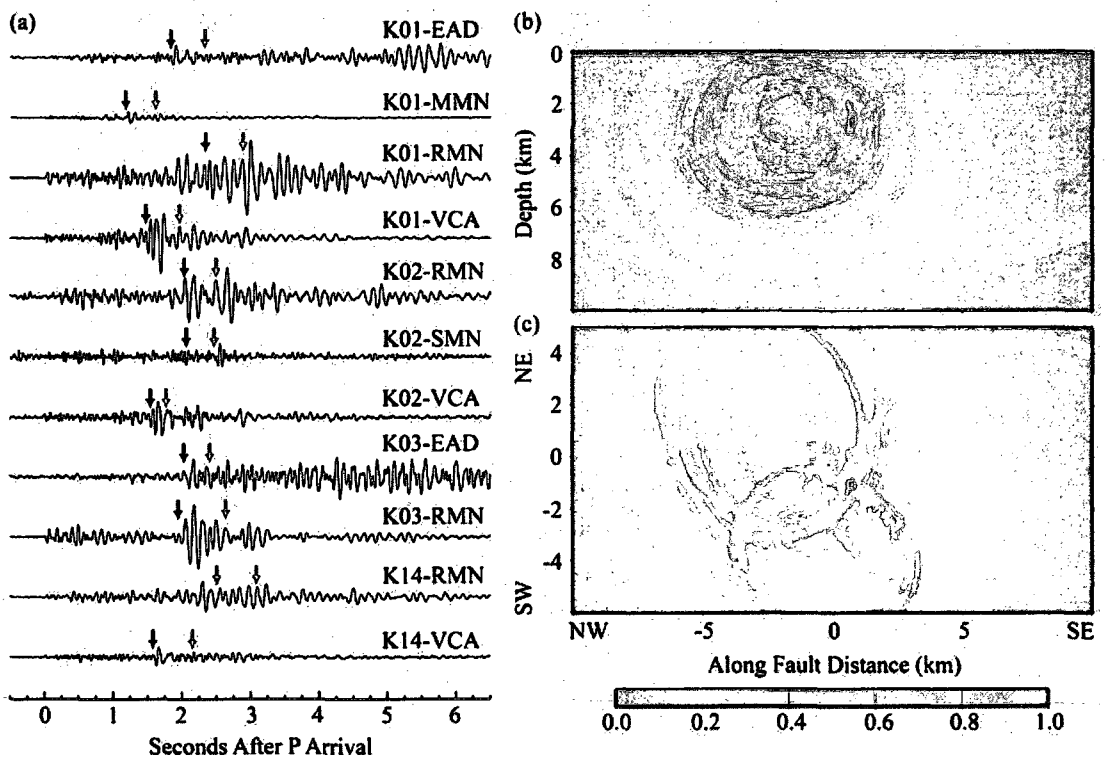

Figure 3.5 Differential seismograms and the imaging of scatterer migration. (a) Vertical-component differential seismograms, which are taken between the events before and immediately after the Parkfield earthquake for four repeating earthquake clusters at several HRSN stations. (b) Cross-section view parallel to the fault and (c) a map view at 3 km depth. Using the differential seismograms shown in (a), the Born approximation migration results in a well defined maximum amplitude area indicating the possible region of the seismic scattering properties change associated with the 2004 Parkfield earthquake. The color bar represents the normalized stacking differential seismogram amplitude. The black and red arrows in (a) indicate the predicted arrival time for *P* to *S* and *S* to *S* converted phase from the "moving" scatterer.

The seismogram from VCA station for cluster K03 on date 20040908 is cut after 2.5 sec since the later waveform is biased by another aftershock as shown in Figure 3.2.

After detected variations in the scattered waveform, we migrate them back to space based on the first order Born approximation (Figure 3.5). A single scattering model is assumed here because of the generally weak scattering effects of the crust and in most cases multiple scattering can be neglected [*Sato and Fehler*, 1998]. By solving eikonal equation based on 3-D *P*- and *S*-wave velocity models [*Michelini and McEvilly*, 1991] *P*- and *S*-wave travel time table are created. The differential seismograms from repeating earthquake clusters were then migrated using

$$A(\mathbf{x}) = \sum_s w_{mn} A_s \left(T_{ij}^{mn}\right) = \sum_s w_{mn} A_s \left(T_{ik}^{m} + T_{kj}^{n}\right) \qquad (1)$$

where m and n represents the *P*- or *S*-wave modes with a combination of *P* to *P*, *P* to *S*, *S* to *P*, *S* to *S* converted phases. T_{ij}^{mn} represents the travel time of mn modes converted phase from event i to station j. k is the location of scattering grid in space. w_{mn} is the weight function for each corresponding converted phase modes. s is the summation over all event-station pairs. Stacking imaging based on *P* to *S* and *S* to *S* modes migration clearly suggests a location of strong scattering properties change at about 3 km depth beneath Middle Mountain area. The predict time for the *P* to *S* and *S* to *S* converted phases are marked with black and red arrows in Figure 3.5a. Comparison between our observations with the "moving" scatterer reported by *Niu et al.* [2003] at the same study region reveals a very consistent pattern. Although in 1993, the "moving" scatterer was coincident with a well-document aseismic event, this time it corresponds to a large nearby earthquake.

3.4.2 Explosion Sources

Two chemical explosions took place in our study area on Oct 17, 2002 and Dec. 29, 2004, crossing the occurrence time of the 2004 Parkfield earthquake. Due to close locations of the explosion, they also produced very similar seismograms when recorded by HRSN stations. Using fault zone trapped waves generated by these two shots, *Li et al.* [2006] reported a ~1% velocity decrease within a ~200 m wide fault zone along the fault strike. Since scattered coda waves are very sensitive to surface environment influence, instead of using surface instrument, here, we try to identify any scattering waveform change due to the co-seismic deformation from borehole records. After filtered the vertical HRSN records for band pass between 1 to 10 Hz, using the first explosion in 2002 as reference, same procedure as used in repeating earthquake clusters study is applied to align them. After all the records for each station are carefully aligned, a running window waveform cross-correlation method [*Niu et al.*, 2003] is used to measure the delay time and evolving de-correlation coefficient of the repeating shot. We compute the delay time $\tau(t)$ and de-correlation index $D(t)$ (defined as 1 minus the maximum cross-correlation coefficient) between the 2004 shot and the 2002 reference shot using a 0.25 sec time window and a running step of 0.02 sec through 6 sec after the P arrival. Differential seismograms are also created for each station. Figure 3.6 shows the example differential seismogram and running window de-correlation measurements at station CCR and VCA. As shown in the differential seismogram the similarity of the repeating shot is not as great as repeating earthquakes, which may partially due to the difference in the source location of the two shots and partially caused by relative large co-seismic rock damage close to surface.

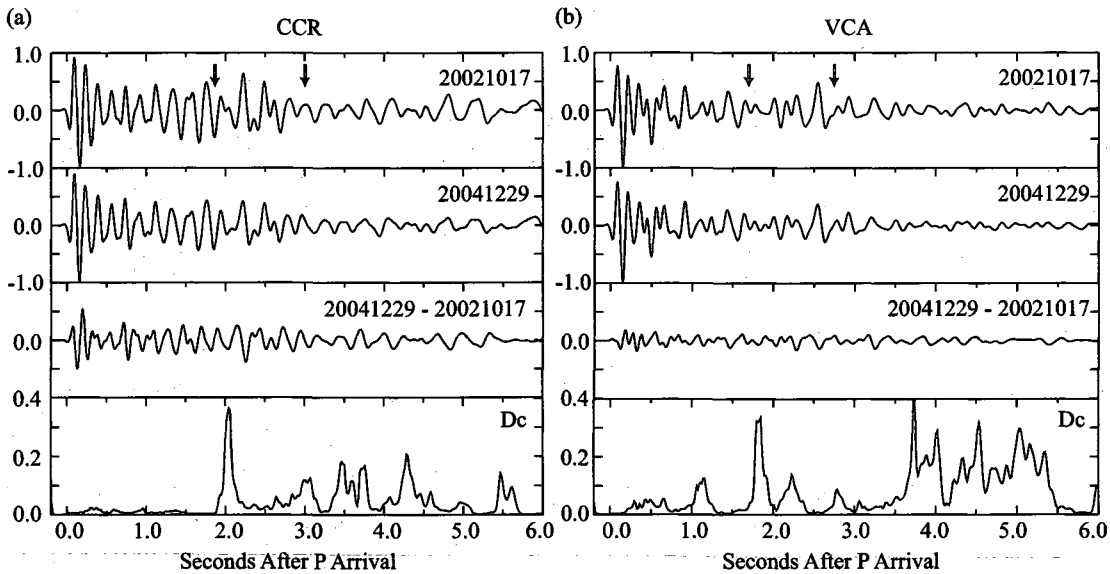

Figure 3.6 Example vertical-component waveforms of repeating explosion shots. (a) and (b) show the records of station CCR and VCA, respectively. Also shown are their corresponding differential seismograms and de-correlation index measurements. The arrows indicate the predicted arrival time for *P* to *S* and *S* to *S* converted phase from the "moving" scatterer observed in Figure 3.5.

A small change of source location, here is around 10 m for our controlled explosion, could introduce significant waveform variations. In addition, large co-seismic velocity reduction at top surface in our study area [*Rubinstein and Beroza*, 2005; *Li et al.*, 2006] may introduce other variations in the differential seismograms. Unlike repeating earthquakes recorded by those borehole stations which are sampling deep portion of the fault, the explosion data inherited significant surface structure and environment noise influence. However, clearly spikes are shown in de-correlation index measurements.

As shown by *Snieder et al.* [2002], while delay time measurements $\tau(t)$ can be interpreted as the mean of travel time perturbation of the each arrival phases τ_i in the time window, de-correlation index can be defined as

$$D(t) = \frac{1}{2}\omega^2\sigma_\tau^2(t) \tag{2}$$

where $\sigma_\tau^2(t)$ and ω^2 are the variance of τ_i and the characteristic angular frequency of the arrival phases, respectively. Thus, a constant background velocity change will lead to a linear trend in $\tau(t)$ and zero response in $D(t)$, given relatively short time window measurements. Using function

$$\frac{\delta v}{v} = -\frac{\tau(t)}{t} \tag{3}$$

linear trend of $\tau(t)$ has been widely used to infer co-seismic fault velocity change [*Schaff and Beroza*, 2004; *Rubinstein and Beroza*, 2005; *Li et al.*, 2006; *Rubinstein et al.*, 2007]. Perturbations of source location will create a constant level of de-correlation index measurements in the coda wave which was used by *Snieder et al.* [2005] to investigate source separation distance for earthquake doublets on the Hayward fault, California. On the other hand, a localized velocity change will introduce a large amount of variance of

travel time perturbation in the arrival phases and result in spikes in the de-correlation index measurements.

Assuming the same location of scattering properties change observed from repeating earthquakes study, black arrows in Figure 3.6 indicates the arrival time of the predicting P to S and S to S converted phases. The time window of the spikes observed in de-correlation measurements matched well with the predicted arrival time of P to S converted phases. We note the suspicious later peaks in VCA station record may be caused by another scattered source and are less reliable for small SNR at large elapse time.

In order to answer whether it is possible to separate the influence of source location, background velocity and localized velocity change, here we present an experiment where synthetic seismograms are computed with an acoustic finite difference algorithm (Figure 3.7). A two-dimensional model of 40 by 21.5 km with a grid size of 20 m is implemented. Unwanted reflections from the boundaries are avoided by the large size of the model and the perfect match layer absorbing boundary on all four boundaries. A Ricker wavelet with a dominant frequency of 8 Hz is used as input source. Following [*Frankel and Clayton*, 1986], we create a Gaussian random medium using,

$$R(r) = \varepsilon^2 \exp\left(-r^2/a^2\right) \qquad (4)$$

where $R(r)$ is the autocorrelation function of distance r, ε is the strength of the heterogeneity and a is the correlation distance or the scale of heterogeneity. A Gaussian random medium with 6 km/s mean, 0.6 km/s standard deviation and 1000 m correlation length is created as the velocity model. 10% fluctuations of the velocity model delivered a realistic scattering medium for our test.

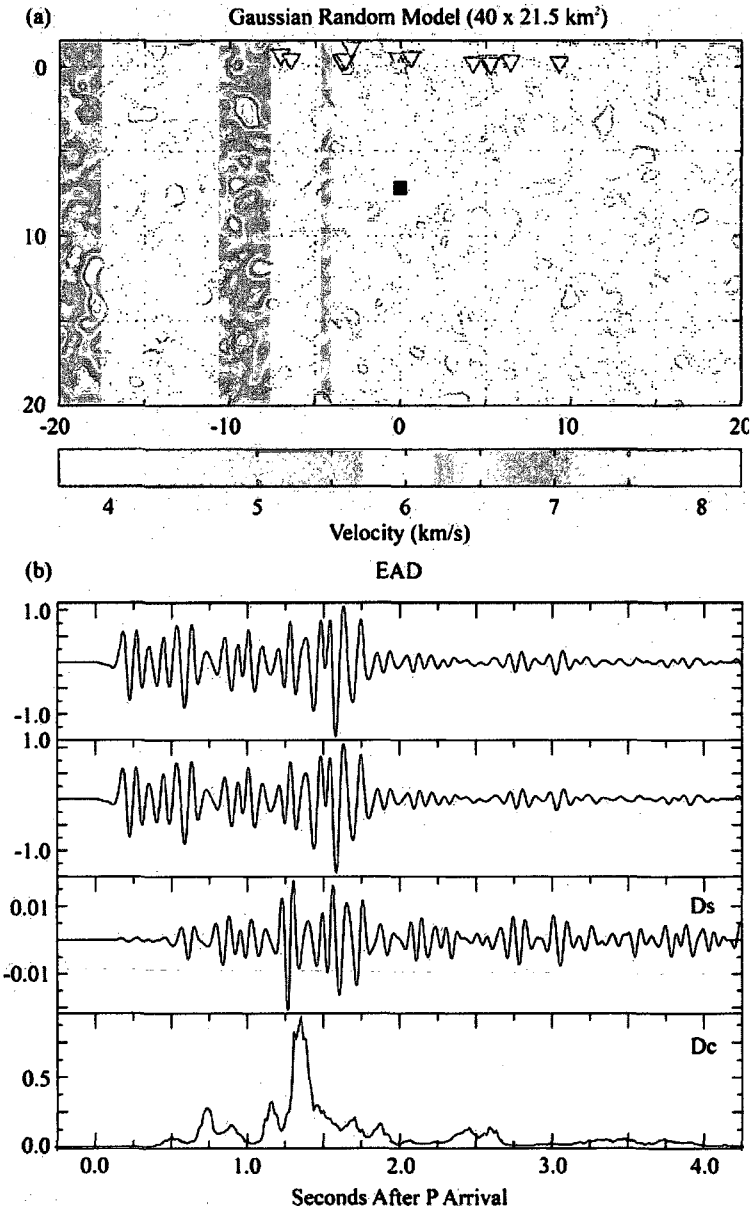

Figure 3.7 Synthetic tests. (a) Gaussian random model used to calculate synthetic waveform. Large model dimension with perfect match layer absorbing boundary at all four boundaries guarantied no reflected artifacts from boundaries in synthetic waveforms. Star shows the location of source. Triangles are the receivers. Black square shows the location of the scatterer. (b) The top two traces show examples of observed waveforms at station EAD before and after introducing source location, background velocity and localized velocity changes simultaneously. The third and fourth traces are the resulting differential seismogram and running window de-correlation measurements from the top two waveforms. Notice the de-correlation index measurements are normalized by waveform SNR and the scale of differential seismograms is around tenth of the original waveforms.

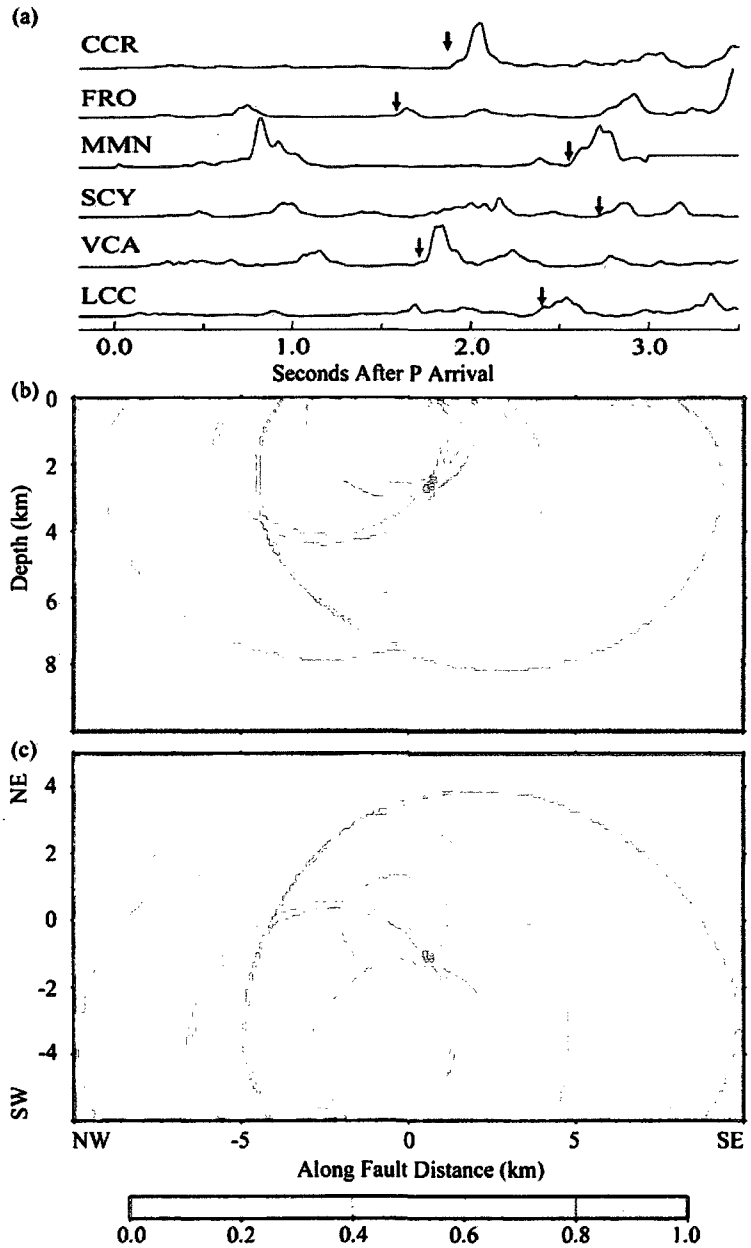

Figure 3.8 Running window de-correlation index measurements of the two explosion shots and the imaging of scatterer migration. (a) Running window de-correlation measurements are calculated from vertical-component seismograms, which are taken between the shots before and after the Parkfield earthquake. (b) Cross-section view parallel to the fault and a map view (c) at 3 km depth. Using the de-correlation index measurements shown in (a), the Born approximation migration results a consistent pattern of seismic scattering properties change at almost the same region as result from repeating earthquakes study. Color bar corresponds to normalized stacking de-correlation index. The arrows in (a) show the predicted arrival time for *P* to *S* converted phase from the observed "moving" scatterer.

By changing the source location by one grid (20 m), decreasing background velocity 0.1% and introducing a strong single scatter with dimension of 600 m and velocity increase 25% into the model simultaneously, synthetic seismograms are calculated and shown in Figure 3.7. The differential seismogram shows that scattered wave variations caused by the strong scatterer are apparently buried in large variations of the waveforms due to source location and background velocity change. It is no longer usable for 4-D type of study in this scheme. However, the maximum de-correlation index successfully detects the time window of the scattered wave (Figure 3.7b).

Using spikes in de-correlation measurements from all stations and with the assumption of *P* to *S* converted phases, we find a well defined location of scattering properties change (Figure 3.8). The predicted time of *P* to *S* converted phases at different stations is also marked in Figure 3.8a on the de-correlation measurements. The location of the "moving" scatterer is very consistent in space with the measurements from repeating earthquakes data.

3.5 Discussion

Following large earthquakes, by studying direct body phases and fault zone trapped wave, *Li et al.*, [1998, 2003 and 2006] observed significant velocity reduction within a ~200 m width highly damaged fault rupture zone. They suggest co-seismic damage of rocks during dynamic rupture responsible for the velocity reduction and the fault rupture zone could extend to as much as 7 km depth.

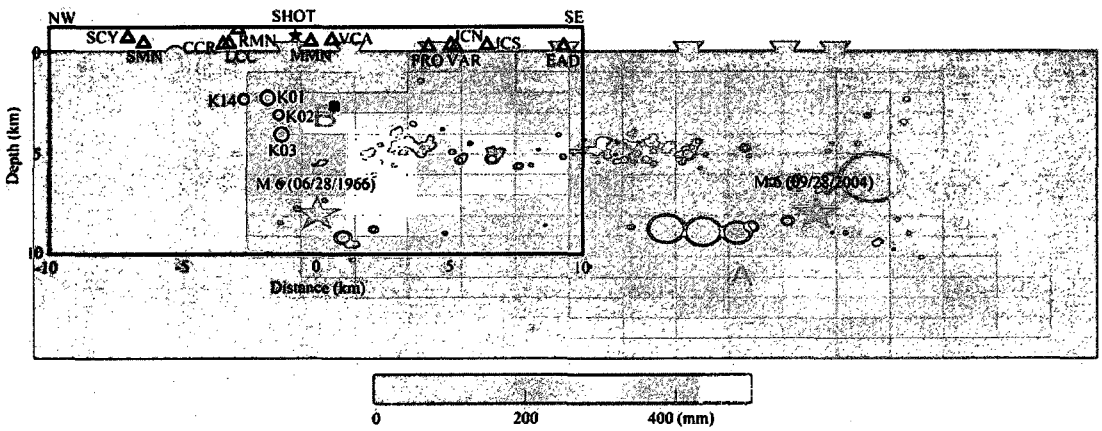

Figure 3.9 Modified co-seismic slip map from *Johanson et al.* [2006], which was inverted from GPS and InSAR data. Two red stars are the hypocenters of the 1966 and 2004 M 6 Parkfield earthquakes. The location of our observed "moving" scatterer is right at the edge of the area with strong co-seismic slip which indicates increased local stress caused by co-seismic slip is the possible explanation for our observation. Background black circles are the aftershocks of the 2004 Parkfield earthquake. The circle size is scaled to the size of the earthquake.

Baisch and Bokelmann [2001] reported seismic scattering change associated with the Loma Prieta earthquake. They suggest that co-seismic deformation caused by a large earthquake leads to crack opening either by local concentration of shear stress or by elevated pore fluid pressure. Our observed temporal varying seismic scattering properties is located at 3 km depth beneath Middle Mountain area, which is right at the edge of significant co-seismic slip area inverted from GPS and InSAR data [*Johanson et al.*, 2006] (Figure 3.9). We believe increasing Coulomb stress at the edge of large amount of deformation zone may responsible for our observed the seismic scattering properties change. Either aseismic slip as reported by *Niu et al.* [2003], or large nearby earthquake as 2004 Parkfield earthquake could introduce re-distribution of stress field near the deformation zone of San Andreas Fault even at great depth. Those localized stress concentrations or releases will lead to open or close partially fluid-filled cracks, hence changing the seismic scattering properties of the rock. During post-seismic healing period, those localized stress could be recovered to pre-seismic state gradually, fluid-filled cracks will then be charged or discharged to the original state too, which will leads to the recovery of variations in seismograms over time.

Rubinstein and Beroza [2005] reported clear co-seismic velocity reduction caused by the 2004 Parkfield earthquake by examining the change in the relative time between *P* and *S* wave for surface and borehole stations. They showed that most velocity reduction was induced by nonlinear strong ground motion from the earthquake and was limited to depth less than 100 m. Consistently, we observed slightly variations in differential seismogram constructed from repeating earthquakes sampling deep fault and large variations in waveform from active shots influenced by shallow structure.

3.6 Conclusion

We inspect temporal waveform variations of four repeating earthquake clusters and two repeating explosions around the 2004 Parkfield earthquake rupture zone. Systematic temporally varying scattered waveforms are detected from both data sets. Differential seismograms from the tightly defined repeating earthquake clusters used in this study provide us an opportunity to image temporal and spatial varying scattering properties close to the rupture zone of a large earthquake. On the basis of coda wave interferometry, we developed a new scatterer migration imaging method to distinguish waveform variations induced by source location, background velocity or localized velocity change. Application of our migration technique to controlled source data reveals a consistent 4-D scattering properties map with the one derived from repeating earthquake clusters. A localized changing of scattering properties, e.g., a "moving" scatterer, is well defined on the fault rupture zone and at 3 km depth beneath Middle Mountain area. From the characteristic frequency (10 Hz) of the observed temporal varying scattered waves, we estimate the dimension of the scatterer to be of the order of 300 m. Strong scattering variations are mostly detected in P to S and S to S scattering modes indicates a most likely cause of S velocity change. To interpret these changes, we suggest a model of co-seismically opened cracks with fluid charge or discharge due to large co-seismic deformation induced by the 2004 Parkfield earthquake. The new technique of imaging scatterer migration developed through this study can be applied to broad regions where relatively loosely defined clusters are available.

Acknowledgments. We thank the Northern California Earthquake Data Center for providing the data.

Chapter 4

Coseismic velocity change during the 2008 Wenchuan earthquake observed from seismic ambient noise

4.1 Abstract

We have investigated the coseismic velocity change associated with the 2008 *M* 7.9 Wenchuan earthquake using continuous records of seismic ambient noise from 16 broadband stations with a temporal coverage of 50 days before and after the occurrence of the Wenchuan earthquake. Rayleigh wave signals between each station pair are extracted by cross-correlation of the daily records of seismic ambient noise wave field and stacked. A tomographic map at period of 10 to 25 s is inverted from the measured group velocities and agrees well with known regional crustal geology. A clear boundary is delineated between the high velocity Tibet plateau and the low velocity Sichuan basin. By measuring the differential travel time for the target period Rayleigh waves recovered from all the station pairs across the occurrence time of the Wenchuan earthquake, consistent travel time variations are observed in the study area. The tomographic inversion clearly shows a region with a ~0.4% velocity decrease. The strike and length of this velocity decrease area strikingly matches the fault zone of the Wenchuan earthquake at depth. We speculate that the observed sharp velocity decrease is the result of decreased stress in the upper crust due to the Wenchuan earthquake. Our results demonstrate the capability of using continuous seismic noise record to monitor the temporal variation of stress field at seismogenic depth.

4.2 Introduction

Time-lapse seismic imaging (4D) is a new and rapidly-evolving technology. It has attracted wide attention in recent years, because accurate imaging of the evolving subsurface structure has significant applications in resource exploration and environmental monitoring. General approaches of time dependent monitoring include measuring changes in the travel time of direct *P* and *S* waves, or detecting changes in the coda waves (e.g., coda wave interferometry). Changes in the recorded seismic waveform could be caused by changes in source or media properties. In order to separate uncertainties caused by slight changes of source location or mechanism, both direct body wave arrivals and scattered coda waves approaches require a highly repeatable source over time. Repeating earthquakes or repeated active shots became the only widely used sources in 4D studies.

By measuring the arrival time of the *S* and *S*-coda waves of repeating earthquakes around the fault area, coseismic velocity decrease associated with large earthquakes have been reported [*Schaff and Beroza*, 2004; *Rubinstein and Beroza*, 2004a, 2004b, 2005, 2007; *Peng and Ben-Zion*, 2006]. Authors suggest strong-motion-induced damage at very shallow depth, usually on the order of hundreds of meters, is responsible for the observed coseismic velocity drop. By detecting consistent temporal variations in the *S*-coda wave of several repeating earthquake clusters, *Niu et al.* [2003] reported an observation of an aseismic transient at seismogenic depth at the San Andreas Fault. However, due to the nature of repeating earthquakes, the temporal and spatial coverage is the biggest holdback in practice. Repeated active source experiments have been applied to expend the dataset beyond using repeating earthquakes. Studies of fault zone guide waves and *S*-coda waves

from repeated chemical explosions at the San Andreas Fault reveals a significant coseismic velocity drop within a ~200 m fault damage zone and a logarithmic time post-seismic velocity healing [*Li et al.*, 1998; *Vidale and Li*, 2003; *Li et al.*, 2006]. They suggest the cause of the velocity changes is from dynamic rupture of the fault zone. *Niu et al.* [2008] observed clear pre-seismic velocity changes from their cross-well active source monitoring experiment at the Parkfield SAFOD drill site. Two large excursions in the travel time of the *S* and *S*-coda waves preceding two nearby earthquakes gives a promising result in earthquake forecasting study. They interpret that pre-rupture stress induced changes in crack properties, such as dilatancy observed in laboratory studies [*Scholz*, 1968], could be responsible for the observed changes in travel time. However, the major disadvantage of using repeated active shots are the poor depth sampling and expensive cost. Explosive energy usually cannot reach deep into the crust where we are most interested.

It has been recently shown that the cross-correlation of the diffuse wave fields (e.g., scattered coda waves or ambient noise) will yield the Green's function between two receivers, as if one of the receivers behaves like an impulsive source [*Weaver and Lobkis*, 2001]. Surface waves traveling between station pairs were firstly recovered by *Campillo and Paul* [2003] from cross-correlation of coda waves of large earthquakes and by *Shapiro and Campillo* [2004] from cross-correlation of seismic ambient noise. From then, surface wave tomography based on the surface waves reconstructed from the seismic noise rapidly emerges as a powerful method for producing high resolution images of the crust and upper mantle at regional and local scales [*Shapiro et al.*, 2005; *Yao et al.*, 2006; *Yang et al.*, 2007]. The discovery of those buried waves in seismic ambient noise wave

field provides a unique temporal coverage in structure properties monitoring, since years long continuous noise records can be used to recover repeated sampling waveforms between station pairs as if one of the stations is a repeating source.

Sens-Schönfelder and Wegler [2006] reported a successful experiment by combining noise cross-correlation with coda wave interferometry to study the changes of medium properties. They observed a clearly seasonal varying velocity (0.1%) with a daily temporal resolution in the coda wave of the recovered Green's function between two stations, at the Merapi volcano, Indonesia. Precipitation induced ground water level variation is used to interpret the observed seasonal velocity perturbations. Similar approaches have been used by *Brenguier et al.* [2008a] at Piton de la Fournaise volcano on La Réunion island. They reported 0.05% seismic velocity drop as precursors for volcanic eruptions. They interpret the decreases in seismic velocity a few weeks before the volcano eruptions as being caused by inflation of the volcano edifice, which is the result of increased magma pressure. As an extension of this study, *Brenguier et al.* [2008b] observed nearly 0.1% coseismic velocity drop followed by clearly postseismic fault healing associated with the 2003 San Simeon and 2004 Parkfield earthquakes along the San Andreas Fault at Parkfield. The observed seismic velocity changes suggest near surface fault damage resulting from strong ground shaking and coseismic/postseismic stress change at depth.

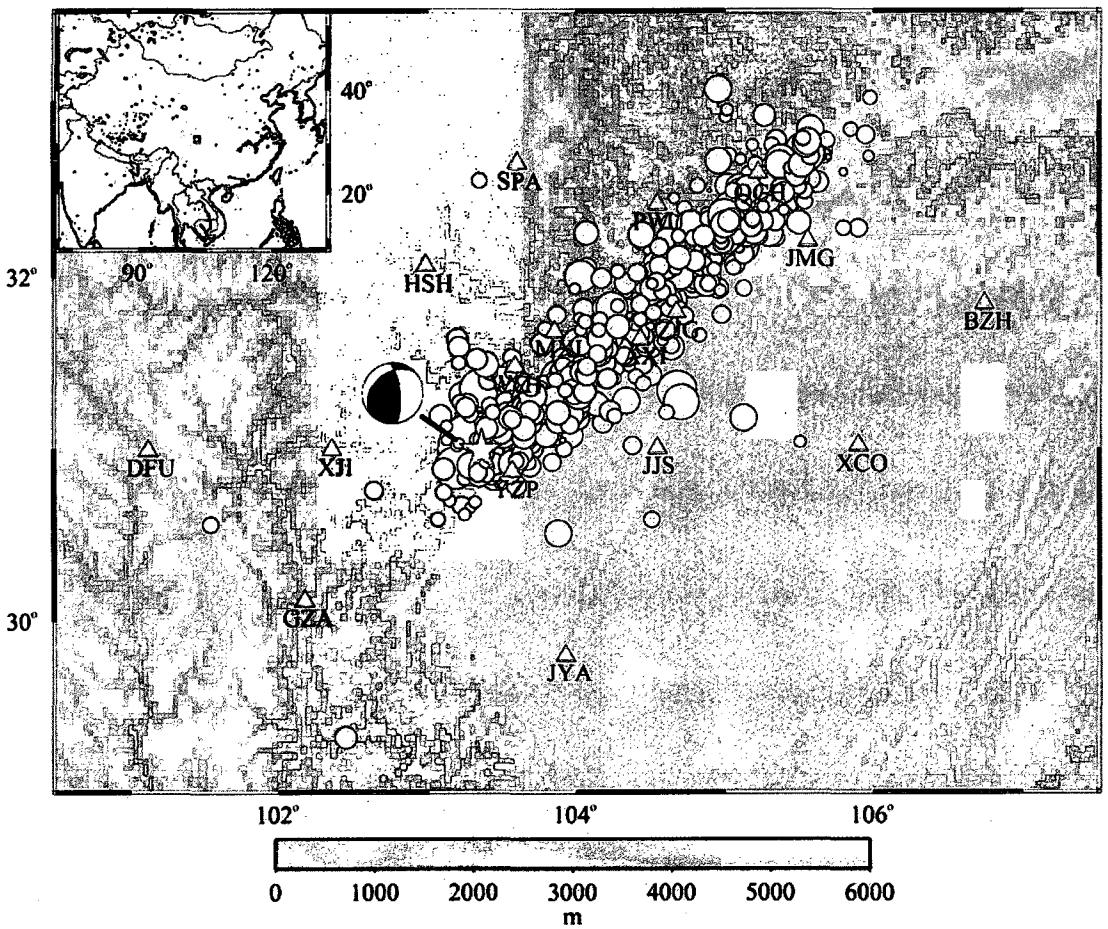

Figure 4.1 Geographic location of the 2008 *M* 7.9 Wenchuan Earthquake and map of the study area. The epicenter of the Wenchuan earthquake is marked with a red star. Also shown is the moment tensor solution of the main shock. Aftershocks ($M > 3$) occur within one and half month after the main shock is marked with white circle and superimposed on the topography map. The size of the circle is scaled to the size of the earthquake. Green triangles are the 16 broadband stations used in this study (station WCH was damaged during the earthquake, which is not used.). Notice the epicenters of the aftershocks are clearly confined along the boundary between the Tibet plateau at Northwest and the Sichuan basin at southeast.

In this study, instead of using the high frequency coda wave [e.g., 0.1 ~ 0.9 Hz in *Brenguier et al.*, 2008a, 2008b], we explore the usage of low frequency (0.04 ~ 0.1) Rayleigh wave to study the time varying velocity structure along the fault zone of the 2008 Wenchuan earthquake (Figure 4.1). Our analysis is divided in three major steps. First, we extract the daily Green's function from continuous seismic records and stack them for each station pair in two groups, before and after the 2008 Wenchuan earthquake. Then, we measure the time delay for the Rayleigh waves propagating through the same two station path across the time of the occurrence of the 2008 Wenchuan earthquake. Finally, we invert velocity change measured from all station pairs to space.

4.3 Data and the Green's Function Extraction

We have collected 100 days (50 days before and after the 2008 Wenchuan earthquake) of continuous vertical component seismic data recorded from the 17 broad band stations run by the Chinese National Seismic Network (CNSN). We first cut the continuous seismic records to daily based segments and then decimate them from 100 samples per seconds to 20 samples per second. Since all of the stations used in this study are the same type of equipment, no station response needs to be removed. In the frequency domain, we apply a spectral whitening by setting the amplitude to one bit for frequency band between 0.02 to 1.0 Hz and zero elsewhere but keeping the phase unchanged. The purpose of spectral whitening is aimed at enhancing the signal from ambient noise by removing persistent monochromatic sources such as the 26 s peak arisen from the Gulf of Guinea [*Shapiro et al.*, 2006; *Bensen et al.*, 2007]. We then correlate these daily seismograms for every possible station pair. The daily cross-correlation is performed using a running time

window with 4096 points time window length and 1024 points running step size, and stacked. Within each running time window, the seismogram is first demeaned and detrended before cross correlation. Finally, a second order band pass Butterworth filter is used to filter those daily cross-correlation measurements between 10 to 25 s to maximize energy recovery.

The resulting cross-correlation functions contain surface wave energy traveling in the opposite directions along the path linking the two stations. The causal and acausal parts are usually asymmetric due to non-uniform distribution of noise source, although the two waves sample the same structure between the two stations. In order to enhance the *SNR* for our target phase, we take the following data processing procedure for each station pair.

First, *SNR* is calculated both for the causal and acausal part of the daily cross-correlation function. We make sure all daily cross-correlation functions have a large *SNR* at its causal part by reverse the cross-correlation functions with a large *SNR* at acausal part. Second, a raw reference Green's function is stacked over all resulting daily cross-correlation functions that passed the first step. The arrival time of maximum energy (T_{max}) is measured at the causal part of the Green's function within the time window by assuming a group velocity within 2.0 to 4.0 km/s. Cross-correlation measurements are then performed between all daily cross-correlation functions and the raw reference Green's function using a 25 s time window around T_{max}. The daily cross-correlation functions with a resulting cross-correlation coefficient less than 0.8 are removed from further analysis. The step is designed to remove bad daily cross-correlation functions before the final stack. Finally, the remaining daily cross-correlation functions are stacked again to yield the final Green's function between each station pair.

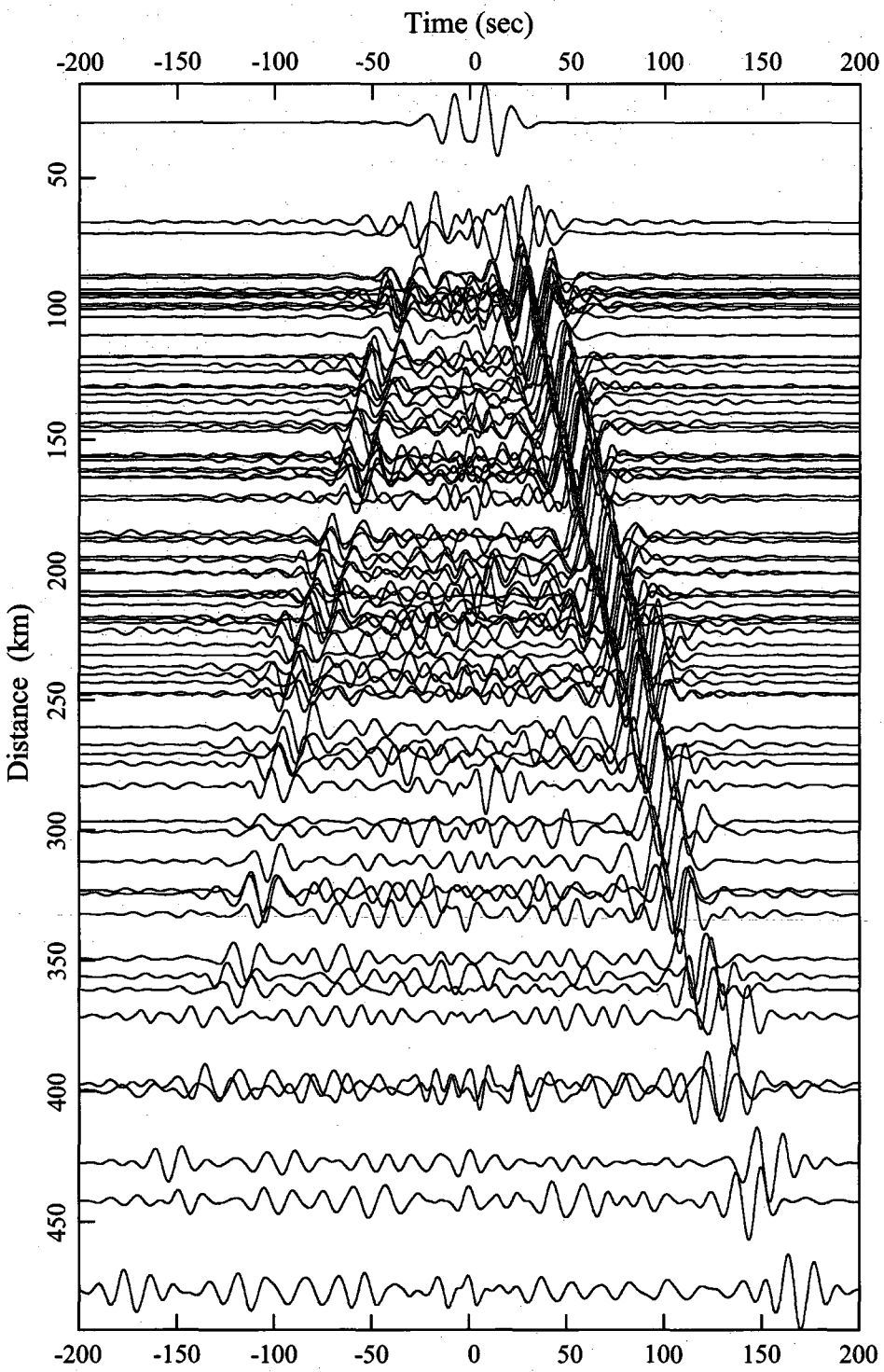

Figure 4.2 Example of 10-25 s Rayleigh wave obtained from seismic ambient noise cross-correlation sorted by inter-station distance. Moveout with increasing station to station distance can be cleanly seen.

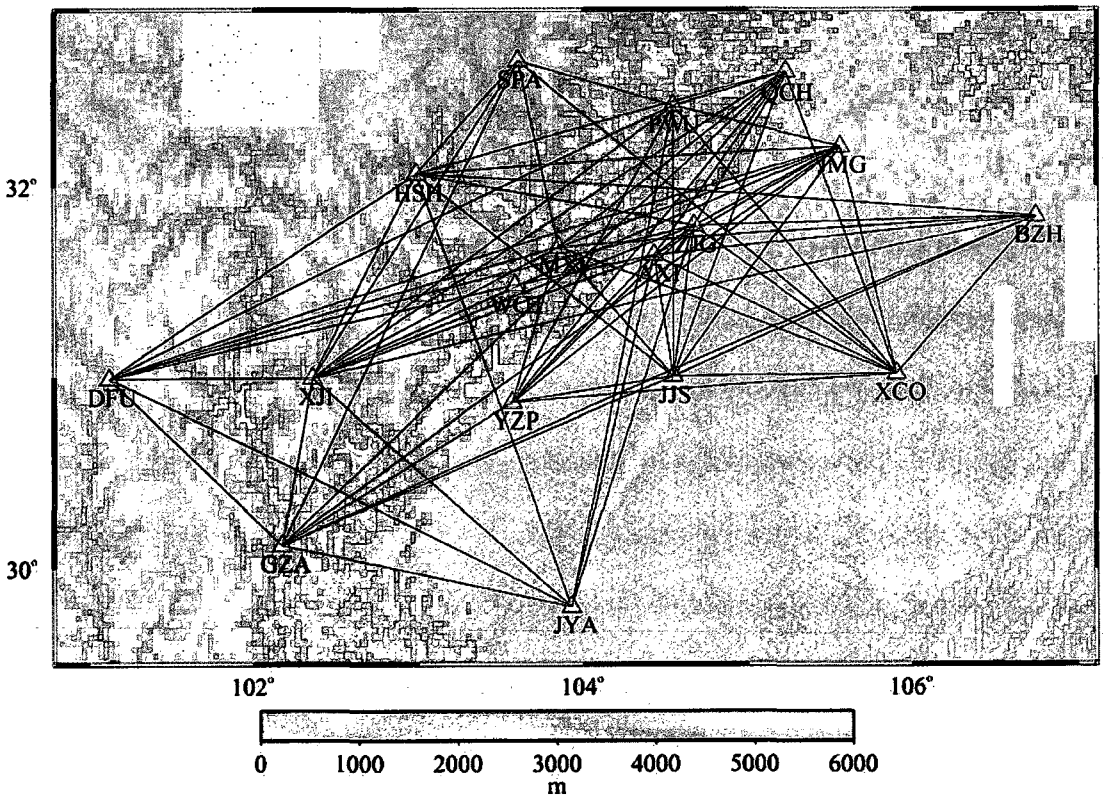

Figure 4.3 Ray path coverage of the data used to obtain the measurements of velocity variations.

Also, two additional separate stacks are taken for 50 days before and after the Wenchuan earthquake. Figure 4.2 shows the 77 reliable measurements of 10 – 25 s Rayleigh wave recovered from the seismic ambient noise. Ray path coverage of the data used in this study is shown in Figure 4.3. The details of data selection are described in following section.

4.4 Results and Discussion

After all the Green's functions are prepared for each station pair, the travel times for the Rayleigh wave along each inter-station path are measured both at the causal (T^{+}_{max}) and acausal (T^{-}_{max}) part of the final Green's function by identifying the arrival time of maximum energy within the time window assuming a group velocity within 2.0 to 4.0 km/s. In theory, homogenous distributed random sources will result in the same absolute value of $\left|T^{+}_{max}\right|$ and $\left|T^{-}_{max}\right|$. However, this is not usually in practical. Uneven distribution of coastal line, which is the major source of seismic ambient noise, produces an asymmetric characteristic of the Green's function result from seismic ambient noise cross-correlation. Timing shift due to station clock error will also resulting in shifting the recovered Green's function. If we define $sumT = T^{+}_{max} + T^{-}_{max}$, Figure 4.4a shows the histogram of the distribution of *sumT* measurements. A good data quality should yield a Gaussian distribution of *sumT* with mean at zero. We have successfully obtained 77 out of 120 pairs of the Green's function with |*sumT*| within 1 second. Outliers are usually due to small *SNR* of the target phase at the acausal part of the Green's function, which will yield a mistaken T^{-}_{max} in the searching for the maximum energy.

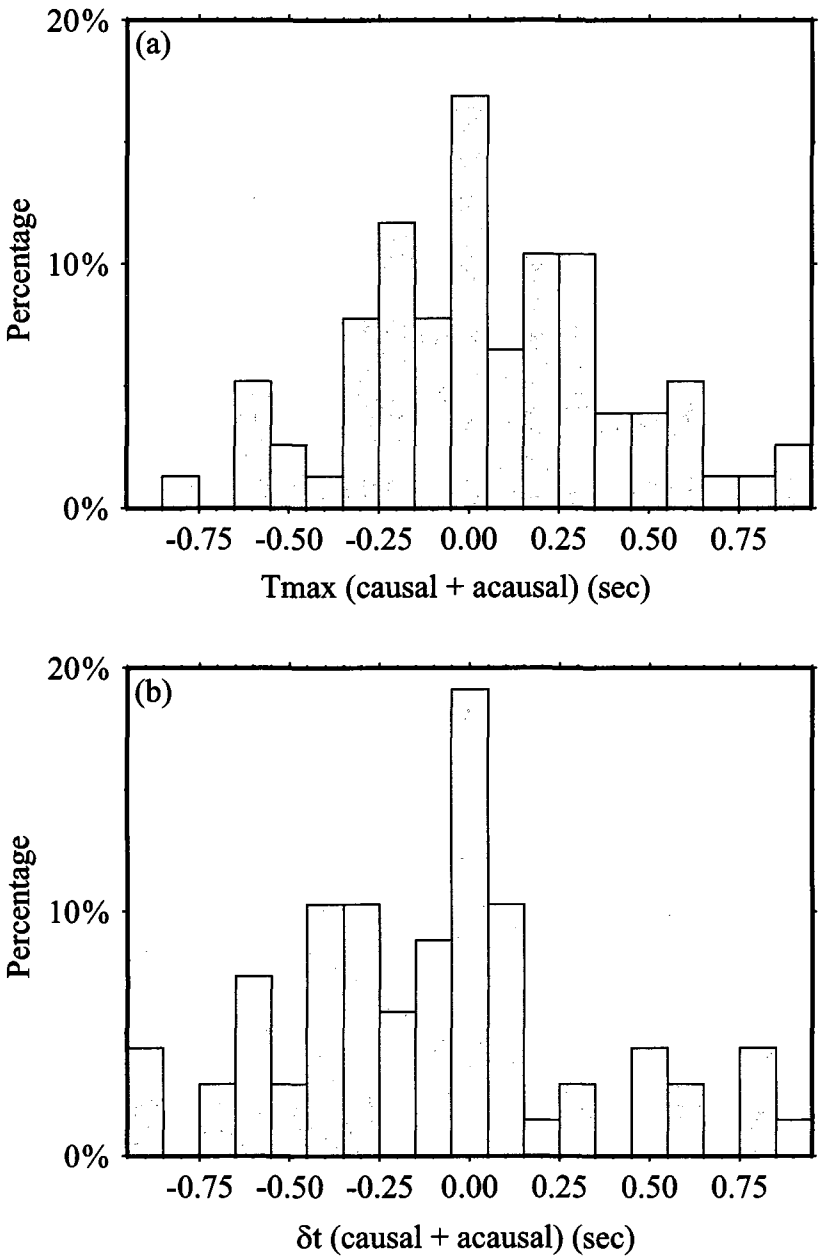

Figure 4.4 Histogram of the *sumT* (a) and *sumδt* (b) measurements. The surface wave arrival time (T_{max}) for a pair of stations should be identical on the causal and acausal correlation time, which will yield a zero mean Gaussian distribution of *sumT*. A velocity change between a pair of stations will result in the same lag time (δt_{max}) on both the causal and acausal correlation time, which will also yield a zero mean Gaussian distribution of *sumδt*.

We believe small *sumT* value (e.g., $|sumT| < 1$ s) guaranteed robust measurement for the Green's function. Station pairs with *sumT* greater than 1 s are removed in further analysis. Since the large *SNR* of the causal part of our recovered Green's function, we use the measurements of T^{+}_{max} and inter-station distances to perform a tomographic inversion for 10 – 25 s Rayleigh wave. The result group velocity maps shows in Figure 4.6a. The map shows close correlation with regional geological features and tectonics. The Sichuan basin is featured with pronounced low velocity due to a thick sediment layer at shallow crust. A clear boundary separates the high velocity Tibet plateau at northwest with the low velocity Sichuan basin at southeast.

The occurrence of 2008 *M* 7.9 Wenchuan earthquake broke a fault zone about 200 km long, and shook the whole source area. We are interested to investigate the extension of the traditional surface wave study to time-lapse monitoring. Using the 25 s time window centered at T^{+}_{max} and T^{-}_{max} respectively, cross-correlation measurements are applied to obtain the lag time between the stacked Green's function before and after the 2008 Wenchuan earthquake. Two examples of the Green's function comparison are shown in Figure 4.5. Apparent time delay is observed in the waveform after the occurrence of the 2008 Wenchuan earthquake. The symmetric delay of both causal and acausal part of the waveform indicates a velocity decrease along the wave path. As shown in *Snieder et al.* [2002], the ratio of time shift to lapse time negatively corresponds the medium's relative velocity changes. We notice a precise measurement of delay time is crucial in the temporal dependent study. By defining $sum\delta t = \delta t^{+}_{max} + \delta t^{-}_{max}$, the distribution of $sum\delta t$ for all 77 pairs used in this study is shown in Figure 4.4b.

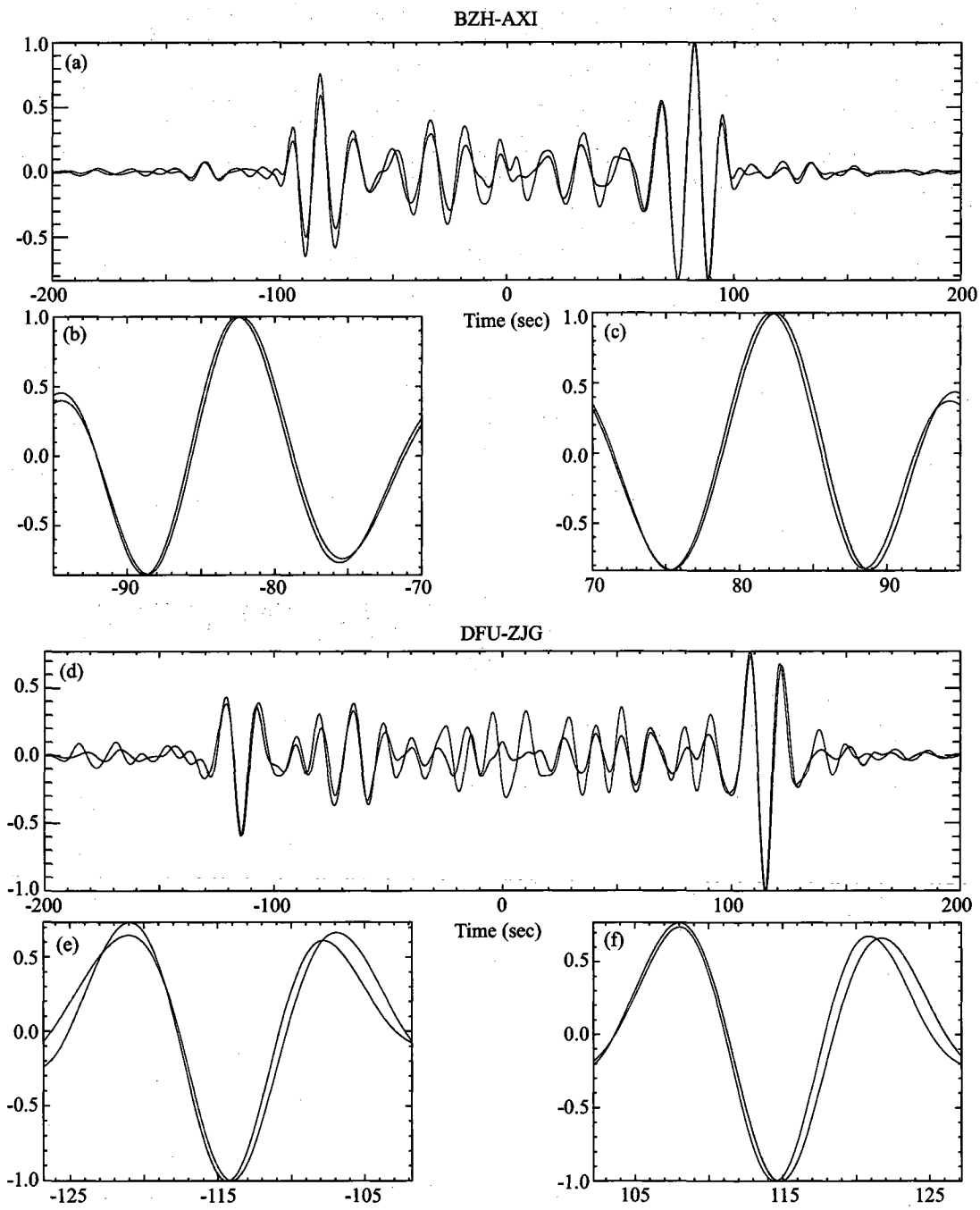

Figure 4.5 Examples of time shift in observed Green's function before and after the occurrence of the 2008 Wenchuan earthquake. Red and blue traces corresponding to the measurements obtained before and after the Wenchuan earthquake, respectively. (b) and (c) are enlarged target time window for (a). (e) and (f) are enlarged target time window for (d). Symmetric delays of post-seismic arrivals are clearly shown in the enlarged time windows.

An average velocity change along the wave path should introduce symmetric time shifting of the waveform, which leads to zero value for $sum\delta t$. As discussed in *Stehly et al.* [2007], a station clock error will result in a one-side time shift of the obtained Green's function. Thus, it will not produce zero value $sum\delta t$. Also, we expect the small time shift due to the change in the spatial distribution of the source will be insignificant by stacking over a long time window (e.g., here we use 50 days of continuous data). The zero mean Gaussian distribution of $sum\delta t$ and large cross-correlation coefficient (> 0.95) indicates the quality of our delay time measurements. As discussed in *Cheng et al.*, [2007], time shift measurements obtained from cross-correlation calculation inversely proportion to the *SNR* of the waveform. Thus, we use the δt^{+}_{max} measured from causal part of the Green's function to calculate the average velocity change along each two station path.

Tomographic inversion shows a sharp velocity decrease of 0.4% at a ~250 km long area parallel to the fault surface trace (Figure 4.6b). The robustness of our observation is discussed in supplementary materials. *Nishimura and Yagi* [2008] reported the Wenchuan earthquake has a fault plane with 33 degree dip. Considering the sampling depth of 10 – 25 s Rayleigh wave is about 15 ~ 20 km, the observed velocity decrease region agrees remarkably well with the projection of the fault in depth. To our knowledge, this is the first direct imaging of fault zone by detecting coseismic velocity drop region associated with a large devastating earthquake from seismic ambient noise study. Similar as the possible explanation proposed by *Nishimura et al.* [2000], the decreases in stress at seismogenic depth within upper crust due to the Wenchuan earthquake could be the reason of the observed velocity decrease.

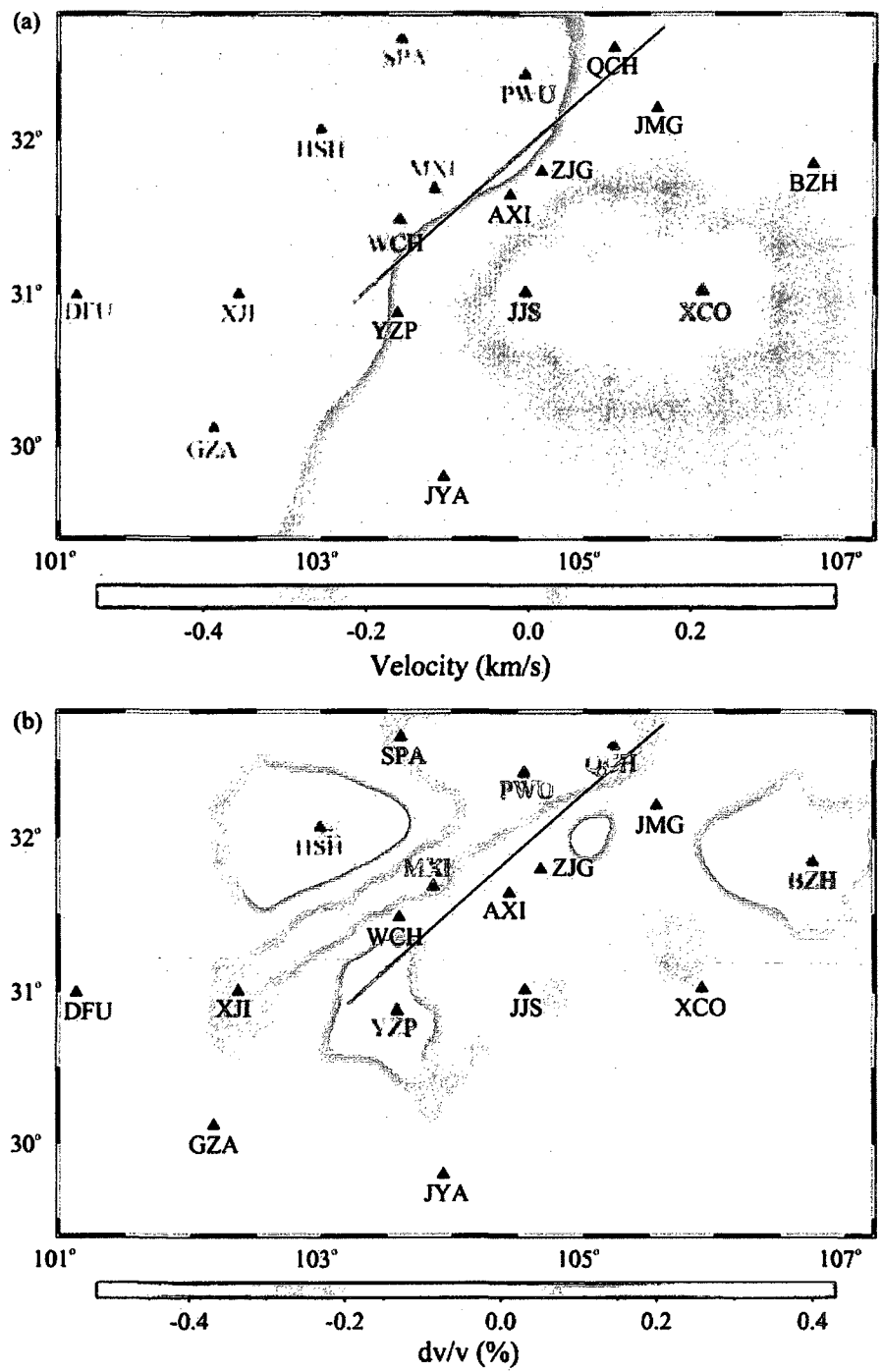

Figure 4.6 (a) Relative group velocity map from 10 to 25 s Rayleigh wave measurements, which is reference to an average group velocity of 2.873 km/s. (b) Coseismic velocity change image obtained from cross-correlation delay time measurements. Black line indicates the surface fault trace of the Wenchuan earthquake. Notice the striking match of the boundary between high and low velocity region with the surface fault trace in (a). Also, the sharp velocities drop in (b).

Due to the limit of data after the May 2008, we do not have enough data to recover a more detailed temporal evolution of crustal stress field around the fault zone area (e.g., post-seismic healing process). Further monitoring of the long term post-seismic fault response will be applied when more up to date data comes in.

4.5 Conclusion

In addition to a 10-25 s group velocity tomographic map recovered from 100 days continuous seismic ambient noise surrounding the area of the 2008 *M* 7.9 Wenchuan earthquake, a new approach combined coda wave interferometry with seismic ambient noise surface wave tomography is developed to investigate the temporal evolution of the velocity field around the fault. A region with a ~0.4% velocity decrease is clearly imaged at depth. We speculate the imaged decrease velocity region results from decreased crustal stress around the fault zone at upper crust. The applications of our method to other active tectonic region such as subduction zones or active volcanoes will provide additional valuable information to study the physical mechanism in depth or even help disaster forecasting.

Acknowledgments. We thank the Chinese National Seismic Network (CNSN) for providing the data.

4.6 Supplementary Materials

Two approaches have been applied to test the robustness of the observed area with sharp velocity decrease. First, a resolution test is applied by using a simple rectangular box with 0.5% velocity decrease to represent the observed area of velocity decrease. Shown in Figure 4.A, with the same ray path coverage used in Figure 4.6, the area of velocity decrease can be clearly recovered.

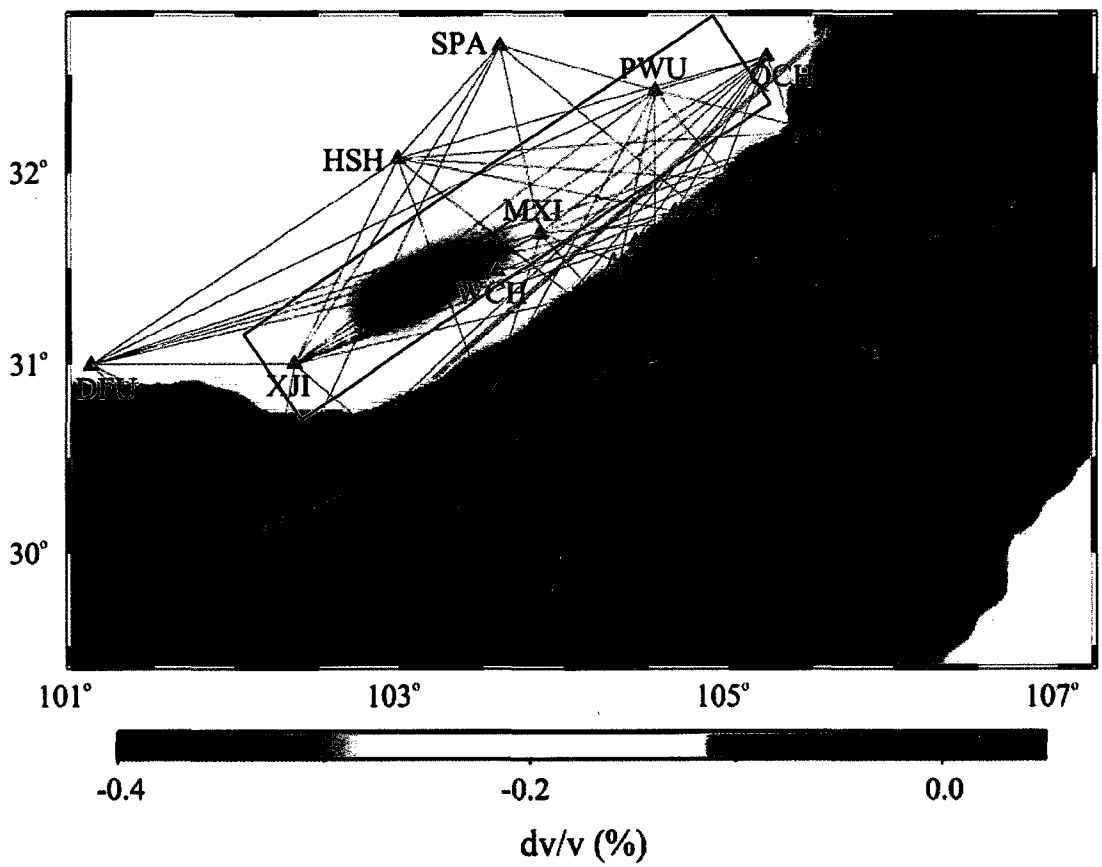

Figure 4.A Synthetic test with a 0.5% velocity decrease within the rectangular box, which corresponds to the observed area with velocity decrease in Figure 4.6b. Also shown are the stations and ray paths used in the test. Purple line indicates the surface fault trace of the Wenchuan earthquake.

In the second test, for each ray path used in this study we have measured the ray path segment length within the observed velocity decrease area (represented as the rectangular box shown in Figure 4.A). Then, we plot the observed delay time along each ray path versus its segment length within the velocity decrease area (Figure 4.B). As you would expect, we observed a clearly increase of the measured delay time with the increased length of ray path segment within the observed velocity decrease area. The results from those two tests suggest that our observation of the area with sharp velocity decrease in Figure 4.6b is quite robust.

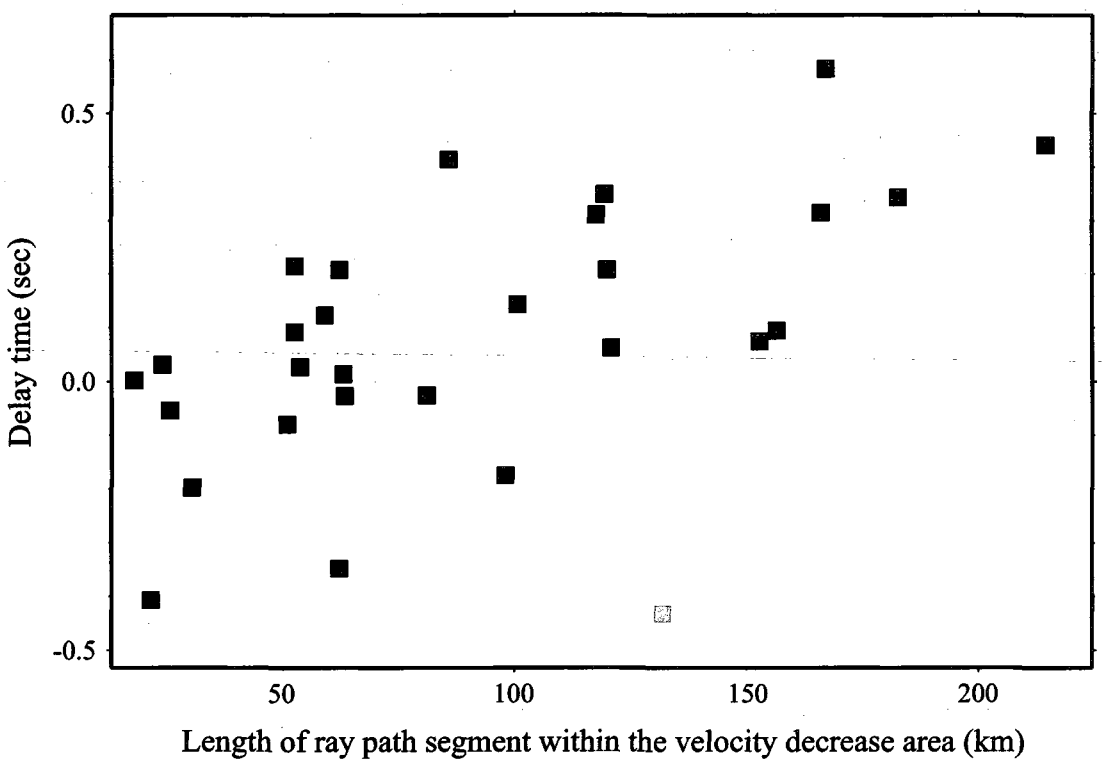

Figure 4.B A clear correlation of the increased delay time with the increased length of ray path segment within the velocity decrease area is shown. Gray square represents the measurement from station pair JYA-HSH. Apparent velocity increase along the ray path outside of the velocity decrease area may responsible for its abnormally behavior.

Appendix A

Spatial clustering and repeating of seismic events observed along the 1976 Tangshan fault, north China

A.1Abstract

Spatial and temporal features of the seismicity occurring along the Tangshan fault in 2001–2006 were investigated with data recorded by the Beijing metropolitan digital Seismic Network. The relocated seismicity with the double difference method clearly exhibits a dextral bend in the middle of the fault. More than 85% of the earthquakes were found in the two clusters forming the northern segment where relatively small coseismic slips were observed during the 1976 M7.8 earthquake. The b values calculated from the seismicity occurring in the northern and southern segment are 1.03 ± 0.02 and 0.85 ± 0.03, respectively. The distinct seismicity and b values are probably the collective effect of the fault geometry and the regional stress field that has an ENE-WSW oriented compression. Using cross-correlation and fine relocation analyses, we also identified a total of 21 doublets and 25 multiplets that make up > 50% of the total seismicity. Most of the sequences are aperiodic with recurrence intervals varying from a few minutes to hundreds of days. Based on a quasi-periodic sequence, we obtained a fault slip rate of ≤ 2.6 mm/yr at ~15 km, which is consistent with surface GPS measurements.

A.2Introduction

The surface of North China is marked by its unusually active tectonic movement and high intraplate seismicity, especially strong and devastated earthquakes. The magnitude 7.8 earthquake that struck the city of Tangshan, ~160 km east of Beijing, on July 28,

1976 is one of the most destructive events in terms of the loss of life. The earthquake occurred on the northern margin of the North China sedimentary basin near the boundary between the basin and Yanshan uplift. The main shock fault is a NE trending strike-slip faulting system [*Shedlock et al.*, 1987; *Nabelek et al.*, 1987] with a dextral bend in the middle that divides the fault into the southern and northern segments (Figure A.1). High seismicity has been maintained since the earthquake along the main fault. To better monitor the seismic activity in the capital area, the Chinese Earthquake Administration (CEA) started to deploy the Beijing metropolitan digital Seismic Network (BSN) in the late 90s. Currently the network consists of 107 broadband, borehole and surface short-period stations that covers an area of ~180,000 km^2 including Beijing, Tianjin and Tangshan metropolitan cities (Figure A.1). Since 2001, a large amount of data including waveform data has been collected. The data provide a new opportunity for investigating the spatial and temporal features of the seismicity along the Tangshan fault.

Fine relocation of seismicity along a fault not only provides a direct 3D view of the fault structure [e.g., *Waldhauser and Ellsworth*, 2002], but also shed lights on earthquake physics [*Rubin et al.*, 1999]. *Gutenberg and Richter* [1944] found that the earthquake size distribution in California follows a power law. The slope of this power law, the '*b*-value', is commonly used to describe the relative occurrence of large and small events. Laboratory studies [e.g., *Scholz*, 1968] found that *b* values are inversely dependent on differential stress. Recent studies [e.g., *Schorlemmer and Wiemer*, 2005] confirmed this dependence from field data.

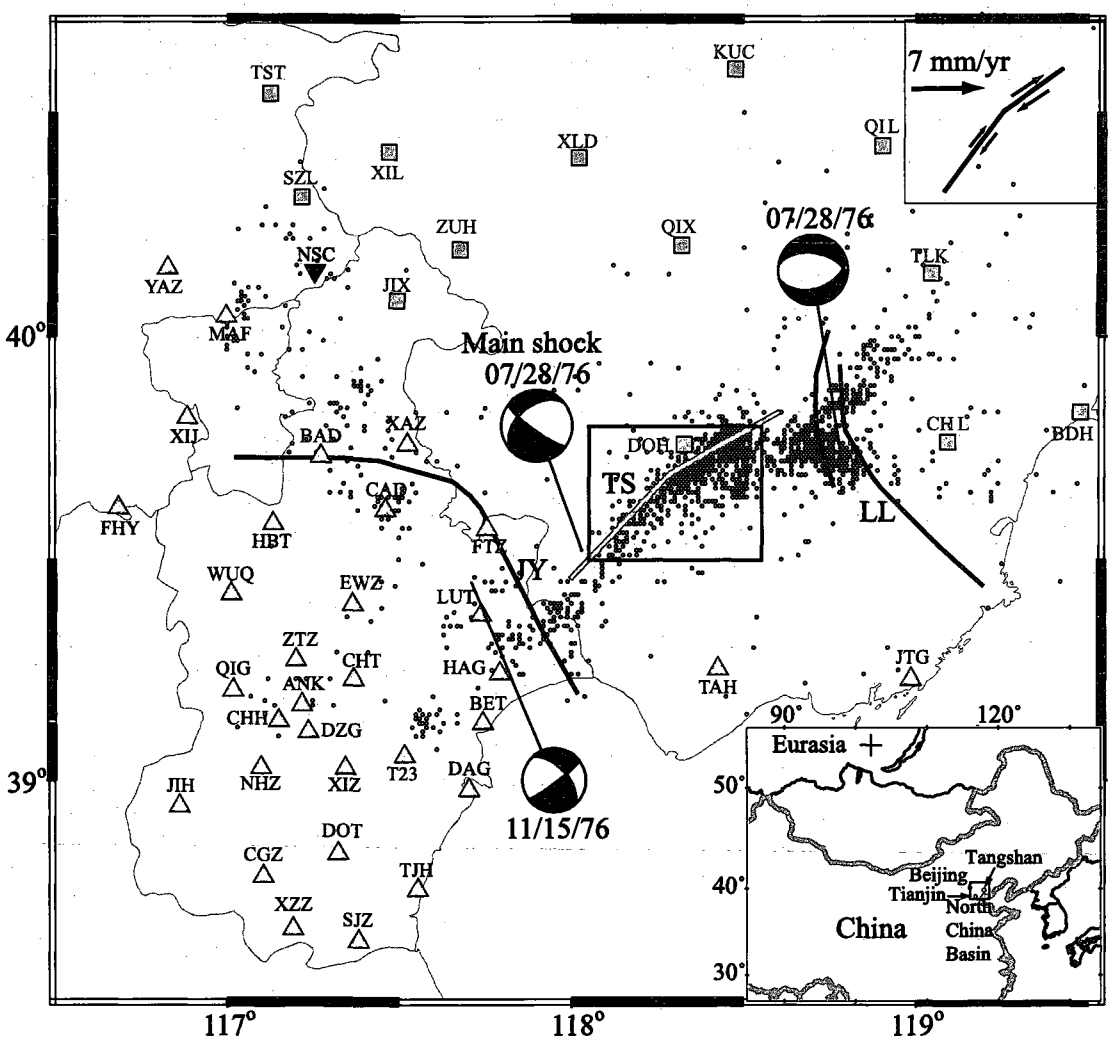

Figure A.1 Geographic map showing the 1976 Tangshan earthquake series, major faults, and BSN stations. Fault locations are from *Shedlock et al.* [1987]. TS, Tangshan main Fault; JY, Jiyunhe Fault; LL, Luanxian-Leting Fault. Squares, triangles, and reverse triangle indicate broadband, borehole, and surface short-period stations, respectively. Circles indicate earthquakes ($0.3 < M_L < 5.0$) occurring between 10/2001 and 12/2006. Only earthquakes inside the box were relocated. Upper inset illustrates the bend of the Tangshan fault with the arrow indicating the eastward motion of the North China basin relative to the stable Eurasia that is indicated by the cross in the lower inset.

Repeating earthquakes are a series of earthquakes regularly occurring on a patch of a fault plane. These earthquakes usually have approximately the same magnitude with roughly the same repeating interval. They are commonly interpreted as repeated ruptures of a single asperity surrounded by a stably sliding area. Repeating earthquakes have been observed in the creeping zones of major faults along plate boundaries [*Vidale et al.*, 1994; *Igarashi et al.*, 2003]. Using teleseismic waveform data, *Schaff and Richards* [2004] found that ~10% of the seismic events in China were repeating earthquakes. *Nadeau and Johnson* [1998] used the scalar moment and recurrence interval of repeating earthquakes to infer fault slip rate at depth.

In this study, we analyzed the catalog, local and regional waveform data of more than 1000 earthquakes occurring between 2001 and 2006 in the aftershock zone of the 1976 Tangshan earthquake to study the spatial distribution, similarity and repeatability of these events. We first relocated earthquakes using the double-difference (DD) algorithm [*Waldhauser and Ellsworth*, 2000] and then applied waveform cross-correlation methods to identify similar and repeating earthquakes.

A.3Data and Analysis

In this study we used the data collected by the BSN between October of 2001 and December of 2006. There are a total of 1020 events ($0.5 \leq M \leq 4.1$) that occurred along the main Tangshan fault (rectangle in Figure A.1) in the period. To avoid waveform complication from the head wave Pn, we selected a total of 46 stations that are located within 150 km from the main fault (Figure A.1). We have 9184 picks of P-wave arrival

times from the BSN bulletins. Among the 1020 events, there are 619 events whose waveform data are available to us.

Catalog locations were routinely determined from picks of P- and S-wave arrival times. Typical precision of location error is in the order of a few kilometers to a couple tens of kilometers. To better resolve the 3D seismicity, we used the DD method to relocate the events. The DD method minimizes residuals between the observed differential times measured from pairs of earthquakes at each station and those calculated times. Instead of locating each event individually the DD method is designed to derive a set of locations that best fit the relative travel times among the entire seismicity. Especially when accurate differential travel-time data are available from waveform cross correlation (cc), the DD method has been proved to be able to collapse diffuse catalog locations into sharp images of seismicity [*e.g., Waldhauser and Ellsworth*, 2002].

In addition to the bulletin picks, we also used a cc based method to measure accurate differential times between pairs of events. To do this, a 1-10 Hz bandpass filter was first applied to the data. As the sampling rate of the BSN stations is 50 Hz, an interpolation was applied before the differential time measurement. The data are interpolated to a sampling interval of 0.3125 ms, which can be considered as the precision of our differential time measurements. The cc is calculated in the time domain using a 1.1 s time window (0.1 s and 1.0 s before and after the onset of the P wave, respectively). To ensure the time window is correctly selected, we manually picked 6089 P wave arrival times for all the available waveform data that have high signal to noise ratio. We selected 83831 pairs with a cc >0.7 for the DD relocation.

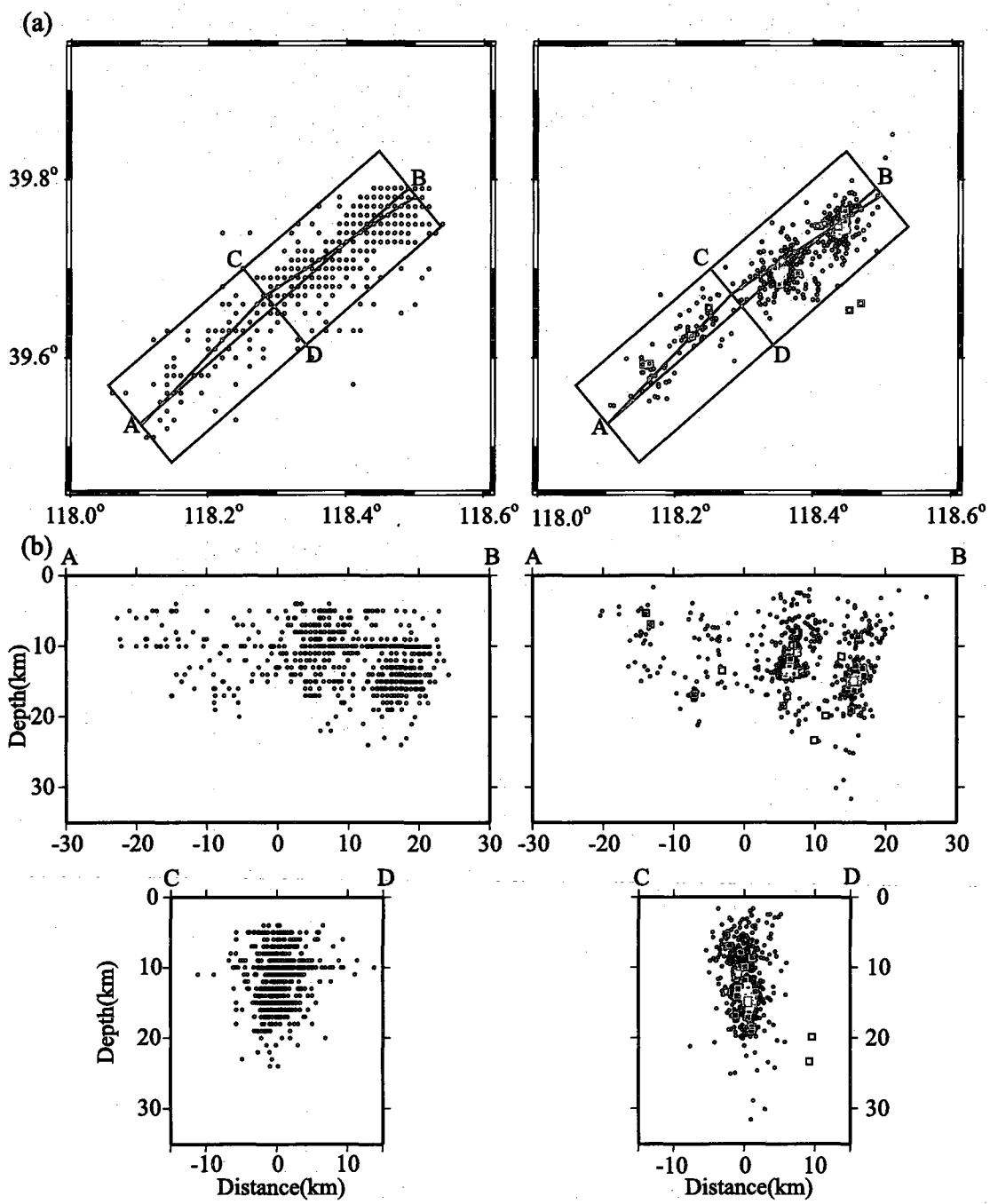

Figure A.2 A comparison of BSN catalog locations (left) and DD locations (right) of the seismicity. (a) Map view of seismicity. (b) Depth cross section views of the seismicity. Similar and repeating events are shown in open squares. The three sequences discussed in the text are shown by solid squares. The large lateral scatter in the relocated seismicity reflects either the nature of the seismicity in this intraplate fault or large location errors due to the station coverage.

A.4Results and Discussion

The relocated seismicity reveals a narrow fault zone at most locations along the Tangshan fault (Figure A.2). Most of the events occurred within a depth range of ~5-20 km and they define a nearly vertical fault. Geographically, more than 85% of the seismicity is distributed in the northern segment, where the relocated earthquakes form two tight clusters. The northern segment had very small coseismic slips during the 1976 M 7.8 Tangshan earthquake, suggesting that most of the strain energy in this segment was released with relatively small seismic events. Seismicity in the southern segment is lower and remains diffuse even after relocation. There is also a significant difference in *b* value of the seismicity between the two sections (Figure A.3a). The *b* values calculated from the northern and southern section are 1.03±0.02 and 0.85±0.03, respectively. The relative lower seismicity and lower *b* value observed from the southern section can be qualitatively explained by the ENE-WSW oriented compressional stress field resulting from the India-Eurasia collision. Due to this eastward compression, the southern segment experiences a lower shear stress but a higher normal stress compared to the northern segment, resulting a smaller number of earthquakes with relatively larger magnitude that explains the observed lower seismicity and *b* value.

We noticed that many events have similar waveforms during the cc calculation (Figure A.3b). If we define similar events to be event clusters having cc $\geq$ 0.8 for a time window 1s before the P wave to 5s after S wave recorded at least one station, we identified a total of 46 similar event sequences with the number of events per sequence ranging from 2 to 130. These comprised 21 doublet and 25 multiplets.

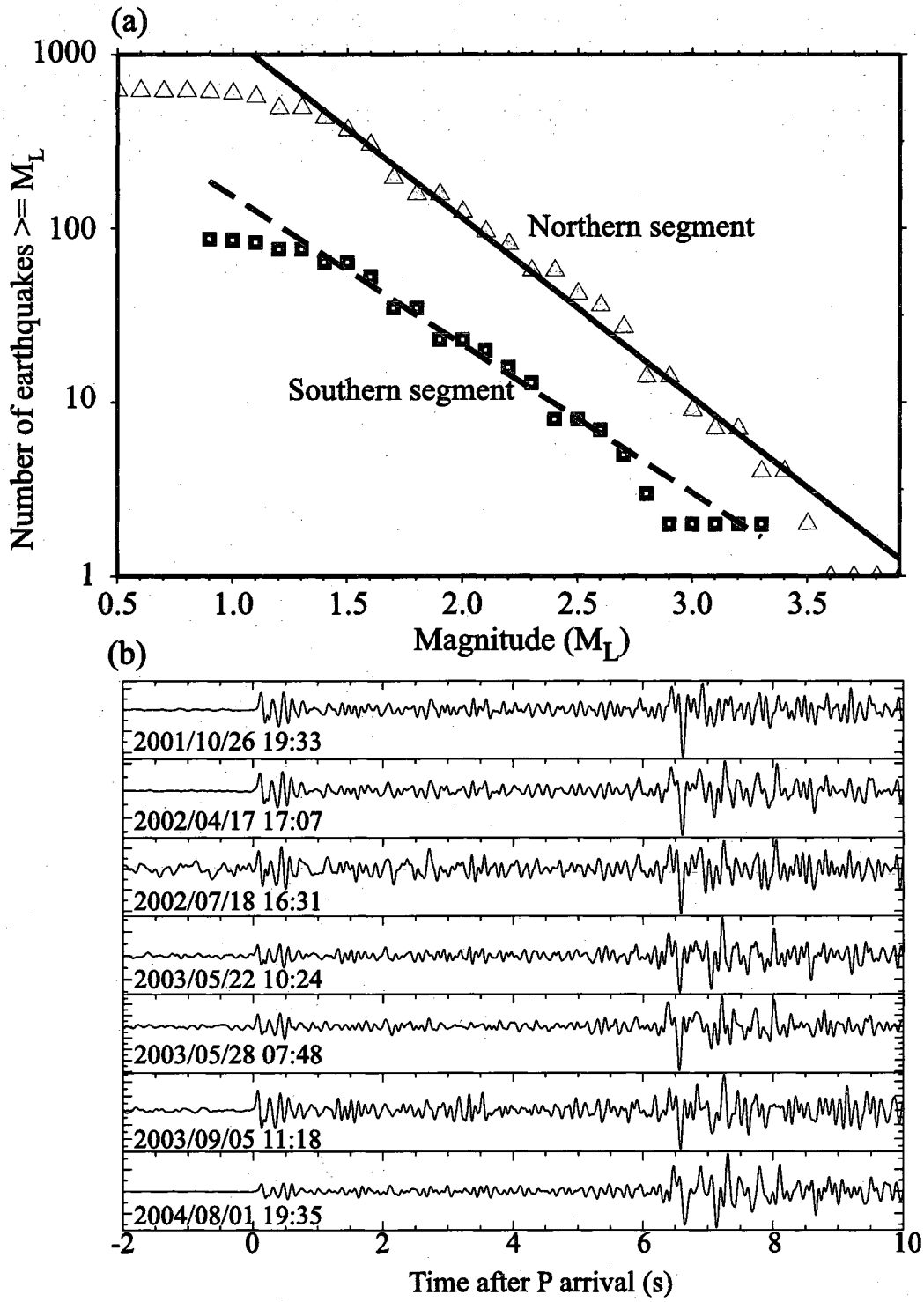

Figure A.3 (a) Cumulative frequency-magnitude distributions for the northern (solid triangles) and southern segment (open squares). An increment of 0.1 in magnitude is used to calculate the cumulative event numbers. (b) Examples of seismograms of sequence 1 recorded at the broadband station QIX station.

The total number of earthquakes in the 46 sequences is 328, making up to 53% of the entire seismicity (619 events). We found significant variations in the recurrence time interval in each sequence, ranging from a few minutes to hundreds of days. Event magnitude in each sequence also varies substantially. 12 doublets and 3 multiplets have recurrence interval less than 10 days. Another 3 doublets and 3 multiplets occurred within a two-month period.

Besides the repeating events, some immediate aftershocks have also been observed to exhibit very similar waveforms [*e.g., Cheng et al.*, 2007]. The difference between repeating events and similar aftershocks is defined by their spatial distribution. In principle rupture areas of the repeating events overlap with each other, while those of the similar aftershocks are displaced from one to another. It is likely that the identified sequences include both repeating events and similar aftershocks, resulting in aperiodicity in recurrence interval and large variations in event size in each sequence. Fine relocation of these sequences is thus needed to separate the repeating events from the similar ones.

Most of the BSN stations are located in the northwest side of the fault, resulting in a one-side distribution to the Tangshan earthquakes. Because of the underlying thick sedimentary layer, the BSN stations usually have high noise levels. The one-side station coverage coupled with low signal to noise ratio makes it difficult to determine the accurate locations of the earthquakes. They also affect the task of defining a complete list of events in each sequence, making them appear to be aperiodic.

We applied the following criteria to select multiplets to perform a fine relocation: (1) average cc > 0.85; (2) internal inconsistence in travel time picking < 0.5 ms; (3) average recurrence interval > 100 days; (4) number of travel time picking > 4(N-1), where N is

the event number of the multiplet and 4(N-1) is the number of unknowns. Only 3 multiplets satisfied these four requirements. Details of the three sequences are listed in the supplementary table. For each sequence, we applied the fine relocation method [*Got et al.*, 1994] to the differential travel-time data. We also assume that all the events occurred in the vertical fault plane that derived from a linear regression of the relocated seismicity. The relocation error is in the order of tens meters based on a grid search method assuming a travel time picking uncertainty of 0.5 ms.

To compare distances between similar events with rupture sizes and to calculate fault slip rate, it is necessary to have an objective measurement of earthquake size. Magnitude in the BSN catalog is given in Richter scale. This is done by convolving digital recordings with the instrumental response of the Wood-Anderson seismograph and correcting the local attenuation structure. We first used spectral ratio method [*Vidale et al.*, 1994] to verify how well event magnitude in the catalog was determined. To do this, seismograms of all events in a multiplet were first assembled at a given station. Amplitude spectra were then calculated from a 20s time window that includes both P and S waves. These spectra were further stacked to form a station average, which was used to normalize the individual spectrum. The normalized spectra, the spectral ratios, were computed for every station and event. The spectral ratios were reassembled on event base and were subsequently averaged to form an event spectra ratio. The relative moments are finally measured from the spectral ratio averaged in the frequency range of 1 to 10 Hz. There is an excellent linear correlation between the logarithm of relative moments and M_L (Figure A.4a), indicating that relative magnitude in the BSN catalog is well determined (Figure A.4a).

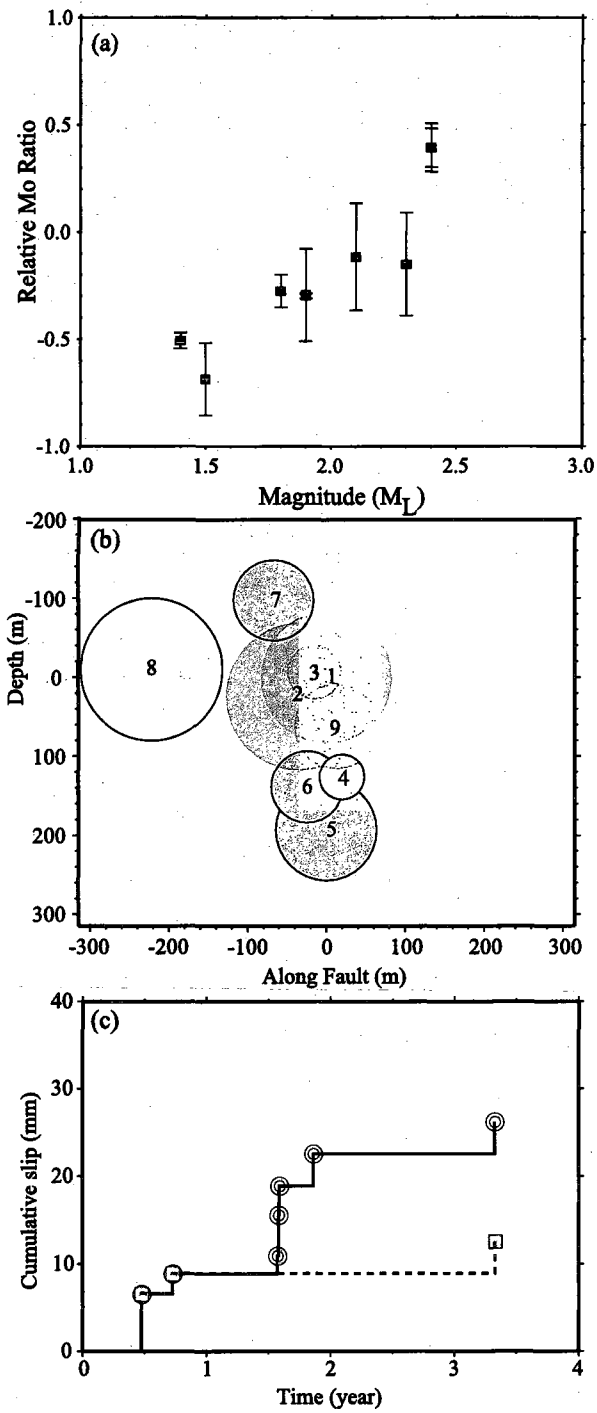

Figure A.4 (a) Relative moment ratios calculated from the spectral ratios are shown as a function of local magnitude. Notice the good linear correlation between the two. (b) Depth cross section along the fault plane of the relative locations of the 9 earthquakes in sequence 1. (c) Cumulative slips calculated from a loose cluster consisting of 8 events (except 8 in Figure A.4b) and a tight cluster consisting 4 events (1, 2, 3 and 9) are shown in open circles and solid squares, respectively.

We then used the moment-magnitude relationship of *Hanks and Kanamori* [1979],

$$\log(M_0) = 16.1 + 1.5M_L \quad (1)$$

to convert M_L to M_o. We further assume a circular rupture model and estimate rupture radius r, from M_o under a given stress drop ($\Delta\sigma$) by using the equation from *Kanamori and Anderson* [1975]:

$$r = \left(\frac{7M_o}{16\Delta\sigma}\right)^{1/3} \quad (2)$$

The coseismic slip is then calculated from the estimated M_o and r:

$$d = M_o / \mu\pi r^2 \quad (3)$$

Figure A.4b shows an example of the distribution of the relocated events in sequence 1. The size of the circle represents the rupture area which was calculated based on equation (2) with a stress drop of 3 MPa. It appears that event 8 lies outside the cluster, and events 4, 5 and 6 are another subgroup. Event 7 also barely overlaps with other events. If we define a loose cluster that includes all the events except for event 8, then we obtained an annual slip rate of 7.1±1.6 mm/yr using a linear regression of the cumulative slip shown as red circles in Fig. 4c. As the 8 events did not occur at the same patch, the released strains should not be solely built up within the recurrence intervals. Thus the annual slip rate here should be considered as an over estimate of the actual stress build up along the fault. If we used the four events (1, 2, 3 and 9) that have better overlaps, we obtained an annual slip rate of 2.6±0.4 mm/yr.

The relocated results for the three sequences are summarized in supplementary table. For sequence 2, only the first and third events overlap with each other. Using these two events, we obtained an annual slip rate of 7.6 mm/yr. Because of the partial overlap, this value should be also considered as an overestimation. For the 3rd sequence, we have very

few observations for three members (marked as x in supplementary table), and there are no statistically significant overlaps among the rest events.

GPS measurement showed that the surface of North China basin is overall moving to the east with respect to the stable Eurasia [*Wang et al.*, 2001]. The geodetic data also revealed significant internal deformations, suggesting that part of the eastward motion is likely devoted to the strain buildup along the Tangshan fault. Our estimate of a slip rate of 2.6 mm/yr thus agrees with the surface GPS measurement. *Cheng et al.* [2007] found no repeating earthquakes along an intraplate fault in central Japan, which they attributed to the lack of a weak zone along the fault. The presence of a large amount of similar and repeating events along the Tangshan fault suggests that damage zone of the 1976 earthquake remains weak since the earthquake. The seismicity is unevenly distributed along the fault, surrounded by weak areas that undergo stable creep under steady tectonic loading.

A.5Conclusions

We have investigated seismicity along the Tangshan fault in 2001-2006. We found that: (1) the seismicity clearly exhibits a dextral bend in the middle of the fault and more than 85% of the events occurred in the northern segment where relatively small coseismic slips were observed during the 1976 M7.8 earthquake; (2) the two segments have significantly different b values, 1.03±0.02 and 0.85±0.03 for the northern and southern sections, respectively; (3) approximately 53% of the earthquakes are similar or repeating events, exhibiting a highly clustering feature of the seismicity in space; (4) the annual slip rate along the northern section of the fault is no larger than 2.6±0.4 at seismogenic depth,

consistent with surface GPS observations. The distinct seismicity and b values are probably the collective effect of the fault geometry and the regional stress field. The high percentage of similar and repeating events suggested that the intraplate Tangshan fault has a well developed weak zone that is characterized by many mature interplate faults.

Acknowledgments. We thank the CEA network center for providing data, and two anonymous reviewers for constructive comments. This study was supported by Ministry of Science and Technology of China under Grant 2005DFA20980, NSF Grant EAR-0352134, and an international travel grant from Rice University.

Appendix B

Preseismic velocity changes observed from active source monitoring at the Parkfield SAFOD drill site

B.1 Abstract

Measuring stress changes within seismically active fault zones has been a long-sought goal of seismology. One approach is to exploit the stress dependence of seismic wave velocity, and we have investigated this in an active source cross-well experiment at the San Andreas Fault Observatory at Depth (SAFOD) drill site. Here we show that stress changes are indeed measurable using this technique. Over a two-month period, we observed an excellent anticorrelation between changes in the time required for a shear wave to travel through the rock along a fixed pathway (a few microseconds) and variations in barometric pressure. We also observed two large excursions in the travel-time data that are coincident with two earthquakes that are among those predicted to produce the largest coseismic stress changes at SAFOD. The two excursions started approximately 10 and 2 hours before the events, respectively, suggesting that they may be related to pre-rupture stress induced changes in crack properties, as observed in early laboratory studies [*Brace et al.*, 1966; *Scholz*, 1968].

B.2 Observation and Discussion

It is well known from laboratory experiments that seismic velocities vary with the level of applied stress [*Birch*, 1960; 1961; *Nur and Simmons*, 1969]. Such dependence is attributed to the opening and closing of microcracks due to changes in the stress normal to the crack surface [*Walsh*, 1965; *Nur*, 1971; *O'Connell and Budiansky*, 1974]. In

principle, this dependence constitutes a stress meter, provided that the induced velocity changes can be measured precisely and continuously. Indeed, there were several attempts in the 1970s to accomplish this goal using either explosive or non-explosive surface sources [*De Fazio et al.*, 1973; *Reasenberg and Aki*, 1974; *Leary et al.*, 1979]. The source repeatability and the precision in travel-time measurement appeared to be the main challenges in making conclusive observations.

With the availability of highly repeatable sources, modern data acquisition systems and advanced computational capability, *Yamamura et al.* [2003] showed compelling evidence that seismic velocity along a baseline in a vault near the coast of Miura Bay, Japan, responds regularly to tidal stress changes. *Silver et al.* [2007] found an unambiguous dependence of seismic velocity on barometric pressure from a series of cross-well experiments at two test sites in California. The stress sensitivity depends primarily on crack density and has a strong nonlinear dependence on confining pressure. Consequently, crack density is expected to decrease rapidly with depth, as should stress sensitivity. It is thus unclear whether the stress-induced velocity variations observed at shallow depths [*Yamamura et al.*, 2003; *Silver et al.*, 2007] are still detectable at seismogenic depth.

To explore stress sensitivity at seismogenic depth, we have conducted an experiment at Parkfield, California, where adjacent deep wells, namely the SAFOD pilot and main holes (Figure B.1), are available. Accurately located seismicity, together with the availability of high quality geophysical data in the Parkfield region, make it one of the best areas to detect temporal changes related to the earthquake cycle.

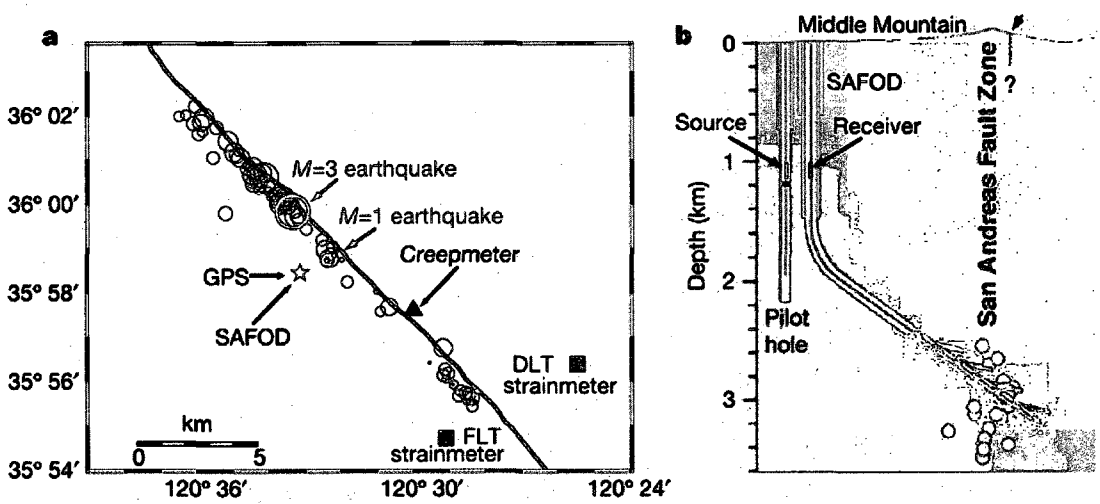

Figure B.1 Map of the experiment site. a, Circles show earthquakes that occurred during the experiment period. The $M = 3$ and $M = 1$ events are shown as red and green circles, respectively. Star indicates the Parkfield SAFOD drill site, where the experiment was conducted. Triangle, location of the Middle Mountain creepmeter; squares, locations of the Donalee (DLT) and Frolich (FLT) Gladwin borehole tensor strainmeters. b, A vertical section (schematic) of the SAFOD main and pilot holes. Red vertical lines indicate the source and receiver locations. Background image is electrical resistivity [*Unsworth et al.*, 2000] with blue (red) corresponding to relatively high (low) resistivity. White circles show the seismicity, red dashes indicate the SAFOD instrumentation, and black short lines represent sub-horizontal holes drilled off the main hole. The profile at the top of the panel is the surface topography with the arrow indicating the surface exposure of the fault.

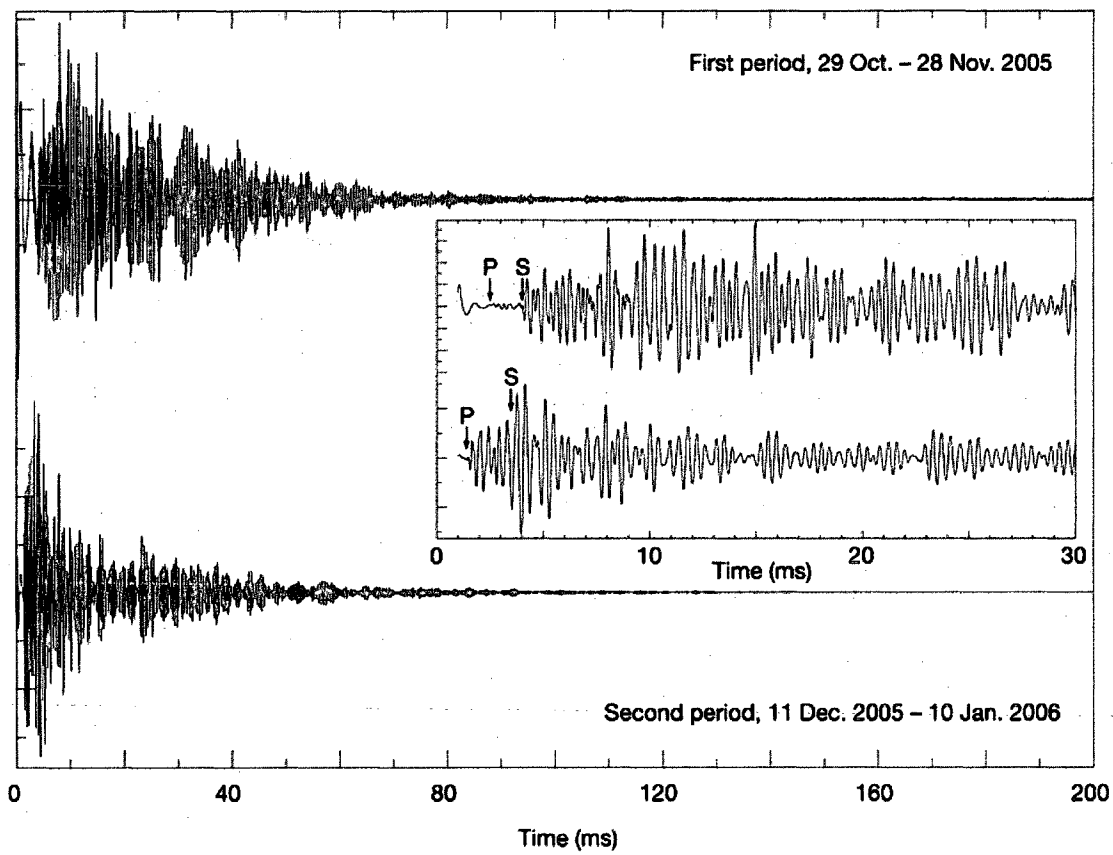

Figure B.2 An example of the raw seismograms obtained from a horizontal component in the two periods. Both are filtered with a band pass filter of 1–5 kHz. Inset shows the first 30 ms of the waveforms. P and S indicate the compressional and shear wave arrivals.

A specially designed 18-element piezoelectric source and a three component accelerometer were deployed inside the pilot and main holes, respectively, at ~1 km depth (see Methods). The experiment was conducted for ~2 months: the first period was 29 October to 28 November 2005, and the second was 11 December 2005 to 10 January 2006. We fired a pulse with a width of 1 ms four times per second and recorded 200-ms-long data with a sampling rate of 48,000 Hz. The waveforms were automatically stacked in groups of 100 shots, resulting in one record (Figure B.2) acquired every 27 s (two additional seconds were needed in storing the data).

To enhance the signal-to-noise ratio (SNR) of the data, we further stacked the raw seismograms in sets of 100. This stacking procedure reduced the data to one stack every 45 min. The 45-min stacked records were then processed with a bandpass filter of 1–5 kHz before the travel-time analysis. We used a cross-correlation-based method to estimate the delay time, which permits subsample precision (see Methods). No smoothing or filtering was applied to the measured delay time series. The error in delay time measurement was estimated to be ~ 1.1×10^{-7} s, based on SNR analysis (see Methods), and this estimate was confirmed by comparing measurements from consecutive recordings. As the nominal travel time of the shear-wave (S-wave) coda along the baseline is about 10 ms, the detectable threshold of velocity perturbation is ~ 1.1×10^{-5}, or 11 p.p.m.

We measured the delay times of the S wave and the S wave plus its coda up to 20 ms with respect to a fixed reference trace for each period (Figure B.3). The measurements show daily cycles that are well correlated with the temperature record (Figure B.3).

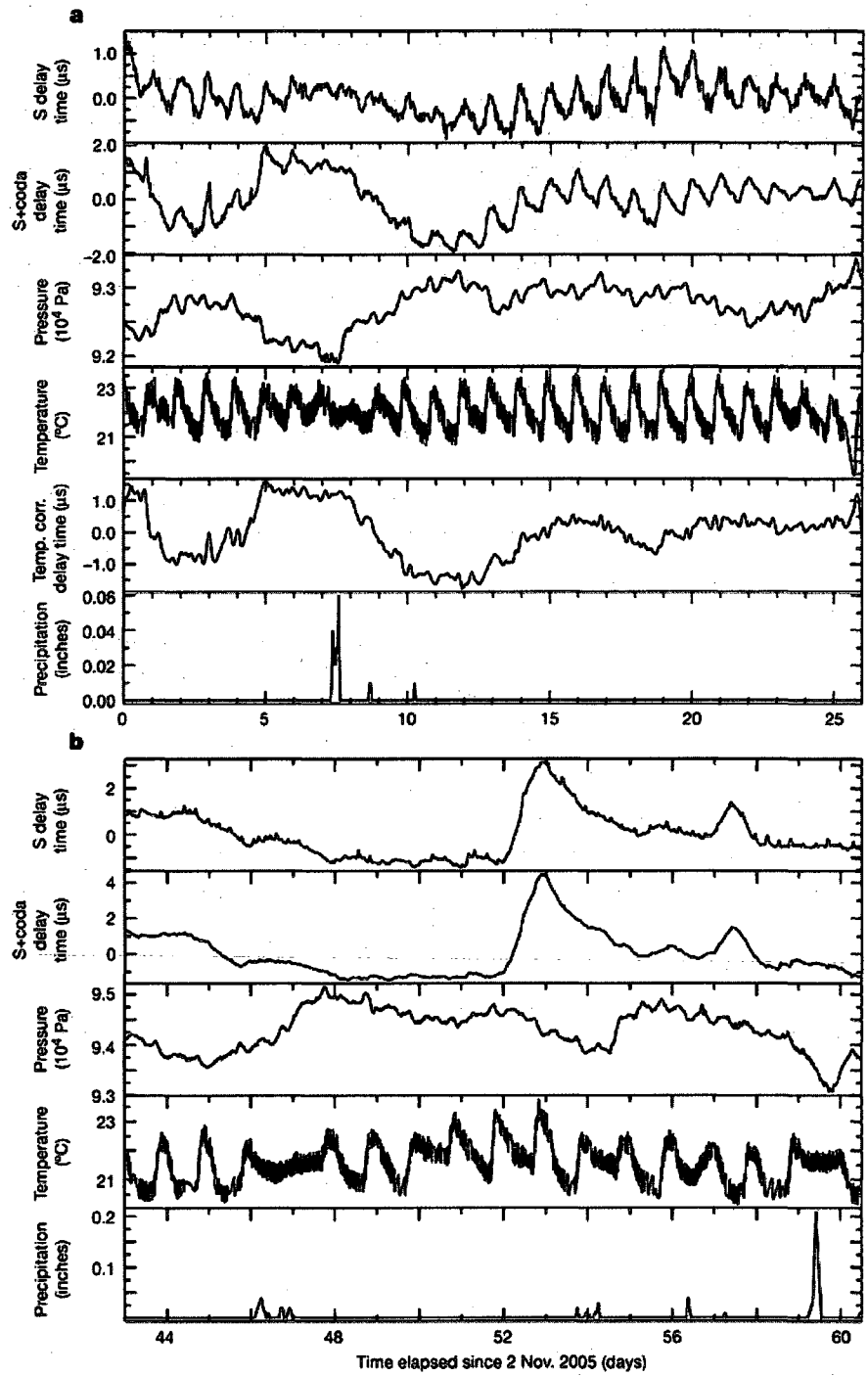

Figure B.3 Estimated delay times for the two periods. a, First period; b, second period. In each panel, the top two traces are delay times estimated from time windows that contain respectively the S-wave arrival and the S-wave arrival plus the coda; the third trace is barometric pressure; the fourth trace is temperature; and the bottom trace is precipitation. In a, the second to last trace is a temperature corrected version of the second trace. Elapsed time is calculated from 2 November 2005, 00:00:00 UT.

Silver et al. [2007] found that this temperature sensitivity originates from the electronics of the recording system rather than from changes in the subsurface velocity field. We excluded the measurements of the first few days to allow the source and sensor to be stabilized at their locations. We also removed the linear trend from the data as was done by *Silver et al.* [2003]. In general, the delay times of the coda are about twice as large as those of the S wave, suggesting that they are caused by a change in the velocity of the bulk media, as the coda travels for a longer time in the media and thus is expected to accumulate a larger travel-time anomaly. The delay time closely follows the barometric pressure changes for the first period (Figure B.3a).

After removing the temperature effect from the measured delay time variations (Figure B.3a), we obtained a delay time change of ~ 3.0 μs in the first period. The corresponding velocity perturbation is about 3×10^{-4}, about an order of magnitude higher than the detectable threshold. During the same time period, the change in barometric pressure is ~ 1.3 kPa. We used a linear regression to estimate the stress sensitivity of the velocity and obtained a value of 2.4×10^{-7} Pa^{-1}. We also calculated the predicted solid Earth tides at the site in the same period and found that the tidal stress varies within 240 Pa, nearly an order of magnitude smaller than changes in barometric pressure. Thus the travel-time changes induced by tidal stress are of the order of 10^{-7} s, close to the measurement error and thus are predicted to be undetectable.

The negative correlation between travel time and barometric stress can be further seen in the delay time data through to the end of the ninth day of the second period. After this time the relationship starts to break down, and we observe instead two prominent excursions in the delay time data that are not seen in the barometric pressure record.

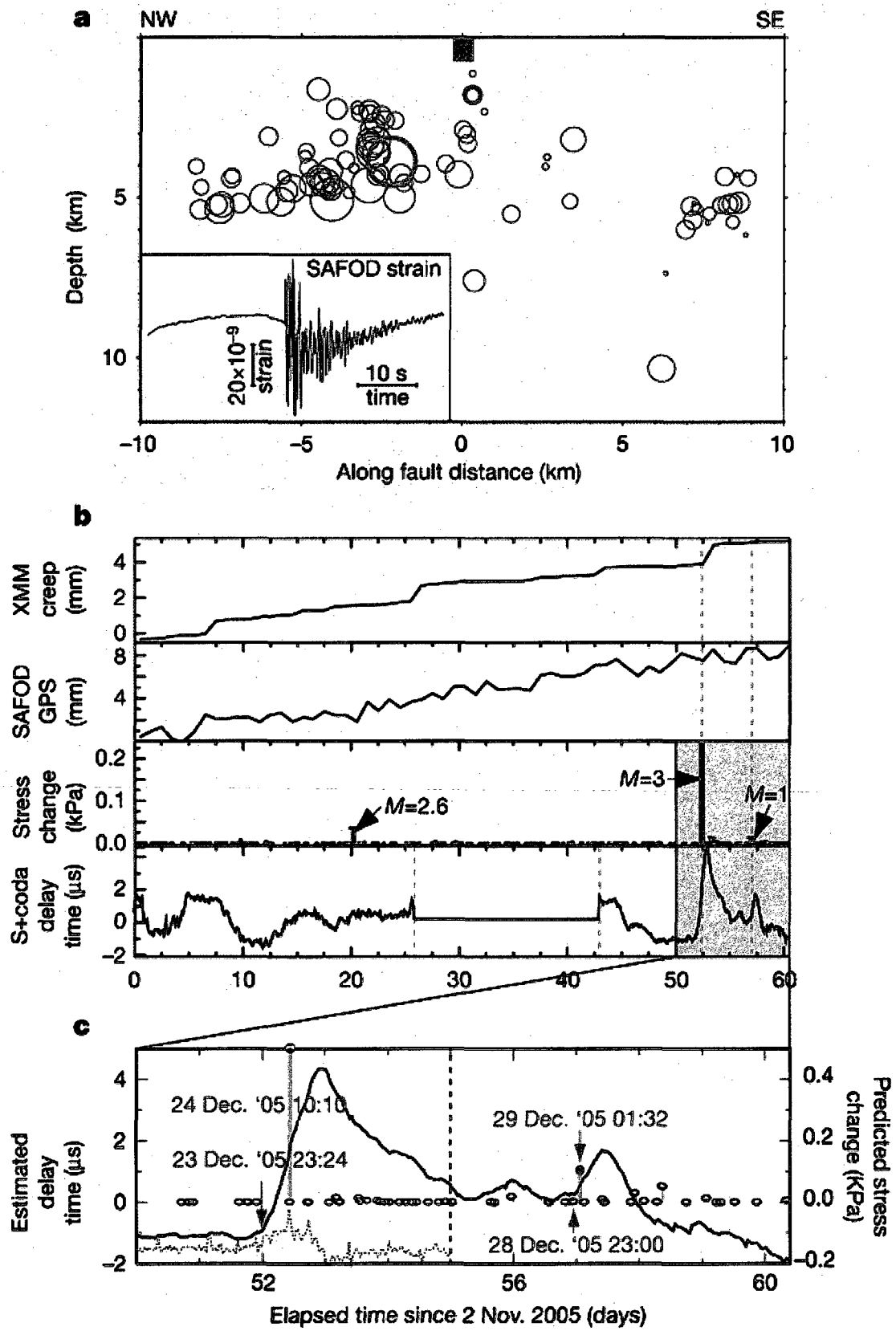
a
NW
SE
Depth (km)
5
10
SAFOD strain
20×10⁻⁹ strain
10 s time
−10
−5
0
5
10
Along fault distance (km)
b
XMM creep (mm)
SAFOD GPS (mm)
Stress change (kPa)
M=2.6
M=3
M=1
S+coda delay time (μs)
0
10
20
30
40
50
60
c
Estimated delay time (μs)
24 Dec. '05 0:10
23 Dec. '05 23:24
29 Dec. '05 01:32
28 Dec. '05 23:00
Predicted stress change (KPa)
52
56
60
Elapsed time since 2 Nov. 2005 (days)

Figure B.4 A comparison of delay time variations with local seismicity and other deformation measurements. a, Depth distribution of earthquakes that occurred in the experimental period. Red square, the SAFOD experiment site; red and green circles, the $M = 3$ and $M = 1$ earthquake, respectively. Inset, the SAFOD strainmeter record, which shows a step function coseismic strain change. The low frequency content of the strainmeter data is severely contaminated by surface temperature variations, and is consequently not suitable for analysis. b, Top to bottom: creep measurement at Middle Mountain (XMM); GPS measurement of fault parallel motion at the SAFOD site; calculated static coseismic stress changes at the SAFOD experiment site for all of the earthquakes; and delay times estimated from the S wave plus its coda for comparison. Dashed lines indicate the time when the M = 3 and M = 1 earthquakes occurred. Note that the amplitude of the stress change of the M = 3 event (~0.5 kPa) is saturated in this plot. c, Predicted coseismic stress changes at SAFOD for earthquakes occurring between 22 December 2005 (day 50) and 1 January 2006 (day 60) indicated by shading in b are shown with the delay time estimation. Stress changes from the local seismicity between days 55 and 60 are amplified by a factor of 10. The two filled circles show the stress change of the $M = 3$ (red) and $M = 1$ (green) event, respectively. The vertical lines indicate the occurrence times of the $M = 3$ and the $M = 1$ event, and the red and green (upward) arrows show the onset times of the two excursions. Blue dotted line is the derivative of the delay time series. Notice that the largest change occurred about ~30 s after the $M = 3$ earthquake.

It is also confirmed that the two excursions were not caused by precipitation or instrumentation. The amplitudes of the two excursions are ~5.5 μs and ~1.5 μs, respectively, over the nominal ~10 ms coda travel time. Using our measured stress sensitivity of 2.4×10^{-7} Pa^{-1}, the corresponding stress changes are 2.3 kPa and 625 Pa for the first and second peak, respectively.

In order to evaluate the possibility of a tectonic cause for the excursions, we examined the seismicity around the SAFOD site occurring in the experiment period (Figure B.4a). The first peak appears to correspond to the largest earthquake occurring in this period (date, 24 December 2005; time, 10:10:57.21 (h:min:s UT); location, 35.9970° N, 120.5565° W; depth, 3.88 km; magnitude 3.00, hereafter the $M = 3$ event), while the second peak corresponds to the second closest (1.5 km) event to the experiment site (29 December 2005, 01:32:50.87 UT, 35.9788° N, 120.5397° W, depth 1.82 km, magnitude 0.98, hereafter the $M = 1$ event). The closest event is about 1.3 km away from our site, but its size is only $M = 0.34$ and thus should not have a large effect at the site.

We calculated the predicted static stress change at SAFOD associated with these two earthquakes. The near-field static displacement at a location **r** with respect to the earthquake is proportional to $M_o r^{-2}$, where M_o is the seismic moment [*Aki and Richards*, 1980]. The spatial derivative of displacement, strain, thus should be ~ $M_o r^{-3}$. The static stress change at **r** is $\Delta\sigma = a\frac{\mu L^2 D}{r^3} = a\frac{\mu(D/L)}{(r/L)^3} = a\frac{\Delta\sigma_o}{\hat{r}^3}$, where $\Delta\sigma_o$ is the average static stress change along the fault, $\hat{r}$ is the characteristic distance measured in fault lengths (L), D is slip on the fault, μ is the shear modulus, and a is a scaling constant equal to $1/(6\pi)$ [*Aki and Richards*, 1980]. If we assume a static stress change in the range of 3 to 10 MPa [*Abercrombie*, 1995; *Rubin and Gillard*, 2000], then the static coseismic stress change at

the SAFOD site is estimated to be ~250–833 Pa for the $M = 3$ event, which is a few times lower than the total stress change (2.3 kPa) calculated from the amount of delay time during the first excursion. The predicted static stress changes at the SAFOD site calculated from the entire local seismicity catalogue are shown in Figure B.4b. Here we used all the events that occurred within 10 km of the site and made a time series of the coseismic stress changes. The $M = 3$ earthquake obviously has the largest effect at the experiment site. The second largest peak around day 20 corresponds to a relatively deep event (22 November 2005, 03:38:02.13 UT, 36.0100 2120.5692, depth 5.07 km, M52.6), which is not observed in the delay time data. The third peak corresponds to the $M = 1$ event. It is not clear to us why the larger $M = 2.6$ event is not observed while the smaller $M = 1$ event shows clearly in the delay time data. But we noticed that data collected in the second period had a better SNR than those of the first period. The associated stress change of the $M = 2.6$ event thus might be below the resolution of the first-month data.

Coseismic change was also observed in other geodetic data. We found a step-function change from the borehole fibre-optic strainmeter data at SAFOD (Figure B.4a inset) as well as from the surface creepmeter data at Middle Mountain (Figure B.4b). The static strain change observed at SAFOD is ~$(20–25) \times 10^{-9}$, corresponding to a coseismic stress change of ~600–750 Pa, which is of the same order of magnitude as our estimate. On the other hand, there were no obvious changes in the SAFOD GPS, or the FLT and DLT strainmeter records (Figure B.4b). The lack of an observable coseismic signal at these sites is, however, predicted by the theoretical amplitude.

The coseismic offset recorded by the SAFOD strainmeter is not obviously present in the delay time data measured either from the manually stacked 45-min-per-sample data or

from the delay times calculated from the 27-s-per-sample raw data. The derivative of the delay time series (dotted line in Figure B.4c), however, does reveal that the largest offset of the entire two-month observing period occurred ~30 s after the $M = 3$ earthquake. This suggests that there was a small coseismic change in the delay time data. The lack of a stronger coseismic signal in the delay time data may imply that the velocity changes we observed here are mainly the result of a poroelastic [*Segall et al.*, 2003] rather than an elastic response to abrupt stress changes.

The two travel-time excursions appear to possess significant preseismic components. The first excursion was observed to start at 23:34 UT on 23 December 2005, while the $M = 3$ earthquake occurred at ~10.6 h later, at 10:10 UT on 24 December 2005 (Figure B.4c). The excursion reached a maximum right after the earthquake, peaking at 21:21 UT on 24 December 2005. The excursion thus has a clear preseismic component besides the coseismic/postseismic changes. The preseismic and coseismic/postseismic components account for ~46% and ~54% of the total change, respectively. This is also true for the second excursion. Its onset is around 22:59 UT on 28 December 2005, about 2.5 h before the occurrence of the $M = 1$ earthquake (01:32 UT on 29 December, Figure B.4c).

With the available geodetic instrumentation, it was impossible to further evaluate the preseismic component. The most direct test would have been with the SAFOD borehole strainmeter data. Unfortunately, the low frequency component is severely contaminated by surface temperature variations and is unusable for periods longer than a few minutes, and is thus not useful in confirming the two low-frequency excursions [*M. Zumberge*, personal communication]. All other instrumentation is either too far away or not sufficiently sensitive to observe even the coseismic offset. Historically, there has been an

absence of preseismic signals in geodetic observations, such as a borehole strainmeter. We suggest that this may be the result of two differences between such instruments and our 'stress meter'. First, our basic measurement is not strain, but rather a stress-induced change in the effective elastic constants of a poroelastic medium, mediated by variations in crack properties and fluid flow. These changes may register only weakly on a strainmeter, a GPS, or a creepmeter. Second, a conventional strainmeter measures local change in the volume immediately surrounding the instrument while our measurements reflect stress/strain changes occurring over a volume sampled by the coda waves that could be orders of magnitude larger.

We put forward the hypothesis that there is a change in effective elastic moduli before rupture, such as a sudden increase in microcrack density, which is a phenomenon related to dilatancy and observed in many laboratory studies [*Brace et al.*, 1966; *Scholz*, 1968]. As such, further continuous seismic monitoring might provide an effective tool for understanding the stress changes that accompany and perhaps precede seismic activity.

Acknowledgements. We thank the NSF funded SAFOD programme and those involved in providing the experiment site, R. Trautz for supplying the barometric pressure logger, M. Zumberge for providing the SAFOD strainmeter data, and D. Lippert and R. Haught for helping with field work. This work was supported by the NSF, Rice University, the Carnegie Institution of Washington, and Lawrence Berkeley National Laboratory of the US Department of Energy under contract DE-AC02-05CH11231.

B.3 Supplementary Materials

Methods

Data acquisition system. Our acquisition was conducted with a combination of commercial and specially built equipment. The latter are the piezoelectric source and the high voltage amplifier used to power it. The source includes 18 cylindrical rings of piezoelectric ceramic (lead zirconate titanate) epoxied together and wired for positive and negative voltage on the inner and outer surfaces. The source was fluid coupled to the well casing. A three-component accelerometer was clamped to the well casing to provide coupling and reduce relative motions between the source and receiver. We used a commercial recording system, a 'Geode' manufactured by Geometrics, which has a 24 bit analogue-to-digital converter. An air conditioner and heater were used to maintain the recording system electronics within a temperature range of about ±1°C.

Triggering was used in our data recording system. The digitizer continually samples the data, and receives a trigger that will generally be between two digitized samples. Including a section of pre-trigger data, the time series is interpolated and re-sampled, so that the new time series begins at the time of the trigger. This start time is not exact, and, at a sampling rate of 48,000 s^{-1}, this time is computed to the nearest twentieth of a sample [Geometrics engineering, personal communication]. Thus there is a delay time measurement error that will be at most a fortieth of a sample (half-way between samples), and the average error will be an eightieth of a sample, assuming that the errors are uniformly distributed. This corresponds to an average error of 260 ns per trigger. The error in the stacked data decreases by a factor of $N^{1/2}$, assuming the errors are uncorrelated. For $N = 100$, we obtain a timing error of 26 ns.

Optimum experimental design. As shown by *Silver et al.* [2007], there is an optimum distance between the source and receiver that minimizes the detectable threshold of subtle velocity changes:

$$N = Q/\pi \tag{1}$$

Here N is the number of wavelengths between the source and receiver and Q is the quality factor. At the SAFOD site, Q is around 200, which gives $N = 64$. If we assume the S-wave velocity to be 2.8 m ms^{-1}, then the wavelength of the signal with a dominant frequency of 2 kHz is about 1.4 m, so the optimum distance is ~90 m. As it was necessary to perform the experiment in the available boreholes, our cross-hole distance was limited to 10 m, which while not optimal still provided us with a good SNR.

Subsample delay time estimate (DTE). In this study, we employed a cosine fitting method to estimate subsample delay time in the time domain [*Cespedes et al.*, 1995; De *Jong et al.*, 1990]. Given the largest sample of the correlation function, cc(0), and its two neighbours cc(-1) and cc(1), the estimated subsample shift is given by following expression:

$$\tau = \alpha / \arctan\left(\frac{cc(-1)-cc(1)}{2cc(0)\sin\alpha}\right), \tag{2}$$

where,

$$\alpha = \arccos\left(\frac{cc(-1)+cc(1)}{2cc(0)}\right). \tag{3}$$

Error estimation. *Silver et al.* [2007] derived a low bound of the error in delay time measurements:

$$\sigma_{DTE} \geq \frac{1}{2\pi f_0 \cdot SNR} . \quad (4)$$

Here f_0 is the dominant frequency of the source pulse, and SNR is the signal-to-noise ratio. Equation (4) indicates that SNR is the only parameter that controls the precision in our delay time estimation when the digitizing error is much less than the background noise in this regime. The precision is not controlled by the sampling rate of the digitizer so it is possible to obtain subsample-interval measurements of the delay time. The dominant frequency of our data is 2 kHz and the SNR is around 700 for the 45-min stacked data, resulting in a best achievable precision of $\sim 1.1 \times 10^{-7}$ s, or 110 ns in the DTE.

We also measured delay time between each two consecutive samples, which follows a Gaussian distribution with a standard deviation of ~80 ns and ~50 ns for the first and second recording period, respectively. In general they are comparable to or even better than the theoretical low bound in equation (4). Since there is contribution from the actual stress-induced velocity perturbations in the measurement, our actual precision can be better than the measured standard deviations. Thus the lower bound appears to be larger than the true DTE error. One possible explanation is that the SNR is significantly underestimated, as the noise is estimated from a time window before the first arrival, which actually contains a considerable amount of non-random electronic noise known as crosstalk, and non-random 'wrap-around' noise from the previous shot.

The precision discussed here does not include other systematic non-random noise, such as changes in the source pulses, errors in trigger timing and digitizer's clock. Such systematic errors could lead to a long-term trend in DTE. To estimate these effects, we

also recorded the source pulse waveform in addition to the data. We employed the same method to measure the variation in the source pulse width. Changes in the source pulse width are between ±20 ns. This indicates that our source pulse generator and recording system were very stable in the two periods and timing error in the digitizer clock was also very small.

REFERENCES:

Abercrombie, R. E. (1995), Earthquake source scaling relationships from -1 to 5 M_L using seismograms recorded at 2.5-km depth, *J. Geophys. Res.*, *100*, 24,015-24,036.

Abercrombie, R. E. (1996), The magnitude-frequency distribution of earthquake recorded with deep seismometers at Cajon Pass, Southern California, *Tectonophysics*, *261*, 1-7.

Aki, K. (1985), Theory of earthquake prediction with special reference to monitoring of the quality factor of lithosphere by the coda method, *Earthq. Pred. Res.*, *3*, 219–230.

Aki, K. (1995), Interrelation between fault zone structures and earthquake processes, *Pure Appl. Geophys.*, *145*, 647–676.

Aki, K., and P. Richards (1980), *Quantitative Seismology*, W.H. Freeman, New York.

Baisch, S., and G. H. R. Bokelmann (2001), Seismic waveform attributes before and after the Loma Prieta earthquake: Scattering change near the earthquake and temporal recovery, *J. Geophys. Res.*, 106(B8), 16,323–16,337.

Bates, D. M. and D. G. Watts (1988), *Nonlinear Regression and Its Applications*, Wiley, New York.

Bensen, G. D., M. H. Ritzwoller, M. P. Barmin, A. L. Levshin, F. Lin, M. P. Moschetti, N. M. Shapiro, and Y. Yang (2007), Processing seismic ambient noise data to obtain reliable broad-band surface wave dispersion measurements, *Geophys. J. Int.*, *169*, 1239-1260.

Birch, F. (1960), The velocity of compressional waves in rocks to 10 kilobars, part 1, *J. Geophys. Res.*, *65*, 1083–1102.

Birch, F. (1961), The velocity of compressional waves in rocks to 10 kilobars, part 2, *J. Geophys. Res.*, *66*, 2199–2224.

Boatwright, J. (1978), Detailed spectral analysis of two small New York State earthquakes, *Bull. Seis. Soc. Am.*, *68*, 1177–1131.

Brace, W. F., B. W. Paulding, and C. H. Scholz (1966), Dilatancy in the fracture of crystalline rocks, *J. Geophys. Res.*, *71*, 3939–3953.

Brenguier, F., M. Campillo, C. Hadziioannou, N. M. Shapiro, R. M. Nadeau, and E. Larose (2008b), Postseismic relaxation along the San Andreas Fault at Parkfield from continuous seismological observations, *Science*, *321*, 1478-1481.

Brenguier, F., N. M. Shapiro, M. Campillo, V. Ferrazzini, Z. Duputel, O. Coutant, and A. Nercessian (2008a), Towards forecasting volcanic eruptions using seismic noise, *Nat. Geosci.*, *1*, 126-130, doi:10.1038/ngeo104.

Brune, J. N. (1970), Tectonic stress and the spectra of seismic shear waves from earthquakes, *J. Geophys. Res.*, *75*, 4997–5009.

Campillo, M., and A. Paul (2003), Long-range correlations in the diffuse seismic coda, *Science*, *299*, 547-549.

Carter, G.C. (1987). Coherence and time delay estimation, *Proc. IEEE,75*, 236-255.

Cespedes, I., Y. Huang, J. Ophir, and S. Spratt (1995), Methods for estimation of sub-sample time delays of digitized echo signals, *Ultrason. Imaging, 17*, 142-171.

Cheng, X., F. Niu , P. G. Silver, and R. Nadeau (2008), Seismic imaging of scatterer migration associated with the 2004 Parkfield earthquake using waveform data of repeating earthquakes and active sources, *Bull. Seismol. Soc. Am.*, to be submitted.

Cheng, X., F. Niu, and B. Wang (2008), Coseismic velocity change during the 2008 Wenchuan earthquake observed from seismic ambient noise, *Geophys. Res. Lett.*, to be submitted.

Cheng, X., F. Niu, P. G. Silver, S. Horiuchi, K. Takai, Y. Iio, and H. Ito (2007), Similar microearthquakes observed in western Nagano, Japan, and implications for rupture mechanics, J. Geophys. Res., 112, B04306, doi:10.1029/2006JB004416.

Chouet, B. (1979), Temporal variation in the attenuation of earthquake coda near Stone Canyon, California, *Geophys. Res. Lett., 6*, 143–146.

Crampin, S., and S.V. Zatsepin (1997), Modelling the compliance of crustal rock; II, Response to temporal changes before earthquakes, *Geophys. J. Int., 129*, 495–506.

De Fazio, T. L., K. Aki, and J. Alba (1973), Solid earth tide and observed change in the in situ seismic velocity, *J. Geophys. Res.*, *78*, 1319–1322.

De Jong, P.G.M., T. Arts, A.P.G. Hoeks, and R.S. Reneman (1990), Determination of tissue motion velocity by correlation interpolation of pulsed ultrasonic echo signals, *Ultrason. Imaging, 12,* 84-98.

Dodge, D. A., and G. C. Beroza (1997), Source array analysis of coda waves near the 1989 Loma Prieta, California, mainshock: Implications for the mechanism of coseismic velocity changes, *J. Geophys. Res.*, *102*, 24437-24458.

Ellsworth, W. L. (1994), Characteristic earthquakes and long-term earthquake forecasts: Implications of central California seismicity, in *Urban Disaster Mitigation*, edited by F.Y. Cheng and M.-S. Sheu, pp. 1-14, Elsevier Sci., New York.

Frankel, A., and R. W. Clayton (1986), Finite-difference simulations of seismic scattering: Implications for propagation of short-period seismic waves in the crust and models of crustal heterogeneity, *J. Geophys. Res.*, *91*, 6465-6489.

Freed, A.M., and J. Lin (2001), Delayed triggering of the 1999 Hector Mine earthquake by viscoelastic stress transfer, *Nature*, *411*, 180–183.

Got, J.-L., J. Fréchet, and F. Klein (1994), Deep fault plane geometry inferred from multiplet relative relocation beneath the south flank of Kilauea, *J. Geophys. Res.*, *99*, 15,375-15,386.

Gutenberg, B., and C. F. Richter (1944), Frequency of earthquakes in California, *Bull. Seismol. Soc. Am.*, *34*, 185–188.

Hanks, T. C., and H. Kanamori (1979), A moment magnitude scale, *J. Geophys. Res.*, *84*, 2348–2350.

Horiuchi, S., K. Ito, T. Matsuzawa, and A. Hasegawa (1992), A real-time processing system of seismic wave using personal computers, *J. Phys. Earth.* 40, 395-406.

Igarashi, T., T. Matsuzawa, and A. Hasegawa (2003), Repeating earthquakes and interplate aseismic slip in the northeastern Japan subduction zone, *J. Geophys. Res.*, *108*(B5), 2249, doi:10.1029/2002JB001920.

Iio, Y., S. Ohmi, R. Ikeda, E. Yamamoto, H. Ito, Y. Kuwahara, T. Ohminato, B. Shibazaki, and M. Ando (1999), Slow initial phase generated by microearthquakes occurring in the western Nagano prefecture, Japan: the source effect, *Geophys. Res. Lett.*, *26*, 1969-1972.

Imanishi, K., M. Takeo, W. L. Ellsworth, H. Ito, T. Matsuzawa, Y. Kuwahara, Y. Iio, S. Horiuchi, and S. Ohmi (2004), Source parameters and rupture velocities of microearthquakes in Western Nagano, Japan, determined using stopping phases, *Bull. Seism. Soc. Am.*, *94*, 1762-1780.

Johanson, I. A., E. J. Fielding, and F. Rolandone (2006), Coseismic and Postseismic slip of the 2004 Parkfield earthquake from space-geodetic data, *Bull. Seismol. Soc. Am.*, *96*, S56–S72.

Kanamori, H., and D. L. Anderson (1975), Theoretical basis for some empirical relations in seismology, *Bull. Seismol. Soc. Am.*, *65*, 1073–1095.

Kimata, F., R. Miyajima, M. Murase, D. Darwaman, T. Ito, Y. Ohata, M. Irwan, K.Takano, F. Ibrahim, E. Koyama, H. Tsuji, T. Takayama, K. Uchida, J. Okada, D. Solim and H. Anderson (2004), Ground Uplift Detected by Precise Leveling in the Ontake Earthquake Swarm Area, Central Japan in 2002-2004, *Earth Planets and Space*, *12*, 45-48.

Leary, P. C., P. E. Malin, R. A. Phinny, T. Brocher, and R. Voncolln (1979), Systematic monitoring of millisecond traveltime variations near Palmdale, California, *J. Geophys. Res.*, *84*, 659–666.

Li, L., Q.-F. Chen, X. Cheng, and F. Niu (2007), Spatial clustering and repeating of seismic events observed along the 1976 Tangshan fault, north China, *Geophys. Res. Lett.*, *34*, L23309, doi:10.1029/2007GL031594.

Li, Y.-G., J. E. Vidale, K. Aki, F. Xu, and T. Burdette (1998), Evidence of shallow fault zone healing after the 1992 *M* 7.5 Landers, California, earthquake, *Science*, *279*, 217–219.

Li, Y.-G., J. E. Vidale, S. M. Day, D. D. Oglesby, and E. Cochran (2003), Postseismic fault healing on the rupture zone of the 1999 *M* 7.1 Hector Mine, California, earthquake, *Bull. Seismol. Soc. Am.*, *93*, 854– 869.

Li, Y.-G., P. Chen, E. S. Cochran, J. E. Vidale, and T. Burdette (2006), Seismic evidence for rock damage and healing on the San Andreas Fault associated with the 2004 M6 Parkfield earthquake, *Bull. Seismol. Soc. Am.*, *96*, 349– 363.

Michelini, A., and T. V. McEvilly (1991), Seismological studies at Parkfield. I. Simultaneous inversion for velocity structure and hypocenters using cubic B-splines parameterization, *Bull. Seismol. Soc. Am.*, *81*, 524–552.

Mosteller, F., and J. W. Tukey (1977), *Data Analysis and Linear Regression,* Addison-Wesley, Reading, Massachusetts.

Nabelek, J., W. P. Chen, and H. Ye (1987), The Tangshan earthquake sequence and its implications for the evolution of the North China Basin, *J. Geophys. Res.*, *92*, 12,615–12,628.

Nadeau, R. M., and L. R. Johnson (1998), Seismological studies at Parkfield VI: Moment release rates and estimates of source parameters for small repeating earthquakes, *Bull. Seismol. Soc. Am.*, *88*, 790–814.

Nadeau, R. M., and T. V. McEvilly (1999), Fault slip rates at depth from recurrence intervals of repeating microearthquakes, *Science*, *285*, 718-721.

Nadeau, R. M., W. Foxall, and T. V. McEvilly (1995), Clustering and periodic recurrence of microearthquakes on the San Andreas Fault at Parkfield, California, *Science, 267*, 503–507.

Nishimura, N., and Y. Yagi (2008), http://www.geol.tsukuba.ac.jp/~nisimura/20080512/.

Nishimura, T., N. Uchida, H. Sato, M. Ohtake, S. Tanaka, and H. Hamaguchi (2000), Temporal Changes of the Crustal Structure Associated with the M6.1 Earthquake on September 3, 1998, and the Volcanic Activity of Mount Iwate, Japan, *Geophys. Res. Lett.*, 27(2), 269–272.

Niu, F., P. G. Silver, R. M. Nadeau and T. V. McEvilly (2003), Stress-Induced Migration of Seismic Scatterers Associated with the 1993 Parkfield aseismic transient event, *Nature, 426*, 544-548.

Niu, F., P. G. Silver, T. M. Daley, X. Cheng, and E. L. Majer (2008), Preseismic velocity changes observed from active source monitoring at the Parkfield SAFOD drill site, *Nature, 454*, 204-208, doi:10.1038/nature07111.

Nur, A. (1971), Effects of stress on velocity anisotropy in rocks with cracks, *J. Geophys. Res., 76*, 2022–2034.

Nur, A., and G. Simmons (1969), The effect of saturation on velocity in low porosity rocks, *Earth Planet. Sci. Lett., 7,* 183-193.

O'Connell, R. J., and B. Budiansky (1974). Seismic velocities in dry and saturated cracked solids, *J. Geophys. Res., 79*, 5412–5426.

Peng, Z., and Y. Ben-Zion (2006), Temporal changes of shallow seismic velocity around the Karadere-Duzce branch of the north Anatolian fault and strong ground motion, *Pure Appl. Geophys., 163*, 567-599, doi: 10.1007/s00024-005-0034-6.

Peng, Z.-G., J. E. Vidale, C. Marone and A. M. Rubin (2005), Systematic variations in recurrence interval and moment of repeating aftershocks, *Geophys. Res. Lett., 32*(L15301), doi:10.1029/2005GL022626.

Reasenberg, P., and K. Aki (1974), A precise, continuous measurement of seismic velocity for monitoring in situ stress, *J. Geophys. Res., 79*, 399–406.

Rubin, A. M., and D. Gillard (2000), Aftershock asymmetry/rupture directivity among central San Andreas Fault microearthquakes, *J. Geophys. Res., 105*, 19,095-19,109.

Rubin, A. M., D. Gillard, and J.-L. Got (1999), Streaks of microearthquakes along creeping faults, *Nature, 400*, 635–641.

Rubinstein, J. L., and G. C. Beroza (2004a), Evidence for widespread nonlinear strong ground motion in the Mw 6.9 Loma Prieta earthquake, *Bull. Seismol. Soc. Am., 94,* 1595–1608.

Rubinstein, J. L., and G. C. Beroza (2004b), Nonlinear strong ground motion in the ML 5. 4 Chittenden earthquake: Evidence that preexisting damage increases susceptibility to further damage, *Geophys. Res. Lett., 31,* L23614, doi:10.1029/2004GL021357.

Rubinstein, J. L., and G. C. Beroza (2005), Depth constraints on nonlinear strong ground motion from the 2004 Parkfield earthquake, *Geophys. Res. Lett., 32,* L14313, doi: 10.1029/2005GL023189.

Rubinstein, J. L., N. Uchida, and G. C. Beroza (2007), Seismic velocity reductions caused by the 2003 Tokachi-Oki earthquake, *J. Geophys. Res., 112,* B05315, doi:10.1029/2006JB004440.

Sato, H., and M. C. Fehler (1998), *Seismic Wave Propagation and Scattering in the Heterogeneous Earth,* Springer, New York.

Schaff, D. P., and G. C. Beroza (2004), Coseismic and postseismic velocity changes measured by repeating earthquakes, *J. Geophys. Res., 109,* B10302, doi:10.1029/2004JB003011.

Schaff, D. P., and P. G. Richards (2004), Repeating seismic events in China, *Science, 303,* 1176–1178.

Scholz, C. H. (1968), Microfracturing and the inelastic deformation of rock in compression, *J. Geophys. Res., 73,* 1,417-1,432.

Schorlemmer, D., and S. Wiemer (2005), Microseismicity data forecast rupture area, *Nature, 434,* 1086, doi:10.1038/4341086a.

Segall, P. and J. R. Rice (1995), Dilatancy, compaction and slip instability of a fluid-infiltrated fault, *J. Geophys. Res., 100,* 22,155-22,171.

Segall, P., S. Jonsson, and K. Agustsson (2003), When is the strain in the meter the same as the strain in the rock? *Geophys. Res. Lett., 30,* doi:10.1029/2003GL017995.

Sens-Schönfelder, C., and U. Wegler (2006), Passive image interferometry and seasonal variations of seismic velocities at Merapi volcano, Indonesia, *Geophys. Res. Lett., 33,* L21302.

Shapiro, N. M., and M. Campillo (2004), Emergence of broadband Rayleigh waves from correlations of the ambient seismic noise, *Geophys. Res. Lett., 31,* L07614, doi:10.1029/2004GL019491.

Shapiro, N. M., M. Campillo, L. Stehly, and M. H. Ritzwoller (2005), High resolution surface wave tomography from ambient seismic noise, *Science*, *307*, 1615–1618.

Shapiro, N. M., M. H. Ritzwoller, and G. D. Bensen (2006), Source location of the 26 sec microseism from cross correlations of ambient seismic noise, *Geophys. Res. Lett.*, *33*, L18310, doi:10.1029/2006GL027010.

Shearer, P. M., E. Hauksson and G. Lin (2005), Southern California hypocenter relocation with waveform cross-correlation, part 2: results using source-specific station terms and cluster analysis, *Bull. Seis. Soc. Am.*, *95*, 904-915.

Shedlock, K. M., J. Baranowski, W. Xiao, and X. L. Hu (1987), The Tangshan aftershock sequence, *J. Geophys. Res.*, *92*, 2791–2803.

Silver, P. G., T. M. Daley, F. Niu, and E. L. Majer (2007), Active source monitoring of crosswell seismic traveltime for stress-induced changes, *Bull. Seismol. Soc. Am.*, *97*, 281–293.

Snieder, R., A. Grêt, H. Douma, and J. Scales (2002), Coda wave interferometry for estimating nonlinear behavior in seismic velocity, *Science*, *295*, 2253–2255, doi:10.1126/science.1070015.

Snieder, R., and M. Vrijlandt (2005), Constraining relative source locations with coda wave interferometry: Theory and application to earthquake doublets in the Hayward Fault, California, *J. Geophys. Res.*, *110*, B04301, 10.1029/2004JB003317.

Stehly, L., M. Campillo, and N. M. Shapiro (2007), Travel time measurements from noise correlation: Stability and detection of instrumental errors, *Geophys. J. Int.*, *171*, 223-230.

Stein, R.S. (1999), The role of stress transfer in earthquake occurrence, *Nature*, *402*, 605-609.

Stork, A. L., and H. Ito (2004), Source parameter scaling for small earthquakes observed at the western Nagano deep borehole, Central Japan, *Bull. Seis. Soc. Am.*, *94*, 1781-1794.

Unsworth, M., P. Bedrosian, M. Eisel, G. Egbert, and W. Siripunvaraporn (2000), Along strike variations in the electrical structure of the San Andreas Fault at Parkfield, California, *Geophys. Res. Lett.*, *27*, 3021–3024.

Vidale, J. E., and Y. G. Li (2003), Damage to the shallow Landers fault from the nearby Hector Mine earthquake, *Nature*, *421*, 524–526.

Vidale, J. E., W. L. Ellsworth, A. Cole, and C. Marone (1994), Variations in rupture process with recurrence interval in a repeated small earthquake, *Nature*, *36*, 8624–8626.

Waldhauser, F. (2001), hypoDD: a program to compute double-difference hypocenter locations (hypoDD version 1.0-3/2001), *U.S. Geol. Surv. Open File Rept. 01-113.*

Waldhauser, F., and W. L. Ellsworth (2000), A double-difference earthquake location algorithm: Method and application to the northern Hayward fault, California, *Bull. Seismol. Soc. Am.*, *90*, 1353–1368.

Waldhauser, F., and W.L. Ellsworth (2002), Fault structure and mechanics of the Hayward fault, California, from double-difference earthquake locations, *J. Geophys. Res.*, *107*(B3), 2054, doi:10.1029/2000JB000084.

Walker W.F., and G.E. Trahey (1995), A fundamental limit on delay estimation using partially correlated speckle signals, *IEEE Trans. On Ultras., Fer. And Freq. Control, 42*, 301-308.

Walsh, J. B. (1965), The effect of cracks on the compressibility of rock, *J. Geophys. Res., 70*, 381-389.

Wang, Q., et al. (2001), Present-day crustal deformation in China constrained by Global Positioning System (GPS) measurements, *Science*, *294*, 574–577.

Weaver, R. L., and O. I. Lobkis (2001), Ultrasonics without a source: thermal fluctuation correlations at MHz frequencies, *Phys. Rev. Lett.*, 87, 134301-134304.

Yamamura, K., O. Sano, H. Utada, Y. Takei, S. Nakao, and Y. Fukao (2003), Long-term observation of in situ seismic velocity and attenuation, *J. Geophys. Res.*, *108,* 10.1029/2002JB002005.

Yang, Y., M. H. Ritzwoller, A. L. Levshin, and N. M. Shapiro (2007), Ambient noise Rayleigh wave tomography across Europe, *Geophys. J. Int.*, *168*, 259–274.

Yao, H., R. D. van der Hilst, and M. V. De Hoop (2006), Surface-wave array tomography in SE Tibet from ambient seismic noise and twostation analysis: I–Phase velocity maps, *Geophys. J. Int.*, *166*, 732–744.

Yoshida, S., and K. Koketsu (1990), Simultaneous inversion of waveform and geodetic data for the rupture process of the 1984 Naganoken-Seibu, Japan, earthquake, *Geophys. J. Int.*, *103*, 335-362.

Yukutake, Y., Y. Iio, K. Takai and S. Horiuchi (2006), The detailed spatial change in the stress field in the 1984 Western Nagano Prefecture Earthquake Region, *J. Geophys. Res.*, submitted.